CHARACTERIZATION AND MODELING OF TRANSFORMATION INDUCED FATIGUE OF SHAPE MEMORY ALLOY ACTUATORS

A Dissertation

by

OLIVIER WALTER BERTACCHINI

Submitted to the Office of Graduate Studies of
Texas A&M University
in partial fulfillment of the requirements for the degree of

DOCTOR OF PHILOSOPHY

December 2009

Major Subject: Aerospace Engineering

CHARACTERIZATION AND MODELING OF TRANSFORMATION INDUCED FATIGUE OF SHAPE MEMORY ALLOY ACTUATORS

A Dissertation

by

OLIVIER WALTER BERTACCHINI

Submitted to the Office of Graduate Studies of
Texas A&M University
in partial fulfillment of the requirements for the degree of

DOCTOR OF PHILOSOPHY

Approved by:

Chair of Committee,	Dimitris C. Lagoudas
Committee Members,	James G. Boyd
	Vikram K. Kinra
	Ibrahim Karaman
	Gary T. Fry
	Etienne Patoor
Head of Department,	Dimitris C. Lagoudas

December 2009

Major Subject: Aerospace Engineering

ABSTRACT

Characterization and Modeling of Transformation Induced Fatigue of Shape Memory Alloy Actuators.

(December 2009)

Olivier Walter Bertacchini, Eng. Diploma, M.S., ENSAM Paris-Tech (Metz), France

Chair of Advisory Committee: Dr. Dimitris C. Lagoudas

The main focus of this research is the transformation induced fatigue behavior of shape memory alloy (SMA) actuators undergoing thermally induced martensitic phase transformation. The recent development of aerospace applications employing shape memory alloys (SMAs) has expanded the need for fatigue life characterization and modeling. Lightweight, compact and with a great work output, SMAs are ideal materials for actuated structural components. However, fatigue life becomes a key factor in applications such as commercial airplanes. Therefore, it is necessary to not only perform fatigue testing but also to investigate the causes of fatigue failure. As a new class of materials, SMAs have unique characteristics and require novel test methodologies to conduct repeatable and reliable fatigue testing. For this research, two materials are being investigated: TiNiCu and Ni-rich NiTi. The experiments performed on the first selected alloy, i.e. TiNiCu SMA, explore three major parameters: the applied stress level, the amount of actuation, and the corrosive nature of the environment. Experimental results show that SMAs undergoing transformation induced fatigue exhibit a low-cycle fatigue behavior and the measurement of the accumulated plastic strain at failure is associated to a Manson-Coffin type failure criterion. Investigations conducted on the post-mortem microstructure showed evidence of a multiphysical coupling between corrosion and cyclic phase transformation, from which a novel cyclic damage mechanism is proposed and explained using the micromechanical shear lag model accounting for actuation and accumulated plastic strains. Thereafter, based upon the identified failure mechanism and considering damage accumulation through crack formation, a stress renormalization procedure is proposed in combination with the Miner's rule to predict the reduction of number of cycles to failure due to cyclic phase transformation and corrosion. A direct method is first presented and the predictions show good agreement with experimental results. However, both corrosion and corrosion-free fatigue data are required. Therefore, a new approach is proposed: the inverse Miner's rule, which requires corrosion fatigue data only to predict corrosion-free life. The new and attractive properties of the selected second alloy, i.e. Ni-rich NiTi SMA, have revived the motivation of the aerospace industry to design SMA actuators. One particular property is cyclic stability generated by precipitation hardening mechanism using Ni_4Ti_3 precipitates. However, Ni_3Ti are also precipitates due to high Nickel content (60 wt.% or 55 at.%). Parameters such as processing, heat treatments, size effects, surface quality and environment are investigated. Thermomechanical response and fatigue life are discussed and the greatest impact is found to come from specimen surface quality. Finally, a detailed fractography presents the different microstructural aspects of the fatigue damage and concludes to a precipitation driven fatigue failure mechanism cause by Ni_3Ti precipitates.

DEDICATION

To my Parents,

Jacqueline and Serge

ACKNOWLEDGEMENTS

I would like to express my deepest gratitude to my committee chair, Dr. Dimitris C. Lagoudas, for his mentorship, leadership and devotion to his students. Not only did he help me achieve my research goals, but he also taught me the importance of being responsible for one another, the importance of listening and, by example, of being dedicated to my goals, passions and motivations; for all this, I cannot thank him enough. I would also like to express my appreciation to my committee members, Dr. James G. Boyd, Dr. Vikram K. Kinra, Dr. Ibrahim Karaman and Dr. Gary T. Fry, for their guidance and thoughtful comments throughout my research.

I want to express my sincere appreciation to my undergraduate advisor, PhD mentor, and co-advisor, Dr. Etienne Patoor, whom I met when I was working at the Ecole Nationale Supérieure D'Arts et Métiers in Metz, France. He maintained a never ending trust and confidence throughout the hard years I spent working on my research at Texas A&M University.

Thanks also to my coworkers, friends and confidants, with whom I had a tremendous social and working experience. Sharing our research, life objectives and cultural origins was more than an enriching experience. Whatever direction my work will take in the future, I will always remember the years of hardship and mutual motivation when times were more than difficult.

Among the great friends I made during these years of hardship, I want to acknowledge: Justin Schick, who has been working on his master's since Spring of 2007

and who has been helping me consolidate the work I have started for the project with the Boeing Company; Dr. Hongxing Zheng, a post-doctoral researcher who came from China and helped me on many discussions and microstructure analysis for the past year; and Dr. George Chatzigeorgiou, who is my officemate and who provided me with professional, mental and personal support. I cannot forget my seniors, who supported me in the hardest personal and professional times, Dr. Luciano Machado, Dr. Gary Don Seidel, Dr. Pavlin Entchev, Dr. Bjorn Kiefer and Olivier Godard, who were graduate students when I started my studies at A&M and who now are successful professionals, in both academia and industry. Finally, I would feel guilty not to mention the great friends with whom I started this amazing journey, progressed with, suffered with, deeply discussed, with and laughed so much with: my lab-mate of nearly four years, Darren Hartl; Parikshith Kumar, who was just a few doors away in the basement of the Bright Building; Piyush Thakre and Amnaya Awasthi, who taught me about their culture, philosophy and approach to science and humanity. To all of you and to the ones I may have forgotten, I say deeply, thank for becoming some of my greatest friends.

I would like to acknowledge the support of the Boeing Company, which allowed me to continue and finish my research on a project that went beyond my thoughts of excitement on a research topic. I would like to especially thank Dr. Frederick T. Calkins and James J. Mabe for the leadership, knowledge and experience they shared during the past three years of interactions.

On a more personal note, I would like to thank my first post-high school mathematics teacher, Marcel Pantani. He was the first person to support me with his will to make me succeed, when I was going through the loss of my mother. He will always have a special place in my heart and will always be part of my success.

I would like to acknowledge my home town, Saint-Raphaël, the charming little city located in the French Riviera, which I have seen growing and becoming more and more beautiful over the years, and this, mostly due to the active involvement and love of its National Assembly Deputy and Mayor, Mr. Georges Ginesta. It is the place where I was born and lived until I moved to start my higher education. It is where my dreams and desire to pursue greater studies were motivated by the precious advice and by the trust from my middle and high school teachers. I will always carry proudly my origins and my culture that I love so much and that I want to share with the international community I interact with every day.

I cannot express my gratitude without thinking of my parents, Jacqueline Gallice Bertacchini and Serge Bertacchini. My mother Jacqueline sadly left this world during the first year of my undergraduate program, which made things very difficult on multiple levels. Her immeasurable love and life lessons only strengthened me to an unbreakable perseverance. My father, Serge, was, and is still, one who has always been behind my dreams and helped me thrive and raise my head when everything was dark around me. He supported me financially and emotionally, in thought and in person, when he surprised me with his first visit to College Station during my first year at Texas A&M University.

I want to acknowledge the patience and understanding of my older brother Fabien and his wife Muriel, who, despite the distance and the very scarce moments we see each other, always supported my objectives and personal choices. They gave birth to three lovely children, Damien, my dearest godson, Raphaël, and the adorable little Marie whom I haven't gotten the chance yet to meet in person.

After the passing away of my dear Mother, I had to go live with very close friends of my family, who gave me love, a comfortable environment, and an emotional support that bound each one of us in an emotional connection that goes beyond friendship. They are family and in my heart every day. Without Anna and Serge Despres, their sons Frederic, Laurent and Julien, I probably would never have had the privilege to write this dissertation. When I arrived here in Texas, I found the same unconditional love and support from whom I consider my American family, Mr. and Mrs. May, their daughter Robin, and Carlos, their son, my brother.

Finally, I express my deep consideration and respect to someone who took me as her son, Beatrice Lantenois. She is my step-mother, trusted friend, confidante and model of balance between work and family. She is a successful businesswoman and a wonderful mother for my stepbrother and stepsister, Florent and Julie. They gave me the greatest joy when they came to visit me, to see my work with Dr. Lagoudas, and to motivate me for the last long stretch of work before preparing for my dissertation defense.

To every one of you, and everyone who had a role in my personal and professional development, I thank you from the bottom of my heart.

NOMENCLATURE

R	external radius of SMA actuator
e	thickness of the cracked surface layer
δ	distance between two consecutive cracks
c_{SMA}	SMA core volume fraction reduced to area fraction due to axisymmetry
c_{TiO_2}	oxide volume fraction reduced to area fraction due to axisymmetry
c_{SL}	surface layer (SL) volume fraction reduced to area fraction due to axisymmetry
σ_{zz}^{SMA}	stress in SMA core
σ_{zz}^{SL}	stress in surface layer (SL)
τ	interfacial shear stress between SMA core and surface layer SL
$\left\langle f^{SMA} \right\rangle$	average of any variable f^{SMA} over the cross-sectional area of the SMA core
$\left\langle f^{SL} \right\rangle$	average of any variable f^{SL} over the cross-sectional area of the surface layer (SL)
u_z^{SMA}	displacement in SMA core
u_z^{SL}	displacement in surface layer (SL)
ε_{zz}^{SMA}	total strain in SMA core
ε_{zz}^{SL}	total strain in surface layer (SL)
ε_{in}^{SMA}	inelastic strain in SMA core
ε_{in}^{SL}	inelastic strain in surface layer (SL)

E^{SMA}	Young's modulus in SMA core
E^{SL}	Young's modulus in surface layer (SL)
μ^{SMA}	shear modulus in SMA core
μ^{SL}	shear modulus in surface layer (SL)
$\sigma_{applied}$	nominal constant stress applied to SMA actuator
σ_{renorm}	renormalized stress level in SMA core due to presence of circumferential cracks
γ	surface layer evolution (crack depth) coefficient
N	number of thermal cycles attained at stress level $\sigma_{renorm}(N)$
N^*	number of cycles to failure under corrosion-free conditions
$\sigma_{corr}(N_f)$	stress-life equation in corrosive conditions
$\sigma^*(N^*)$	stress-life equation in corrosion-free conditions
A^*, B^*	corrosion-free stress-life equation coefficients
A_{corr}, B_{corr}	corrosion stress-life equation coefficients
dN	infinitesimal number of cycles consumed at stress level $\sigma_{renorm}(N)$
dD	infinitesimal damage fraction at stress level $\sigma_{renorm}(N)$

TABLE OF CONTENTS

Page

CHAPTER

Page

CHAPTER

Page

CHAPTER

Page

CHAPTER

LIST OF FIGURES

Page

Page

Page

Page

LIST OF TABLES

Page

CHAPTER I

INTRODUCTION TO SHAPE MEMORY ALLOYS, CYCLIC LOADING AND FATIGUE

1.1. Transformation induced fatigue in SMAs

SMAs are sensitive to the thermomechanical loading path they are subject to. The two common loading paths applied to SMAs are pseudoelastic and constant load thermal cycling [1]. The first type is mostly utilized by medical engineering applications that require large deformations and recovery under cyclic mechanical loading. To exhibit pseudoelastic response, SMAs require being in austenite, fully or partially, at a selected test temperature. Therefore, SMAs can exhibit pseudoelastic response only if the test temperature is above the austenite start temperature ($T > A_s$). Upon mechanical loading, austenite transforms into martensite. The transformation is complete if the martensite is fully detwinned and the transformation strain attains its maximum. The transformation is partial if the martensite is partially detwinned and therefore the transformation strain does not reach its maximum value. At temperatures above the austenite finish temperature ($T \geq A_f$), complete shape recovery upon mechanical unloading is observed. At temperatures comprised between the austenite start and finish temperatures ($A_s < T < A_f$) partial shape recovery is observed. The second type of loading path,

---

This dissertation follows the style of International Journal of Fatigue.

referred to as constant stress loading path, is an idealization of typical loading paths used by the aerospace engineering industry that utilize SMAs as actuators subject to mechanical loading under temperature variations. Constant mechanical loading is used to induce detwinning of the martensite upon cooling. The deformation achieves its maximum when the temperature of the SMA is lower than the martensitic finish temperature ($T \leq M_f$). It is when the SMA actuator is heated above the austenite finish temperature ($T \geq A_f$) that full recovery occurs from martensite to austenite. The applied loading path, pseudoelastic or constant stress, can be selected so that the SMA fully transforms from one phase to the other, thus defining complete transformation cycles. Moreover, it is possible to limit the transformation and permit partial forward transformation and partial recovery, i.e. partial transformation cycles.

The fatigue life response of SMAs can be divided into two categories, high-cycle fatigue and low-cycle fatigue. High-cycle fatigue of SMAs can be seen in the first generation of medical applications such as stents, periodontal wires, bone replacement and supporting structures. These applications involve cyclic mechanical loading and often refer to either elastic cyclic loading of the austenitic parent phase of the SMA or to pseudoelastic cyclic loading at low strain amplitudes. Tobushi et al. [2], Miyazaki et al. [3] and more recently, Furuichi et al. [4] and Gall and Maier [5] have shown that for low total strain amplitudes ($< 1\%$), SMAs can demonstrate fatigue limits larger than a million cycles. It is only recently that the medical industry has been focusing on the influence of high amplitude cyclic straining of pseudoelastic SMAs. The results showed fatigue limits below ten thousand cycles under extreme conditions and the reduced number of cycles compared to low amplitude cyclic straining was attributed to the accumulation of permanent deformations [6, 7].

Over the last decade, mechanical, medical and aerospace industries have seen the growing use of Shape Memory Alloys (SMAs) [8, 9]. The thermomechanical response of SMAs subject to various mechanical and thermal loads resulting in a cyclic phase transformation has been widely investigated. The influence of different thermomechanical loading paths on the stabilization of the transformation strain and on the accumulation of plastic strain has also been investigated [10]. However, most of the results pertain to a limited number of cycles and mainly focus on the development and stability of stress-assisted two-way transformation strain and the evolution of plastic strain [11, 12, 13].

The recent development of various aerospace applications such as SMA actuated flaps, blades and noise reduction devices further motivates the need to investigate and characterize the response of shape memory alloys actuators [14, 15]. Thermal cyclic loading of SMA actuators subject to mechanical loads, either constant or variable, results in martensitic phase transformation with an associated maximum recoverable strain in the order of three to five percent in most common polycrystalline shape memory alloys [1, 9]. The result from the repeated actuation of SMAs is the accumulation of transformation induced plasticity and the reduced fatigue limit of the SMA to a low-cycle fatigue regime. Some early studies on the fatigue of SMA actuators have confirmed a low-cycle fatigue behavior with significant accumulation of plastic strain, which leads to failure of the SMA actuators below ten thousand cycles under extreme loading conditions [16, 17, 18, 19, 20]. This behavior is characteristic of SMAs and is defined as transformation induced fatigue.

Transformation induced fatigue can be found under both pseudoelastic cyclic loading [2, 3, 4, 5, 6, 20, 21] and constant load thermal cycling [12, 16, 17, 18, 19]. The first one uses a representation of the fatigue life using alternating stain plotted versus the number of cycles to failure using the well-known rotating-bending fatigue apparatus. Miyazaki et al. [3] used this methodology extensively to generate fatigue pseudoelastic transformation induced fatigue data and a summary is presented in Figure 1 and Figure 2.

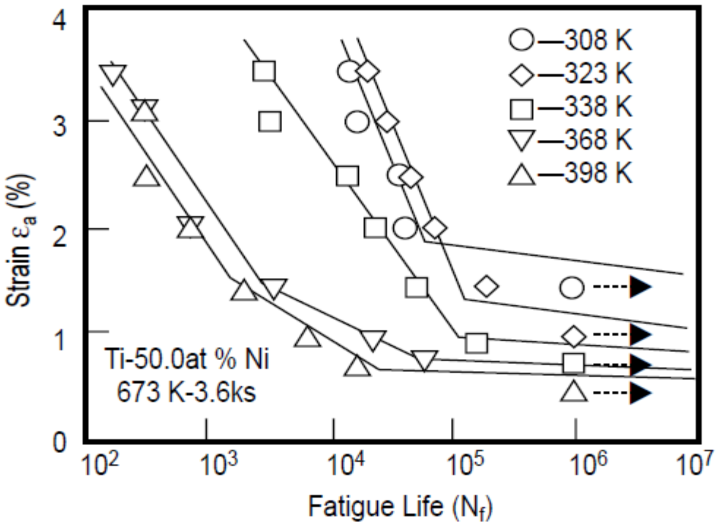

Figure 1. Strain-life curves for NiTi alloys, with test temperatures indicated on the plots. The specimens were annealed at 673 K for 1 hour [3].

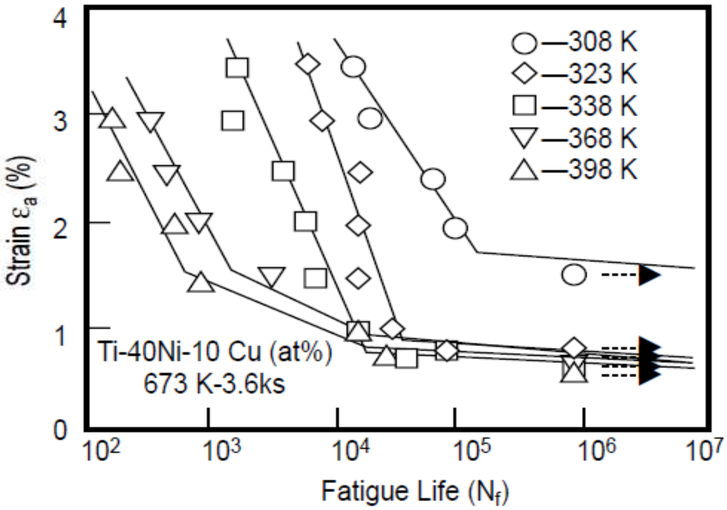

Figure 2. Strain-life curves for TiNiCu alloys, with test temperatures indicated on the plots. The specimens were annealed at 673 K for 1 hour [3].

Cycles to failures are found to range between 100 and beyond 1,000,000 for strain ranges comprised between less 0.7% and 3.5%, for both NiTi and TiNiCu SMAs, showing how reducing the amount of transformation greatly reduces the transformation induced fatigue life. In the case of constant load thermally induced transformation fatigue, a new standard is being established due to the need to control both the actuation through temperature and the level of applied load. Therefore, constant load thermally induced transformation fatigue is mostly represented in terms of the applied stress versus the number of cycles to failure [18, 22, 23, 24]. Bigeon and Morin [16], Proft et al. [25] and Lagoudas at al. [22] have investigated the constant load thermally induced transformation fatigue of the particular TiNiCu SMA alloy and found, despite certain discrepancies, similar fatigue response. However, the key observation is the absence of fatigue limit compared to pseudoelastic transformation induced fatigue.

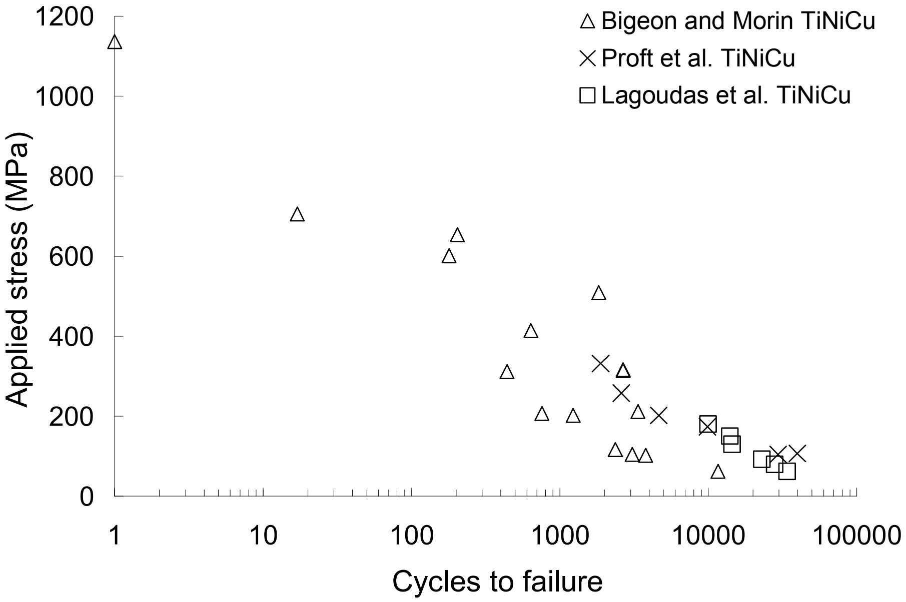

Figure 3. Constant load (stress) thermally induced transformation fatigue for $Ti_{50}Ni_{40}Cu_{10}$ SMA actuators from three different experimental setups [16, 22, 25].

Lagoudas et al. [18, 22], Bertacchini et al. [23, 26] and Bhaumik et al. [24] investigated the role of partial transformation cycles on the transformation induced fatigue life of SMA actuators and consistently found an improvement of the number of cycles to failure of nearly an order of magnitude, which confirms the initial observations of improved fatigue performance under reduced amount of actuation, i.e. cycles through smaller volume fraction of martensite.

1.2. Cyclic loading and damage nucleation

When considering SMAs as actuators, it is important to understand the effect of repeated martensitic phase transformation on the overall thermomechanical behavior as well as on the evolution of the microstructure in the material. The cooling of an SMA component below the martensitic transformation temperatures results in the nucleation of untwinned martensite and upon the application of a constant stress, results in the reorientation of the martensite causing the SMA to exhibit a recoverable strain in the order of 3% to 5 % in most polycrystalline SMAs. Upon heating above the austenite transformation temperatures, the SMA component transforms back into its parent phase, thus recovering most of the inelastic strain generated upon cooling under stress, where the remaining unrecovered strain is attributed to transformation induced plasticity (TRIP) [18, 27] and stabilized martensite [28, 29, 30]. Such transformation mechanism, repeated over a large number of cycles, induces an evolution of the microstructure. The work by Lagoudas et al. [18, 22], Tamura et al. [21] and Morgan and Friend [27] demonstrate microstructural evolutions resulting in the modification of the transformation temperatures, hysteresis and stability of the recoverable strain.

The thermomechanical response of an SMA actuator is strongly dependent on its microstructure, but one major aspect influencing the fatigue life is the existence of surface defects. Recent studies by Hornbogen and Eggeler [31, 32] focus on the role of surface quality in the fatigue life of shape memory alloys. The actuation strain an SMA produces is recoverable but induces the formation of irreversible strains, which contribute to a crack nucleation process. Processes such as wire drawing can lead to residual stresses and defects at the surface of the SMA, which under cyclic loading will favor the nucleation and growth of microcracks. In addition, the repeated martensitic transformation results in irreversible surface processes. The accumulation of plastic strain is usually seen as beneficial to delay crack propagation but also leads to the formation of defects, such as alternated surface extrusions and intrusions [33]. Studies by Figueiredo et al. [20] showed the influence of the amount of transformation on the crack formation and final failure of SMAs. Under cyclic loading, the formation of cracks is generally initiated at the surface, and progresses slowly until the crack becomes unstable. This characteristic can also be found in SMAs. Recent studies showed the influence of the amount of transformation on the fracture surface and final failure as well as supporting evidence of surface crack initiation and propagation in SMAs under various loading conditions [34]. Supporting evidence of surface crack initiation and propagation in SMAs under various loading conditions and various specimen geometries are discussed in the work by Figueiredo et al. [20] and by Cheung and Darvell [34].

The main cause of fatigue damage in SMAs comes from TRIP, resulting in low-cycle fatigue. However, oxidation and corrosion are phenomena that can accelerate damage formation under cyclic loading and therefore contributing to a reduction of the fatigue life [35]. The aerospace industry has been dealing with high temperature materials since the emergence of jet engines, which require materials sustaining cyclic loading at elevated operating temperatures [36, 37]. The emergence of high temperature shape memory alloys (HTSMAs) for aerospace applications is another important example of the coupling between oxidation temperatures and cyclic loading [38]. It is even more important as SMAs exhibit large inelastic reversible strains that can significantly add to the complexity of the coupling between oxidation and cyclic phase transformation [39]. Finally, SMAs are known for their low actuation frequencies. The heating and cooling rates of TiNiCu SMA wires are discussed in the work of Miller [40], Lagoudas et al. [22] and of Bertacchini et al. [23], and it is found that a direct way to enhance the actuation frequency was to combine Joule resistive heating with forced fluid convective cooling. SMAs are no different than other alloys and compositions such as the equiatomic NiTi SMA have shown excellent resistance to corrosion [41, 42]. However, the consequence of the improvement of the actuation frequency through combination of Joule resistive heating and forced fluid convective cooling is the formation of a corrosive environment that operates at temperatures much below conventional oxidation temperatures. Therefore, one has to assess the working conditions and environment of the SMA actuators to take into account a possible coupling between oxidation and transformation induced fatigue of SMAs.

1.3. Alloy compositions and applications

NiTi SMAs have been the primary focus for actuation applications. However, the addition of ternary elements can change the response of the SMA while maintaining similar thermomechanical properties. The addition of Cu so that the new alloy composition becomes $\mathrm{Ti_{50}Ni_{50-x}Cu_x}$ with a maximum of 10 at.% Cu substitution, contributes to lower values of latent heat of transformation. This allows smoother phase transitions, lower amount of accumulated non-reversible plastic strains, smaller hysteresis and absence of intermediate R-phase transformation [10]. However, the substitution of Nickel for Copper in proportions up to 10 at.% slightly reduces the fatigue life of the alloy [3]. This trend has been observed for fatigue tests under either pseudoelastic or thermomechanical cyclic loading. Some of those investigations focused on the $Ti_{50}Ni_{45}Cu_5$ alloy composition [24, 43]. Results showed improved fatigue life and stabilized hysteresis loop in the case of trained and partially actuated SMAs.

With the purpose of developing new actuation technologies incorporating active materials, including the design of systems providing significant noise reduction of commercial aircrafts, engineers from the Boeing Company have been investigating the use of Shape Memory Alloys (SMAs) as actuators [14]. Ni-rich SMAs are used as beam actuator and are clamped to a serrated aerodynamic structure placed on the nozzle of a jet engine. The purpose of such a design is to induce actuation in the SMA beam components, producing a deflection of the variable geometry chevrons (VGC). Such deflection causes the fan flow to vary and to be less turbulent during take-off and landing, resulting in significant noise reduction [15].

Nickel rich binary NiTi SMAs differ from the conventional and widely spread near equiatomic NiTi [44]. The larger proportion of nickel content results in the formation of a second metastable phase in the nickel-rich matrix. For alloys with a Ni content ranging between 57 wt.% and 60 wt.%, the NiTi binary phase diagram shows formation of a secondary stable phase, i.e. Ni_3Ti. Intermediate precipitates can be formed due to both the high Nickel content of the matrix and the presence of the stable Ni_3Ti, i.e. Ni_4Ti_3 and Ni_3Ti_2 [45, 46]. The composition of the alloy sets the proportions between the two stable phases NiTi and Ni_3Ti. The size, distribution and concentration of precipitates, resulting in modifications of the matrix composition, can be tuned during heat treatments. A common approach to those alloys is a shape set heat treatment following the hot rolling process. The shape set is a heat treatment performed to adjust an SMA component to a desired shape while maintaining its transformation behavior. The shape set heat treatment is a high temperature treatment that allows diffusion of atoms with homogenization of the post hot-rolling microstructure; the cooling is usually slow and controlled. A second thermal treatment is applied after shape set, i.e. aging. The aging treatment is used at ranges where only metastable precipitation occurs and therefore water quenching is necessary to stabilize such precipitates [45]. The control of the time and of the temperature of the aging treatment allows adjusting the proportion of nickel exchanged between the nickel-rich matrix and the nickel-rich precipitates. This adjustment treatment is proven to be highly effective in tuning the transformation temperatures as well as the hysteresis [47]. In addition to controlling the transformation temperatures and the hysteresis, the nickel-rich $Ni_{60}Ti_{40}$ demonstrated excellent actuation response in terms of number of cycles to reach stable actuation response as well as creep-like behavior upon variable loading [48, 49]. These results made the nickel-rich $Ni_{60}Ti_{40}$ SMA actuators the primary candidate for future experimental testing and applications.

The diffusion of nickel in the binary matrix and in the formed nickel rich precipitates creates local concentration gradients that not only affect the local composition, but also the local behavior [50]. The sensitivity of Ms to nickel content is such that a gradient of concentration results in neighboring material points with different shape memory properties [3, 50]. In addition to concentration gradients, the growth of precipitates results in the distortion of the NiTi lattice. The consequence is the formation of stress concentration gradients surrounding the precipitates. When the precipitates are small enough to only induce elastic distortion, the precipitation is coherent. However, the formation of large precipitates usually leads to non-coherent precipitates due to large deformations [45, 51].

In previous research efforts, development, characterization and modeling of the material were the main objectives with little effort dedicated to the understanding of the materials fatigue behavior [52]. As the nickel-rich SMAs undergo hot rolling followed by homogenization treatment as well as precipitate formation, the maximum transformation strain that these alloys can generate is up to ~1.4% under monotonic thermomechanical loading on ASTM standard test specimens [48, 52]. As a material never before tested under cyclic conditions until failure, it becomes important to differentiate a two-level mechanism that dictates the behavior of Ni-rich NiTi SMA actuators. The first consists of global phenomena such as the accumulation of plastic strain and the overall effect of the externally applied stress, which lead to the macroscopic response and stabilization of the actuator. The second concerns the local mechanisms that dictate the failure mechanisms involved in the fatigue failure of such alloys. Corrosion, surface effects, interactions between possible precipitates and matrix can easily lead to defect generation and propagation, ultimately leading to the failure of the SMA component, as summarized in Figure 4.

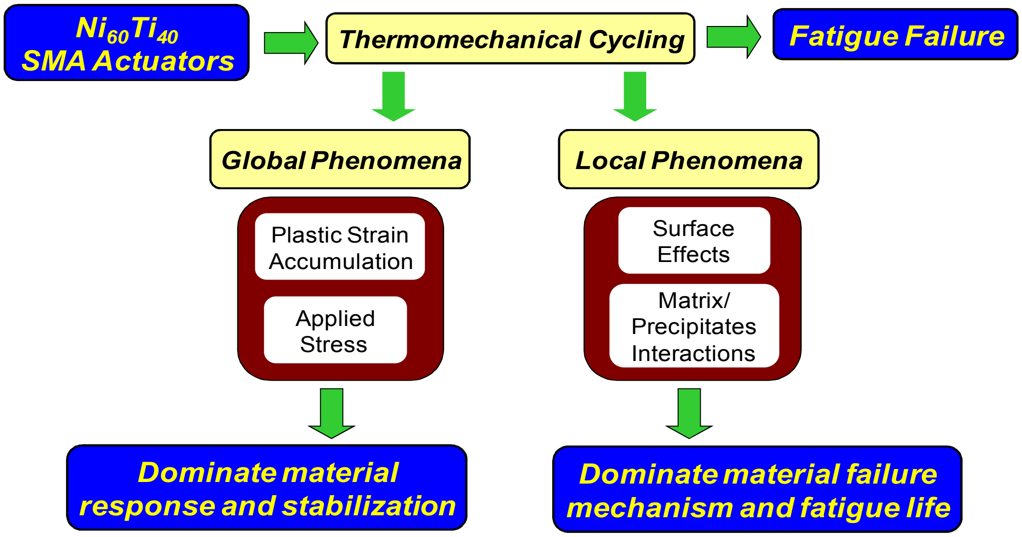

Figure 4. Effects of cycling and definition of global and local phenomena dictating the materials response, failure and fatigue life.

As the knowledge and technology for SMAs used as actuators continues to mature, the understanding and assessment of the transformation induced fatigue behavior has now become pertinent. The need for transformation induced fatigue life characterization of nickel-rich SMAs for the Boeing VGC application turns into a priority as this structural active component is subject repeated loading for approximately 20,000 to 70,000 flight cycles. $Ni_{60}Ti_{40}$ SMA actuators are no different in terms of high amplitude straining due to full martensitic detwinning induced upon thermal cyclic loading and therefore exhibit a low-cycle fatigue behavior. Large amounts of plastic strain have been reported to be stabilized upon application of the appropriate thermomechanical training [48, 52]. Therefore, it is important to acknowledge the fact that such SMA actuators will develop large amounts of plastic strain in counterpart of being highly competitive in terms of large energy density actuators. However, such application involving low-cycle fatigue behavior requires being accepted and certified. Such certification requires the definition of testing standards and compliance to safety coefficients ensuring a fatigue life beyond the targeted life during service. Transformation induced fatigue life characterization becomes a significant challenge to the integration of such promising materials in one of the first major large scale SMA aerospace applications.

CHAPTER II

TRANSFORMATION INDUCED FATIGUE OF TiNiCu SMA ACTUATORS: EXPERIMENTS AND RESULTS*

In this Chapter, the transformation induced fatigue of TiNiCu SMA wire actuators undergoing thermally induced martensitic phase transformation in a corrosive environment is investigated. The main objective of this work is to evaluate the cyclic response and fatigue behavior of TiNiCu SMA wire under corrosive conditions and to compare it to results obtained for fatigue testing in a corrosion-free environment. Chapter II focuses on various experimental aspects, including the presentation of fatigue results as a function of various testing parameters. The variable test parameters are five applied stress levels from about 50 MPa to about 250 MPa, and two different actuation strains, one corresponding to complete transformation cycles and the other to partial transformation cycles. The results from fatigue testing in a corrosive environment show a consistent reduction of the fatigue life compared to corrosion-free fatigue results, in both complete and partial transformation conditions. It is also observed that corrosion-assisted fatigue leads to more scattered fatigue data and this spread is mostly attributed to enhanced and accelerated damage mechanisms due to corrosion. Finally, the accumulated plastic strain is correlated to a Manson-Coffin fatigue failure criterion

---

*Part of this chapter is reprinted with permission from "Thermomechanical transformation fatigue of TiNiCu SMA actuators under a corrosive environment – Part I: experimental results" by Bertacchini O W, Lagoudas D C and Patoor E., 2009. *International Journal of Fatigue*, 31, 1571–78, Copyright 2009 by Elsevier.

and it is shown how TiNiCu SMA wire actuators exhibit a fatigue life depend on the amount of accumulated plastic strain.

2.1. Experiments

2.1.1. Experimental setup

The fatigue testing involved in this study consisted of thermomechanical cycles under constant stress conditions in a custom-built fatigue test frame [22, 26]. Figure 5 and Figure 6 describe the experimental setup that was used to perform fatigue testing. Figure 5 illustrates the different constituents of the fatigue frame, while Figure 6 shows an overview of the experimental setup and the different constituting parts.

One end of the SMA actuator is connected to the rigidly anchored aluminum frame, while the other end is connected to a kevlar cable passing through the pulley-system shown in Figure 5, and is referred to as free-end.

The frictionless pulley-system is designed to transfer the vertical loads from the hanging weights to the horizontally positioned SMA wires. The constant loads acting on the SMA actuators result in constant stress conditions. The SMA is heated using resistive Joule heating and is cooled through forced fluid convection. The induced resistive heating resulted in temperature change from about 10°C to about 120°C in one second. The selected cooling fluid is an ASTM certified engine coolant. The measurement of the displacements is performed using linear variable displacements transducers (LVDT), as shown in Figure 6.

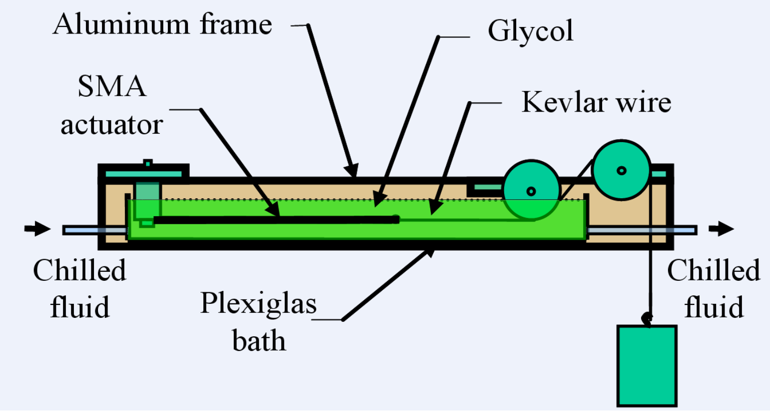

Figure 5. Schematic of the experimental fatigue test frame, side view.

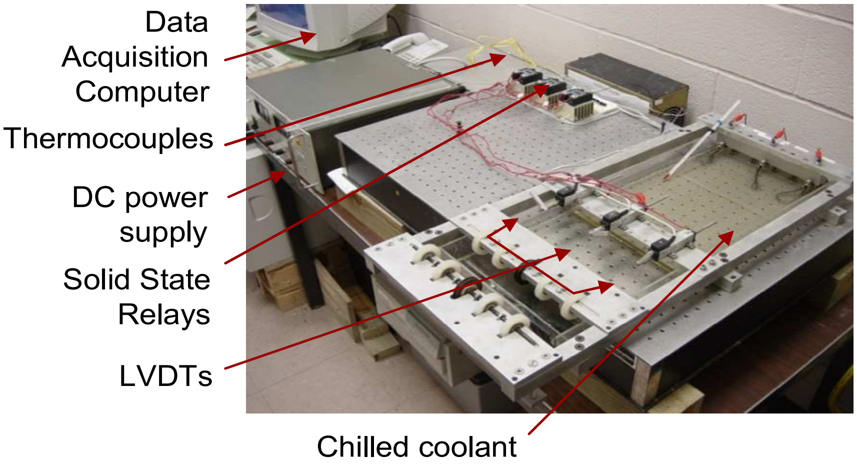

Figure 6. Picture of custom built constant stress fatigue test frame using forced fluid glycol coolant.

The cooling methodology is selected to provide enhanced cooling capacity as well as to induce corrosion. In order to maintain a 10°C temperature in the open bath

(Figure 6), the fluid is circulated through a heat exchanger subjecting the coolant to negative temperatures. Therefore, an ASTM certified antifreeze engine coolant is selected. A total time of approximately three seconds is needed to cool the SMA wires from 120°C to 10°C. The coolant was a low-viscosity mixture of water, ethylene glycol and diethylene glycol chosen to provide good heat transfer capacity [18, 22, 40]. The fluid also contained corrosion inhibitors and alkali compounds to limit acidity formation.

In a preliminary work focusing on the thermomechanical fatigue of SMA wire actuators, series of tests were conducted under similar loading conditions in a corrosion-free environment, where natural convective cooling using cold air was achieved in a refrigerated chamber [18, 22, 40]. The corrosion-free fatigue data will be compared to this study's corrosion fatigue data and will be discussed in the next section.

2.1.2. Methodology and control of actuation

The LVDTs continuously recorded the position of the free-end of the actuator and two different positions were recorded per thermal cycle: one position upon completion of heating, i.e. x_k^A, and the other upon completion of cooling, i.e. x_k^M, where $k$represents the number of cycles. Subsequently, it was possible to normalize the displacements by the initial length of the actuators L_{init} and to define the total strain terms ε_k^A and ε_k^M associated with the austenitic phase and with the martensitic phase, respectively, as shown in Eq. (1).

$$\varepsilon_k^A = \frac{x_k^A - x_1^A}{L_{init}}; \varepsilon_k^M = \frac{x_k^M - x_1^A}{L_{init}}; k = 1, 2 \ldots \quad (1)$$

The SMA actuators were mounted into the frame, cooled from T_0 to $T_{\min}$ and loaded from zero to σ_0 constant stress inducing detwinning of the martensite, as indicated in Figure 7, for both complete and partial transformation cycles, i.e. 100% actuation and 50% actuation, respectively. Figure 8 and Figure 9 represent the recording of the strains in austenite and martensite for complete and partial transformation, respectively, during the first four cycles of testing.

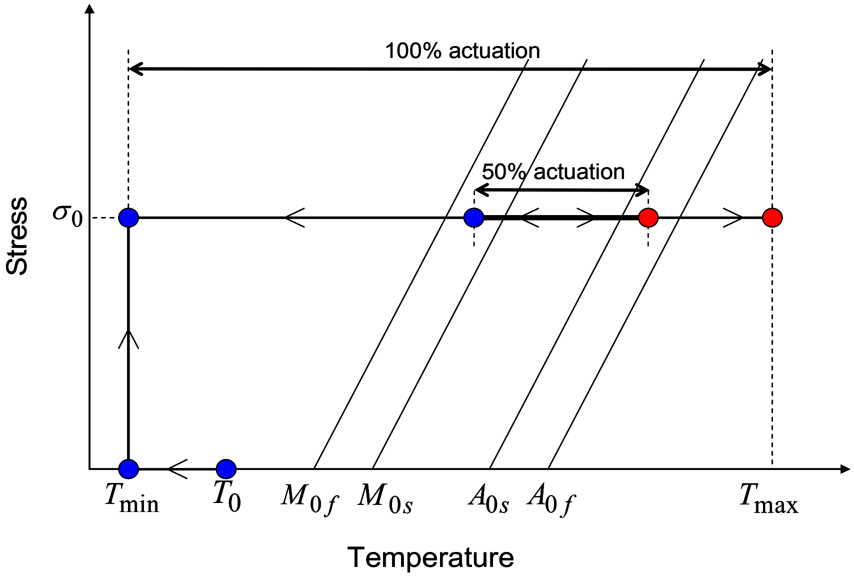

Figure 7. Representative stress-temperature phase diagram and loading path corresponding to complete and partial transformation cycles.

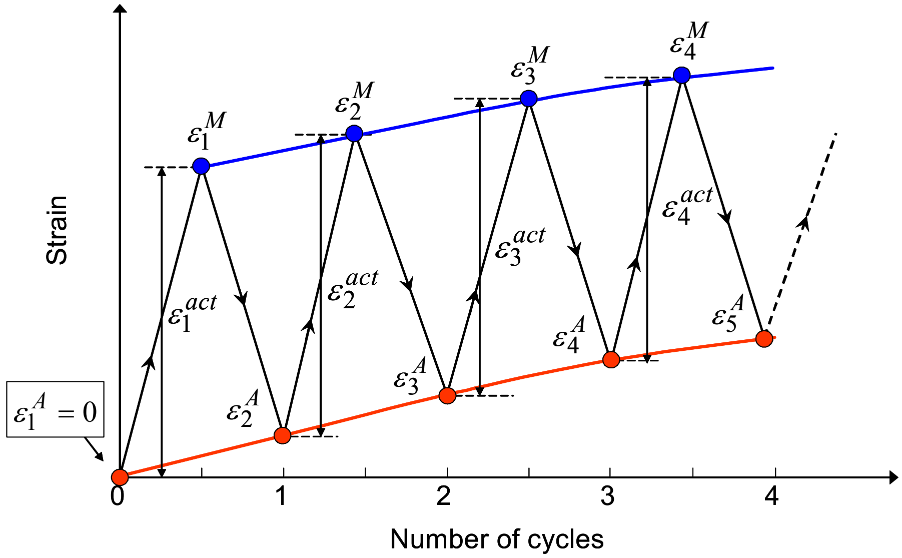

Figure 8. Interpretation of the strains in martensite, austenite and actuation strain as a function of the number of cycles under complete transformation conditions.

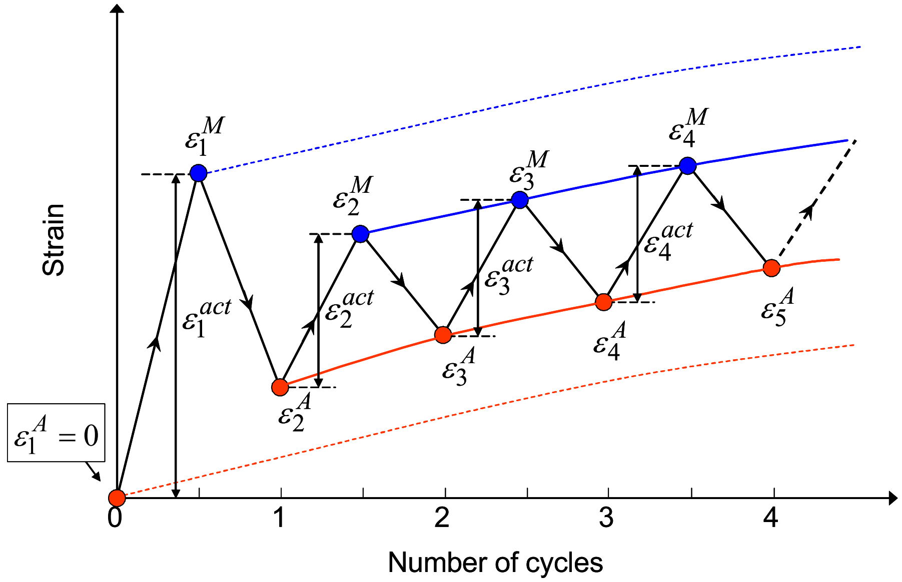

Figure 9. Interpretation of the strains in martensite, austenite and actuation strain as a function of the number of cycles under partial transformation conditions.

The dashed lines shown in Figure 9 indicate the strain levels attained during full actuation while the solid lines correspond to partial actuation. The actuation strain is the measurement of the net elongation of the SMA wire actuator, normalized by the initial length between two consecutive heating and cooling positions and is defined in Eq. (2).

$$\varepsilon_k^{act} = \frac{x_k^M - x_k^A}{L_{init}} = \varepsilon_k^M - \varepsilon_k^A \tag{2}$$

In this work, we neglected the formation of residual martensite and assumed accumulation of irreversible strain due to plasticity induced by transformation only. The measurement of the total strain in austenite ε_k^A , i.e. high-temperature total strain, which encompasses a plastic part ε_k^p and an elastic part, as shown in Eq. (3).

$$\varepsilon_k^A = \varepsilon_k^p + \frac{\sigma_0}{E_A} - \varepsilon_{init}^e \tag{3}$$

E_A is the elastic modulus in the austenitic phase and the initial elastic strain ε_{init}^e is used to zero the strain in austenite during the first cycle. The measurement of the total strain in martensite ε_k^M is composed of an elastic part, a plastic part ε_k^p , an inelastic part due to crystallographic reorientation of the martensite under stress H_k^σ [1], and a thermal part. The total strain in martensite, i.e. low-temperature total strain, can be written as shown in Eq. (4).

$$\varepsilon_k^M = \frac{\sigma_0}{E_M} + \varepsilon_k^p + H_k^\sigma + \alpha_{th}\Delta T - \varepsilon_{init}^e \tag{4}$$

E_M is the elastic modulus of the martensitic phase, ΔT is the thermal loading amplitude and α_{th} is the coefficient of thermal expansion assumed to have negligible influence during mixed-phase actuation and to have little influence on the overall total strain in martensite [1]. Therefore, the maximum transformation strain per cycle can be written as shown in Eq. (5).

$$H_k^{\sigma} = \varepsilon_k^{act} + \sigma_0 \frac{E_M - E_A}{E_M E_A} \tag{5}$$

For partial transformation cycles, the calculation of the total strains in austenite and in martensite takes into account the mixed-phase nature of the transformation, as shown in Figure 7. The displacement measurements and definition of strains in austenite, martensite and actuation strain follow Eqs. (1) and (2). The targeted amount of transformation strain during partial transformation can be defined using the maximum transformation H_k^{σ} and two coefficients $\lambda^{\min}$ and $\lambda^{\max}$, as shown in Figure 10. $\lambda^{\min}$ and $\lambda^{\max}$ represent the lower and upper limit of the fraction of actual transformation strain, respectively, and are expressed in Eqs. (6) and (7), as shown in Figure 10.

$$\varepsilon_{\min,k}^{t} = \lambda^{\min} H_k^{\sigma} \tag{6}$$

$$\varepsilon_{\max,k}^{t} = \lambda^{\max} H_k^{\sigma} \tag{7}$$

As the material undergoes partial phase transformation, there are no more pure phases and therefore the rule of mixtures is utilized to describe the contributions of each phase on the elastic strain, as shown in Eqs. (8) and (9).

$$\varepsilon_{\min}^{e} = \left(1 - \lambda^{\min}\right)\frac{\sigma_0}{E_A} + \lambda^{\min}\frac{\sigma_0}{E_M} \tag{8}$$

$$\varepsilon_{\max}^{e} = \left(1 - \lambda^{\max}\right)\frac{\sigma_0}{E_A} + \lambda^{\max}\frac{\sigma_0}{E_M} \tag{9}$$

The high-temperature mixed-phase strain, that is referred to as total strain in austenite ε_k^A, accounts for a plastic strain ε_k^p, for a partially recovered transformation strain $\varepsilon_{\min,k}^t$ and for a mixed-phase elastic strain $\varepsilon_{\min}^e$, as shown in Eq. (10).

$$\varepsilon_k^A = \varepsilon_k^p + \varepsilon_{\min}^e + \varepsilon_{\min,k}^t - \varepsilon_{init}^e \tag{10}$$

The definition of the low-temperature mixed-phase strain, that is referred to as total strain in martensite ε_k^M can be expressed as shown in Eq. (11).

$$\varepsilon_k^M = \varepsilon_{\max}^e + \varepsilon_k^p + \alpha_{th}\Delta T + \varepsilon_{\max,k}^t - \varepsilon_{init}^e \tag{11}$$

Therefore, the transformation strain under partial transformation cycles can then be written as shown in Eq. (12).

$$\varepsilon_k^t = \varepsilon_k^{act} + \left(\lambda^{\max} - \lambda^{\min}\right)\sigma_0 \frac{E_M - E_A}{E_M E_A} \tag{12}$$

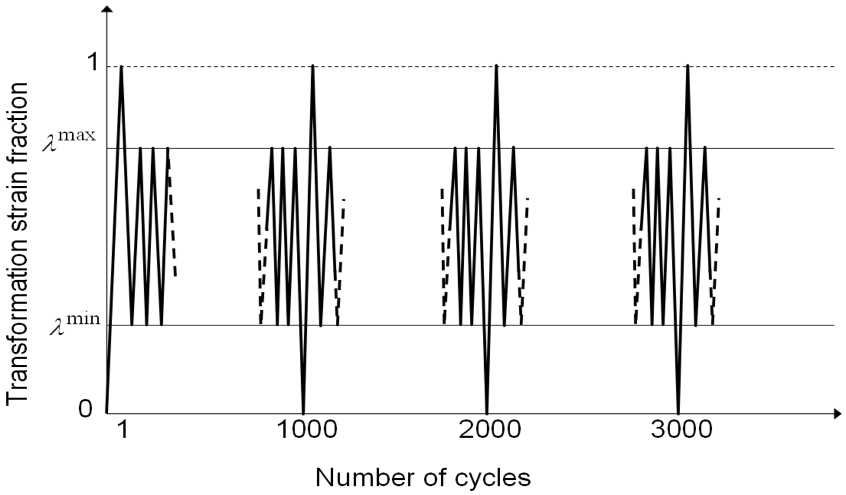

Figure 10. Loading blocks under partial transformation: a full transformation cycle is performed every 1000 cycles to evaluate any evolution of the maximum transformation strain H_k^{σ}. This process is repeated until fatigue failure of the SMA actuators.

2.1.3. Parameters and test matrix

Under constant stress loading, two parameters have a major influence on the transformation induced fatigue life of SMA actuators. The first one is the level of applied stress and the other is the amount of actuation strain. Five applied stress levels were selected ranging from about 50 MPa to about 250 MPa. The lowest stress level was limited by the onset of detwinning upon cooling [53], while the highest stress level was selected to be lower than the martensite yield limit [10, 40]. The amount of actuation strain was selected for two values, one for complete actuation, i.e. 100% maximum actuation, and one for partial actuation, i.e. 50% maximum actuation [18, 22].

The selected material was $Ti_{50}Ni_{40}Cu_{10}$ (at.%) SMA wire of 0.6 mm (0.024 in.) diameter. The gauge length was approximately 200 mm (8 in.). A 15 minutes at 550°C annealing treatment was proved beneficial to optimize the fatigue performances as well as to minimize the amount of plastic strain [18, 22, 27], therefore, this heat treatment was selected. The transformation temperatures were measured with a *Perkin Elmer Pyris 1* differential scanning calorimeter (DSC), using the intersecting tangent method. The onset and end of transformation temperatures under zero stress were, M_{0f}= 40°C, M_{0f} = 47°C, A_{0s} = 54°C and A_{0f}= 60°C and are shown in Figure 11. The test matrix introduced in Table 1 summarizes the different investigated parameters. To ensure repeatability of the fatigue experiments, three specimens were tested for each of the five load levels, for both complete and partial transformations.

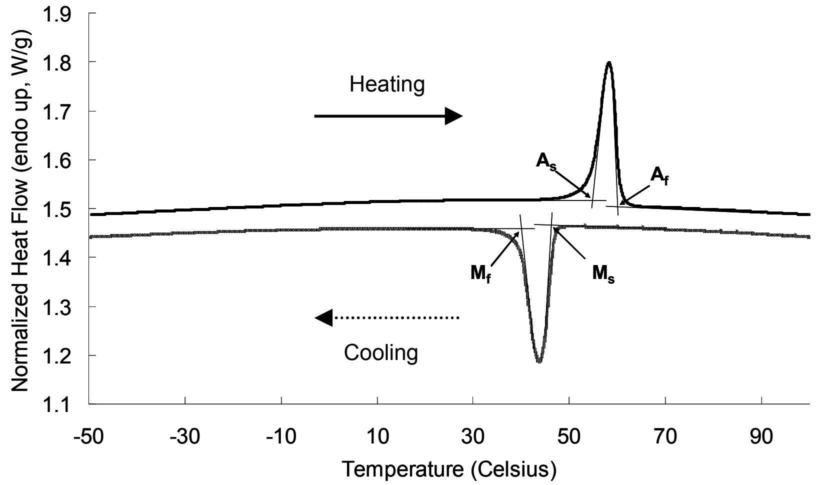

Figure 11. DSC results for TiNiCu SMA wire in a stress free condition.

Table 1. TiNiCu wire actuator transformation fatigue test matrix.

Actual Applied Stress (MPa)	54	106	154	193	247
Complete Transformation	Ic	IIc	IIIc	IVc	Vc
Partial Transformation	Ip	IIp	IIIp	IVp	Vp

Three specimens were tested for each condition.

2.2. Results and discussion

2.2.1. Influence of applied stress level

Figure 12(a) and Figure 13(a) show representative results of the evolution of the strains in martensite and in austenite as well as of the actuation strain, for complete transformation cycles under stress levels of 54 MPa and 154 MPa, respectively. Figure 12(b) and Figure 13(b) present the same results for partial transformation cycles under 54 MPa and 154 MPa, respectively.

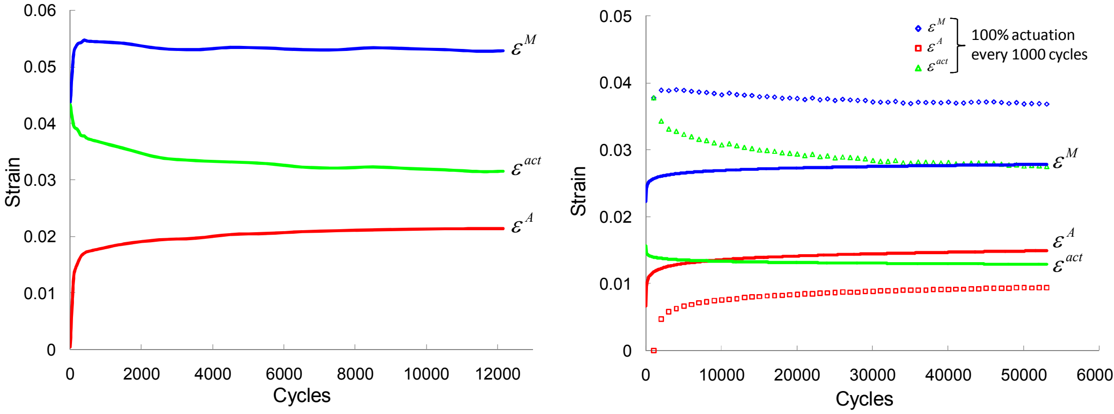

(a) (b)

Figure 12. Strain response of TiNiCu SMA actuator, thermally cycled under 54 MPa constant stress for (a) complete transformation cycles, i.e. test Ic and (b) partial transformation cycles, i.e. test Ip.

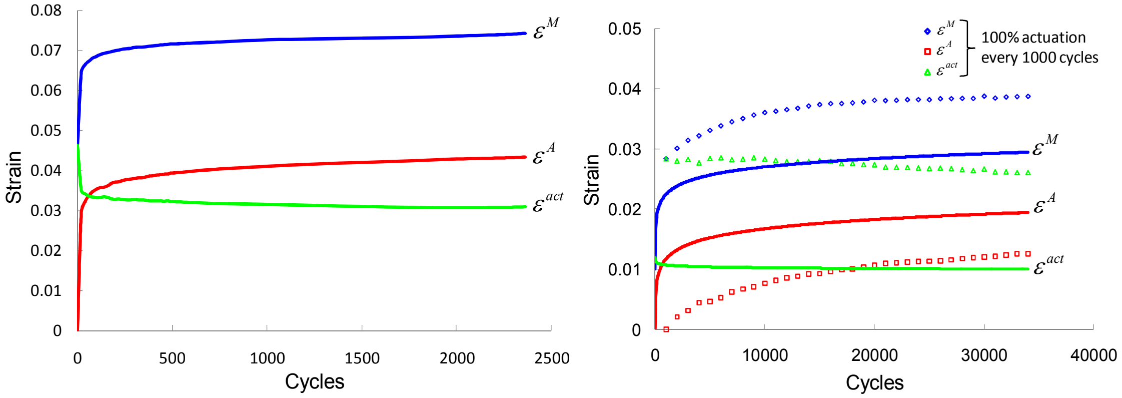

(a) (b)

Figure 13. Strain response of TiNiCu SMA actuator, thermally cycled under 154 MPa constant stress for (a) complete transformation cycles, i.e. test IIIc and (b) partial transformation cycles, i.e. test IIIp.

For complete transformation cycles, the strain in martensite demonstrates preliminary shakedown behavior over a few hundred cycles and becomes fully stable upon further cycling under low stress (54 MPa). Although preliminary shakedown is observed, at higher stresses (106 MPa and higher), the strain continues to evolve at a low rate. The resulting strain levels at failure range from an average of 5.3% to an average of 9.1%. However, the strain in austenite behaves similarly for all stress levels. The strain in austenite demonstrates a similar shakedown behavior but continues accumulating plastic strain at a low rate, resulting in averaged strain levels at failure ranging from 2.1% to 6.2%. The increase of the applied stress level above 100 MPa decreases the amount of actuation strain by approximately 0.2%, indicating saturation of the actuation performances. The higher the stress level, the more damage is generated upon cycling. Additionally, the dislocations introduced during the first thousand cycles are responsible for the reduction of the actual maximum transformation strain. Similar behavior is observed for partial transformation results with shakedown occurring over a few thousand cycles in opposition to a few hundred cycles for complete transformation.

A summary of the values obtained at failure for the strain in austenite, in martensite and for the actuation strain is given in Table 2 and the corresponding cycles to failure are summarized in Table 3. The levels of accumulated plastic strain and of actuation strain with respect to the different applied stress levels are summarized in Figure 14. The results show the influence of the applied stress level on the accumulated plastic strain at failure and therefore on the amount of stabilized actuation strain. The actuation strain decreases as the accumulated plastic strain reaches higher values under higher stresses. The amount of permanent deformations formed under high stresses reduces the amount of austenite, which transforms into martensite causing a decrease in the available actuation strain.

Table 2. Summary of strains recorded at failure for all stress levels and for both complete and partial transformation cycles.

Test conditions	Stress level (MPa)	Strain in austenite (%)				Strain in martensite (%)				Actuation strain (%)			
		Test 1	Test 2	Test 3	**Avg.**	Test 1	Test 2	Test 3	**Avg.**	Test 1	Test 2	Test 3	**Avg.**
Ic	54	2.1	1.9	2.3	**2.1**	5.2	5.0	5.6	**5.3**	3.1	3.0	3.3	**3.1**
IIc	106	2.5	2.9	3.3	**2.9**	5.7	6.4	6.5	**6.2**	3.2	3.4	3.2	**3.3**
IIIc	154	4.5	4.1	4.3	**4.3**	7.6	7.2	7.4	**7.4**	3.1	3.0	3.1	**3.1**
IVc	193	5.2	4.7	5.4	**5.1**	8.2	7.5	8.0	**7.9**	3.0	2.8	2.6	**2.8**
Vc	247	5.9	6.2	6.4	**6.2**	8.9	9.0	9.4	**9.1**	2.9	2.8	3.0	**2.9**
Ip	54	1.5	1.7	1.5	**1.5**	2.6	2.9	2.7	**2.7**	1.1	1.2	1.2	**1.2**
IIp	106	1.2	1.6	1.7	**1.5**	2.6	2.6	2.7	**2.6**	1.3	1.3	1.0	**1.2**
IIIp	154	2.0	1.8	1.7	**1.8**	3.0	2.7	2.7	**2.8**	1.0	0.9	1.0	**1.0**
IVp	193	2.5	3.0	2.1	**2.5**	3.6	4.0	3.2	**3.6**	0.8	1.2	0.4	**0.8**
Vp	247	2.6	2.4	3.6	**2.7**	3.1	3.2	4.0	**3.4**	0.9	1.0	0.7	**0.9**

Table 3. Summary of number of cycles to failure for all stress levels and for both complete and partial transformation cycles.

Test conditions	Stress level (MPa)	Cycles to failure			
		Test 1	Test 2	Test 3	**Avg.**
Ic	54	12154	8322	4991	**8489**
IIc	106	7078	3426	6800	**5768**
IIIc	154	1836	2199	2359	**2131**
IVc	193	2764	2369	2998	**2710**
Vc	247	1224	1325	2013	**1521**
Ip	54	38529	41406	53478	**44471**
IIp	106	23831	24782	29289	**25967**
IIIp	154	29031	34199	33218	**32149**
IVp	193	19732	17512	15075	**17440**
Vp	247	18564	15502	19634	**17900**

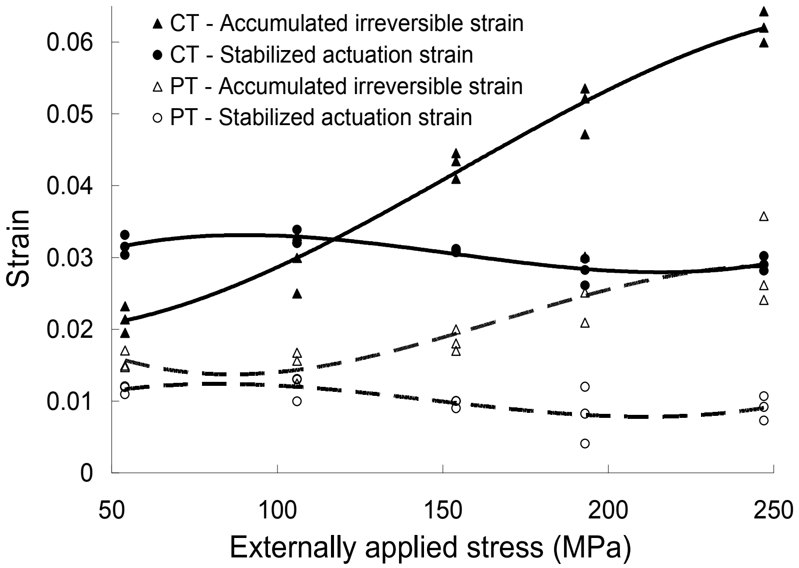

Figure 14. Accumulated plastic strain and stabilized actuation strain at failure as a function of the applied stress level for complete transformation (CT) and partial transformation (PT).

2.2.2. Influence of partial transformation

In terms of actuation performances and fatigue life, Figure 14 and Figure 15 characterize the significant influence of partial versus complete transformation cycles. By reducing the full amount of actuation strain (~ 3% in complete transformation) by nearly half (~ 1% to ~ 1.5% in partial transformation), the strain in martensite reaches averaged values ranging from 2.7% to 3.4% while the accumulated plastic strain at failure is averaging values from 1.5% to 2.7%. Figure 15 presents results for the number of cycles to failure as a function of the level of applied stress, for both complete and partial transformation cycles and the main conclusion is an increase of the fatigue life of the SMA actuators by nearly one order of magnitude when partial transformation cycles are generated.

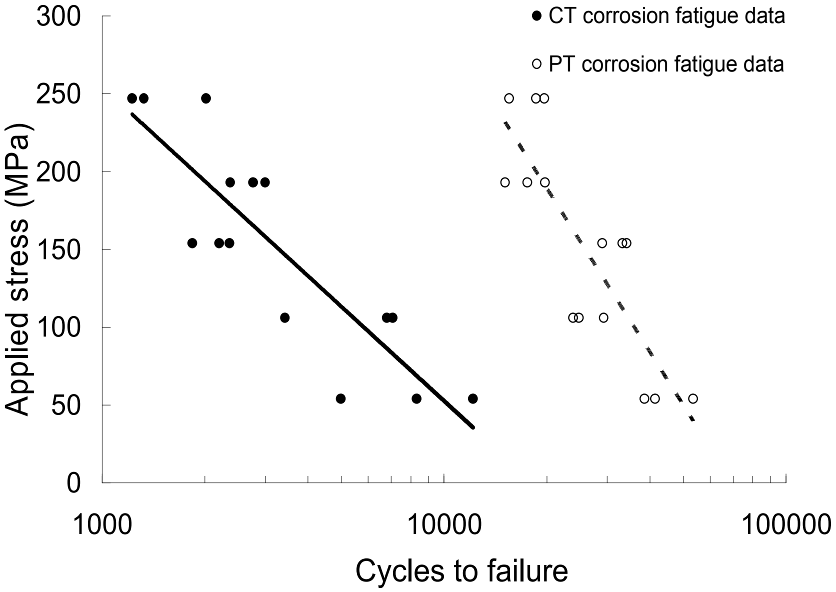

Figure 15. Applied stress level with respect to the number of cycles to failure for complete transformation (CT) and partial transformation (PT).

The plastic strain accumulation is often considered to be the appropriate failure criterion in the case of low-cycle fatigue response of conventional metals [35]. As previously observed in Figure 12 and Figure 13, the actuation strain, due to its stable response, cannot be used to define a failure criterion. However, the accumulated plastic strain exhibits a significant dependency on the number of cycles to failure and can be expressed through a Manson-Coffin criterion [22, 26], as shown in Eq. (13).

$$\varepsilon^{p} = \alpha\left(N_{f}\right)^{-\beta} \tag{13}$$

It was found that for most metals the slope of the Manson-Coffin law can be approximated to 0.5 [35], and SMAs seem to follow a similar trend with values comprised between 0.46 and 0.54 [22, 23, 26]. The fatigue ductility coefficient α, however, seems to be related to the processing of the alloy. In previous works, it was shown that heat treatments had a great influence on the value of the fatigue ductility coefficient. Figure 16 shows the accumulated plastic strain at failure for both complete and partial transformation cycles. A smaller fraction of actuation strain results not only in an improved fatigue life but also in a lower amount of irrecoverable strain. The lower irrecoverable strain level is a result of a lower rate of damage accumulation through thermomechanical cycling and leads to an extended life of the SMA actuators. The Manson-Coffin approximation, using a fixed β coefficient equal to 0.5, gives less conservative approximations. However, it still captures the effect of various amounts of transformation strain on the lifespan, as well as on the amount or accumulated plastic strain.

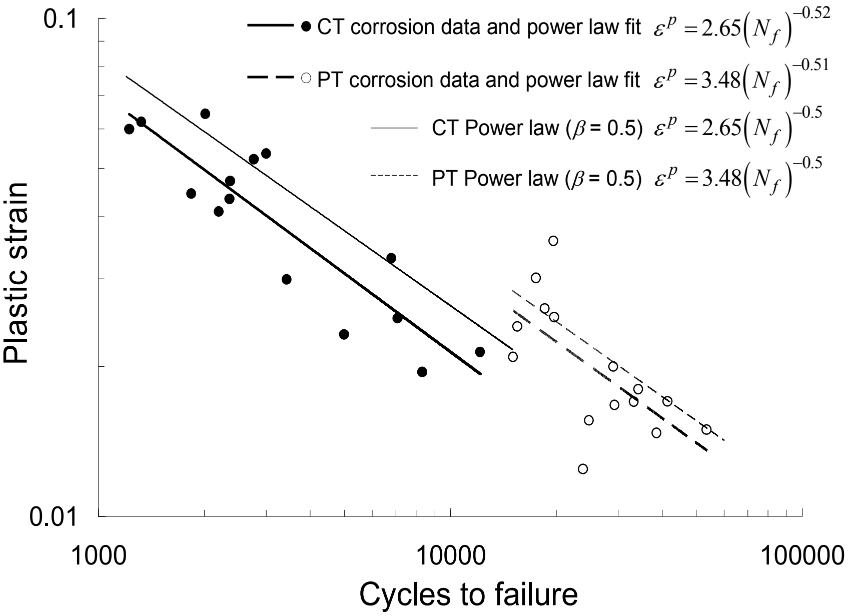

Figure 16. Accumulated plastic strain at failure for complete and partial transformation conditions. Comparison between experimental curves and curve fit for Manson-Coffin coefficient $\beta = 0.5$.

2.2.3. Comparison with corrosion-free fatigue results

Corrosion-free testing conditions were introduced in the subsection 2.1 and results from preliminary investigations [22, 40] are now introduced and compared to the present study involving a corrosive cooling environment. Figure 17 presents the number of cycles to failure versus the level of applied stress for TiNiCu SMA wire actuators subject to corrosion-free and corrosive cooling environments. For both complete and partial transformation cycles, the corrosive environment leads to a significant reduction of the fatigue life of the actuators. Furthermore, it is observed that, at each applied stress level, the difference in number of cycles between corrosion and corrosion-free fatigue life is larger for partial transformation than for complete transformation. This difference indicates that there is a relationship between number of cycles and corrosion. The second significant observation is the influence of corrosion on the scattering of the fatigue data. In the case of transformation induced fatigue under corrosion, the curve fitting of the corrosion fatigue data has a correlation coefficient equal to approximately 0.7 for both complete and partial transformations. Those values are indicative of data dispersion about the averaged values represented by the curve fitted shown in Figure 17. The correlation coefficient for corrosion-free fatigue data is approximately equal to 0.9, for both complete and partial transformation cycles. This result indicates that localized damage mechanisms affect the overall macroscopic fatigue response and the behavior of the SMA actuators.

In Figure 18, the Manson-Coffin law is applied to corrosion-free and corrosion fatigue results for complete transformation cycles only to estimate the validity and limitations of the Manson-Coffin criterion. The fatigue ductility coefficient α changes from 2.58 in corrosion-free conditions to 2.65 in a corrosive environment, which indicates that corrosion has little influence on the accumulation of plastic strains under complete transformation. Moreover, one can observe from Figure 17 that by setting the value of the slope β at 0.5, the corrosion and corrosion-free equations are similar. Therefore, the Manson-Coffin criterion does not allow a good estimation of the influence of corrosion on the fatigue life. The Manson-Coffin failure criterion has previously been investigated for similar alloy composition and proved how the accumulated transformation induced plastic strain can be utilized to model failure of SMA actuators using a fixed value of 0.5 for the slope β [18, 22, 40]. However, for different environments, the failure criterion does not capture the different fatigue limits under similar assumptions.

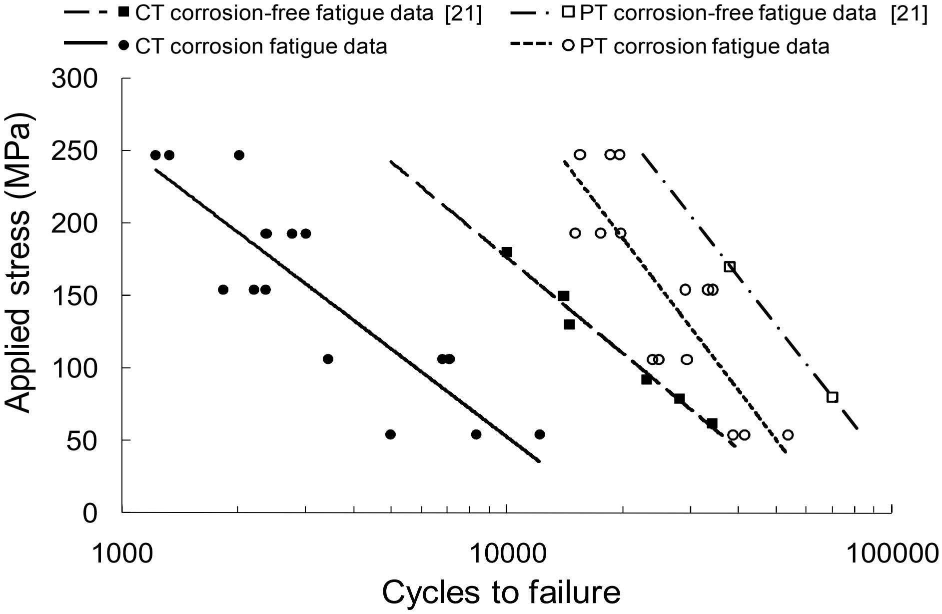

Figure 17. Influence of corrosion on the stress-life response of SMA actuators for complete and partial transformation cycles.

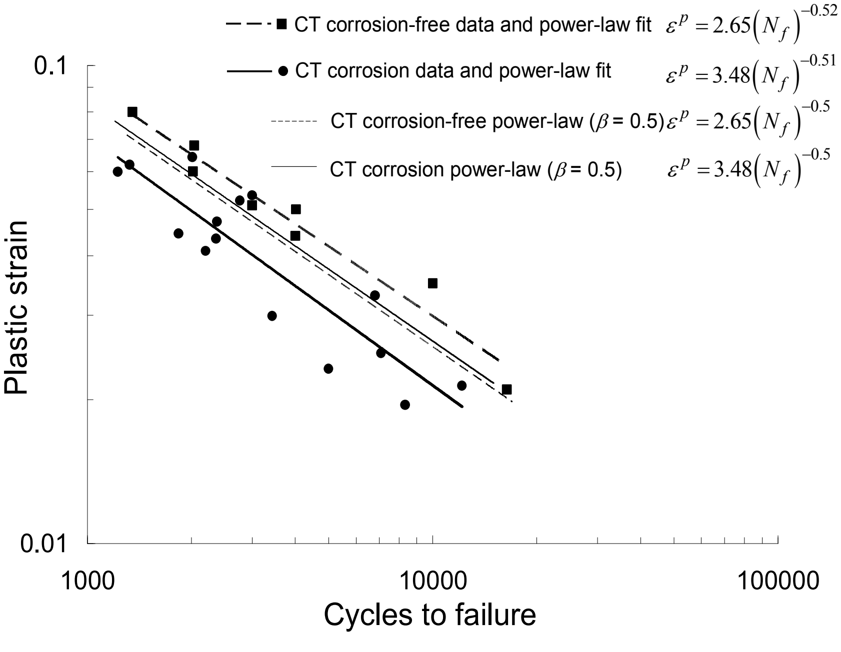

Figure 18. Influence of corrosion on the plastic strain accumulation response of SMA actuators for complete transformation cycles. Comparison between experimental curves and curve fit for Manson-Coffin coefficient $\beta = 0.5$.

CHAPTER III

CHARACTERIZATION AND MODELING OF THE TRANSFORMATION INDUCED FATIGUE OF TiNiCu SMA ACTUATORS

In Chapter II, constant stress fatigue testing was performed in corrosive environment and compared to corrosion-free fatigue results [26]. Figure 19 presents a summary of the experimental fatigue results obtained in Chapter II and characterizes the influence of corrosion on the fatigue life of TiNiCu SMA wire actuators. It was found that the application of an external voltage to induce resistive heating of the SMA actuators was responsible for the reduction of fatigue life, for both complete and partial transformation cycles. The experimental conditions of the experiments under corrosive conditions are recalled in Table 1.

The main results were the observation of the reduction of fatigue life of TiNiCu SMA wire actuators in a corrosive environment. The experimental conditions involved complete and partial transformation cycles. It was found that both type of transformation cycles demonstrated sensitivity to the corrosive environment and led to nearly one order of magnitude reduction of the fatigue life of the actuators compared to similar experimental conditions performed in a corrosion-free environment. This analysis was performed based on the relationship between applied stress and number of cycles to failure as well as accumulated plastic strain and number of cycles to failure.

Chapter III first presents a microstructure analysis of the post failure TiNiCu SMA wire actuators. The results from observations and measurements are discussed and used for a micromechanical stress analysis using a modified shear lag model using actuation and accumulated plastic strains. Finally, Chapter III presents simplified damage mechanism in order to formulate a damage accumulation renormalization procedure that is combined with the Miner's rule. The purpose is to formulate a fatigue life model able to reproduce fatigue life results under corrosive conditions from corrosion and corrosion-free fatigue data as well as to predict fatigue life in corrosion-free conditions from corrosion fatigue test data.

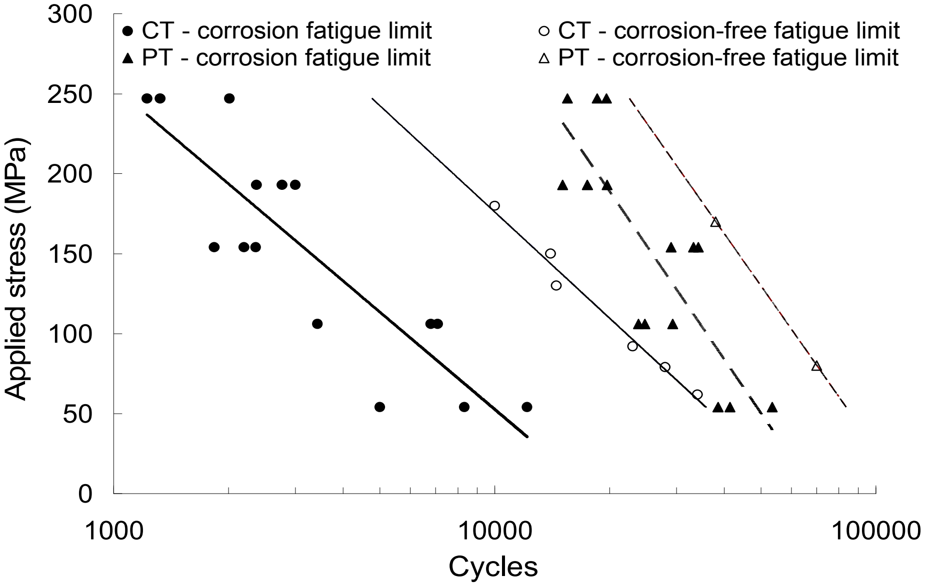

Figure 19. Applied stress vs. number of cycles to failure. Fatigue data in complete transformation under (a) corrosion-free conditions and (b) corrosive conditions. Fatigue data in partial transformation under (c) corrosion-free conditions and fatigue data in partial transformation under (d) corrosive conditions.

3.1. Microstructure Analysis

The purpose of Chapter III is to explain the reasons for the development of corrosion during transformation cycles and its influence on the reduction of the fatigue life of TiNiCu SMA wire actuators. The use of microstructural evaluation, chemical analysis and micromechanics is proposed to investigate the effect of a corrosive environment on the microstructure and on the reduction of the number of cycles to failure of TiNiCu SMA wire actuators under thermally induced constant stress cyclic loading.

3.1.1. Fractography

The investigations were conducted using a *JEOL JSM 5800 LV* scanning electron microscope (SEM) and the measurements presented in the next subsection were performed using a *LEICA MEF4M* metallographic optical microscope

Figure 20 show fracture surfaces for test specimens tested in complete and partial transformation at 106 MPa. Figure 20(a) and Figure 20(b) show crack initiation areas exhibiting smooth morphology and located at the surface of the specimens while final stage failure is identifiable near and at the tear lines. Figure 20(c) and Figure 20(d) are two examples of stress levels resulting in severe damage leading to crack formation across the entire specimens. Figure 20(c) is the fractography of a specimen tested under complete transformation conditions at 247 MPa presenting a circular crack located approximately 50 μm under the surface of the specimen. Under partial transformation cycles and at 193 MPa, Figure 20(d) exhibits a level of damage higher than under complete transformation. This observation is not only supported by the presence of circular cracks but also by the formation of cracks through the entire specimen. However, the fatigue crack initiation sites are similar in all cases. Fatigue cracks show initiation from the surface extended to a large portion of the circumference of the specimen.

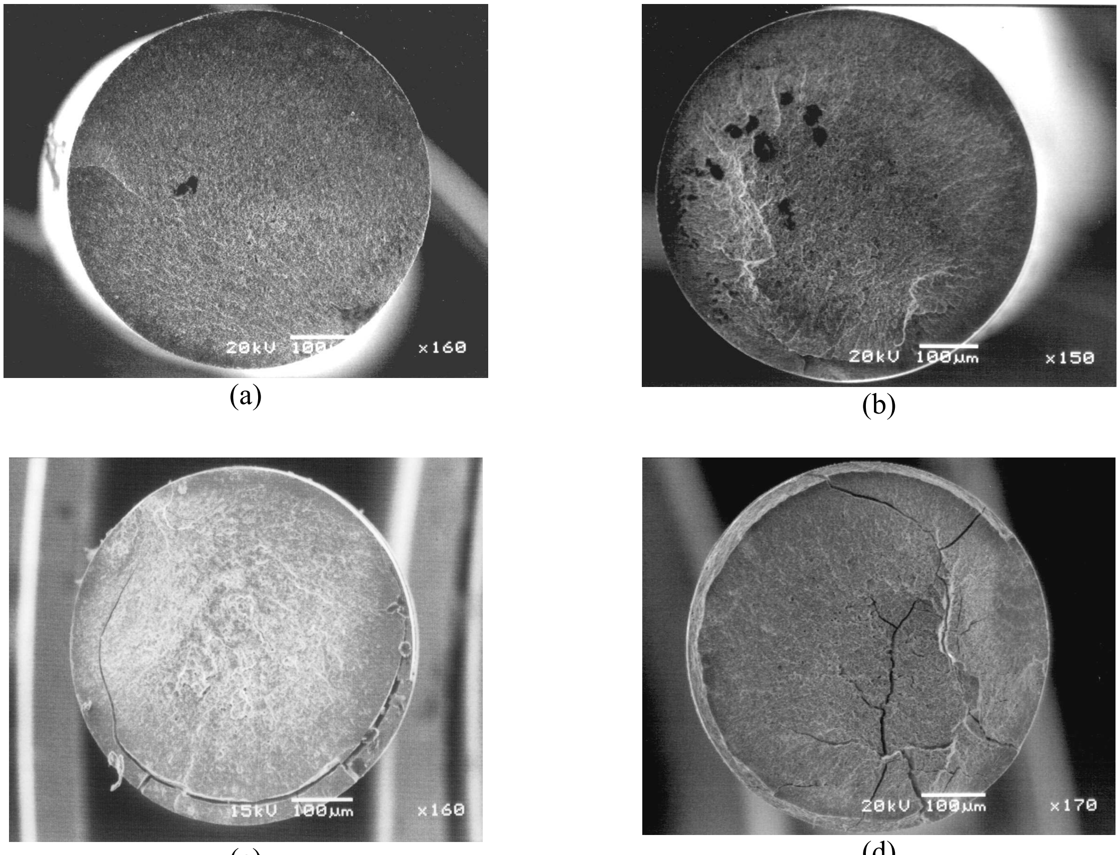

(a) (b) (c) (d)

Figure 20. Fracture surfaces for samples tested under test conditions (a) IIc (106 MPa, complete transformation), (b) IIp (106 MPa, partial transformation), (c) Vc (247 MPa, complete transformation) and (d) IVp (193 MPa, partial transformation).

Figure 21(a) and Figure 21(b) corroborate this observation with the assessment of a microcrack network covering the entire surface of the SMA actuators. The length of the microcracks covering the surface of the actuator is comprised between 5 μm and 10 μm and the microcracks are circumferentially oriented.

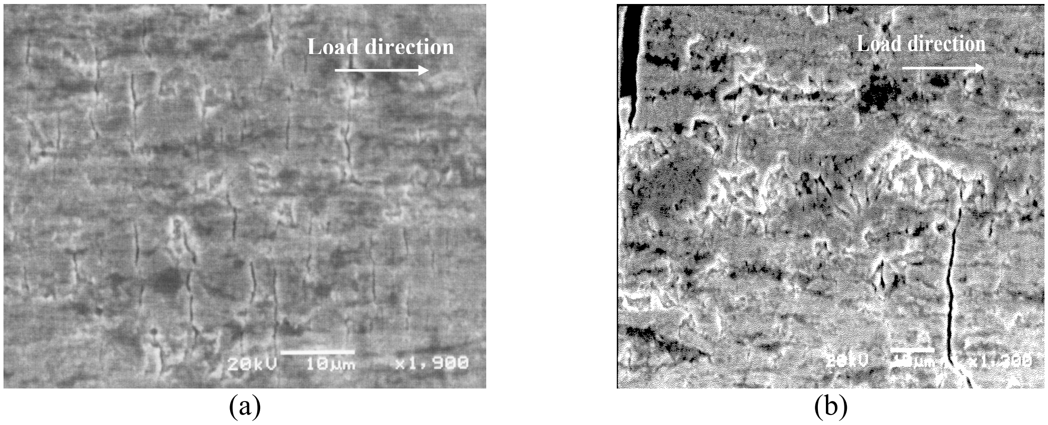

(a) (b)

Figure 21. Superficial microcrack patterns for (a) test condition IIIc (154 MPa, complete transformation) and (b) test condition IVp (193 MPa, partial transformation).

The superficial microcracks were found in all tested specimens, for both complete and partial transformation cycles. For applied stresses ranging from 154 MPa to 247 MPa and from 106 MPa to 247 MPa for complete and partial transformation cycles, respectively, the microcracks coalesced and formed circumferential macrocracks as shown in Figure 22. Figure 22(a) shows one end of a failed specimen with circumferential cracks visible up to 8 mm. It is found that the circumferential cracks are distributed in a periodic arrangement on both segments of the ruptured specimen [26, 54]. This indicates that the final failure occurred approximately in the middle of the periodically cracked region. Figure 22(b) and Figure 22(c) illustrate that the crack spacing is dependent on the type of transformation. Therefore, the observation of such unique morphology led to additional investigations, such as the measurement of the circumferential crack spacing and depth.

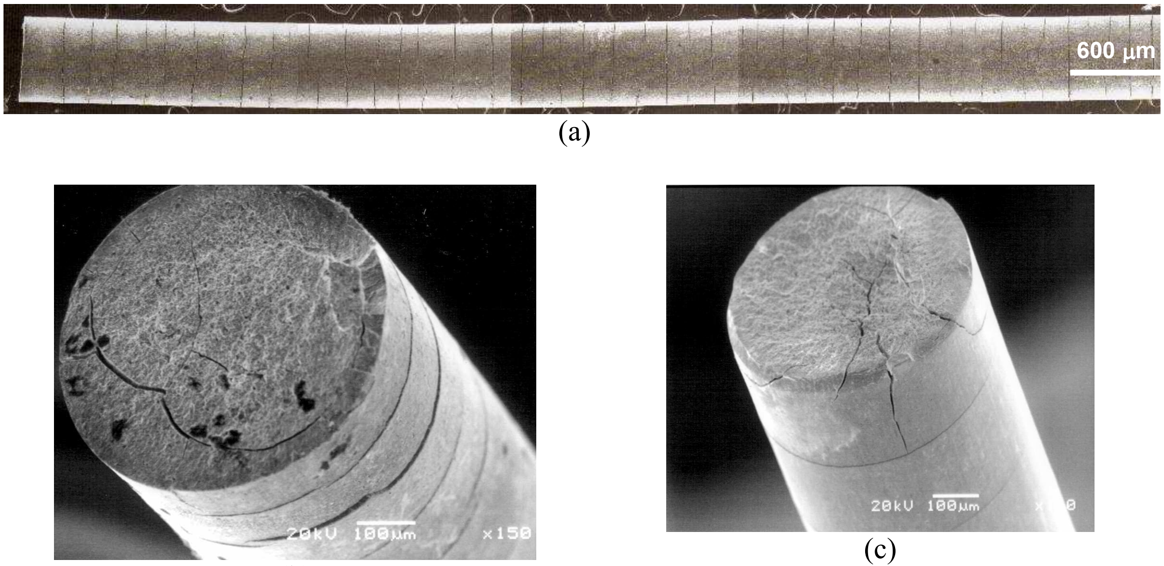

(a)

(b)

(c)

Figure 22. (a) SEM micrograph of a SMA actuator with periodical circumferential cracks (total length = 8 mm, crack spacing ≈ 180 μm). The fracture surface can be seen on the right hand side of the specimen. Sample IVc tested at 193 MPa in complete transformation conditions; comparison of crack spacing near fracture surface for (b) sample IVc and (c) sample Vp.

3.1.2. Circumferential crack measurements

Circumferential cracks were identified for stress levels ranging from 154 MPa to 247 MPa and from 106 MPa to 247 MPa, for complete and partial transformations, respectively; therefore, all reported crack measurements correspond to those specific stress ranges. The crack spacing was measured for the three specimens at each test condition, and each data point reported in Figure 23 corresponds to an average of the crack spacing measurement. The results show that the crack spacing ranges between 140 μm and 200 μm in complete transformation, while in partial transformation, it ranges between 230 μm and 375 μm. In both cases, the crack spacing was reduced with an increase of the applied stress level. This result indicates that the amount of transformation strain dictates the crack spacing at failure.

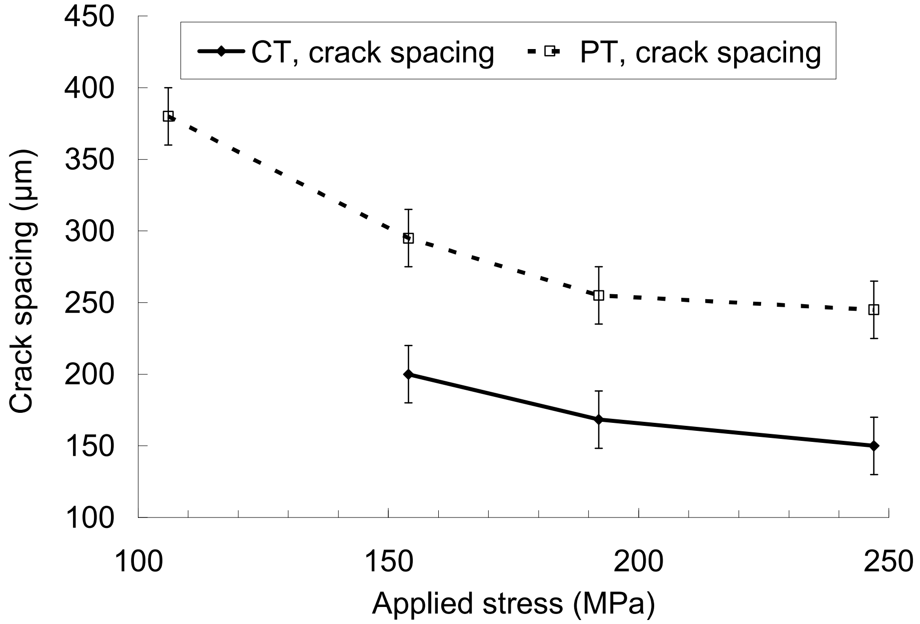

Figure 23. Circumferential crack spacing as a function of the applied stress.

Different crack depths were also observed by looking at two different fracture surfaces from two experimental conditions, as shown in Figure 24(a) and Figure 24(b). Complete and partial transformation cycles performed under an applied stress of 247 MPa, resulted in failure occurring after approximately 1,200 cycles and 15,000 cycles, respectively. The crack depth for complete transformation was measured between 30 μm and 40 μm, while for partial transformation, the crack depth was measured between 60 μm and 70 μm. The presence of circular cracks, distributed in a periodical arrangement showing different spacing and depths under various test conditions, led to the assumption that there is a damage mechanism related to the development of a brittle surface layer. Therefore, the variation of the crack depth measurements in terms of both applied stress level and amount of actuation strain was further investigated. From each specimen, four different radial measurements were performed at the location of the fracture surface, as shown in Figure 25.

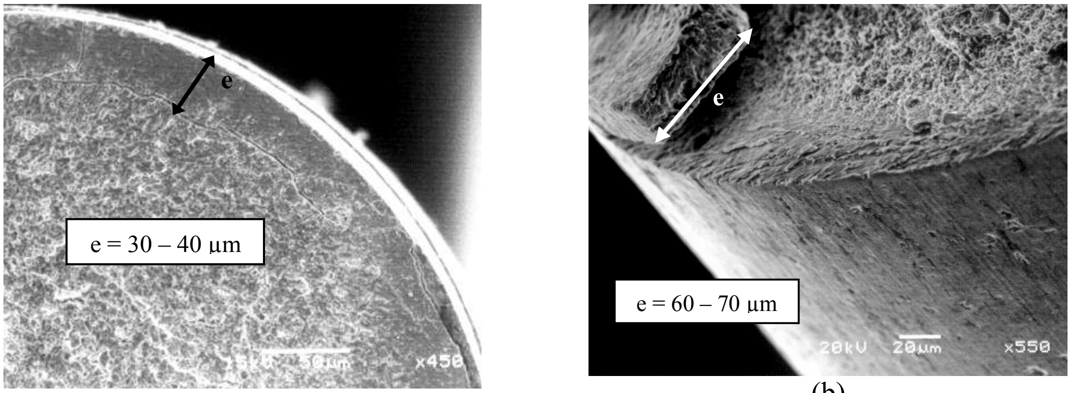

(a) (b)

Figure 24. Fracture surface and circumferential crack formation after (a) ~ 1,200 cycles under test condition Vc (247 MPa, complete transformation) and after (b) ~ 15,000 cycles under test condition Vp (247 MPa, partial transformation).

In addition, four additional measurements away from the fracture surface were conducted to assess the distribution of the crack depth and to identify any localization. The selected locations were 5 mm apart from each other, with the reference point being the fracture surface. Each test condition is represented by three specimens; therefore each data reported in Figure 26 corresponds to a crack depth measurement averaged over 12 measurements.

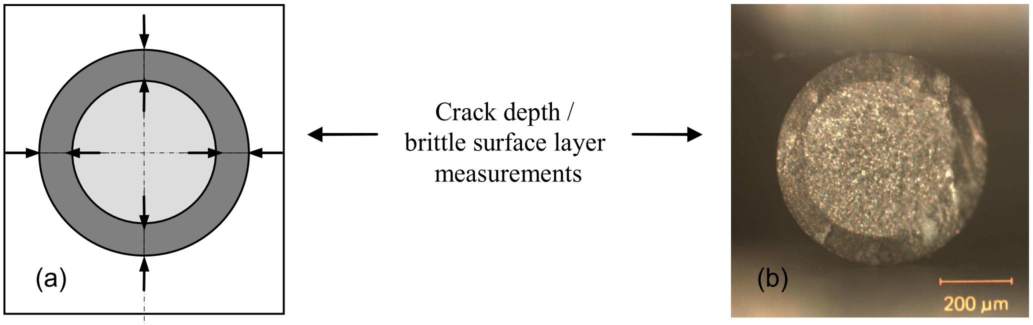

Figure 25. Description of the crack depth four radial measurements: (a) schematic of a cross section and its four measurements, (b) example of actual optical micrograph used to make the crack depth measurements.

Figure 26(a) and Figure 26(b) represent the crack depth as a function of the axial position on the wire, relative to the fracture surface for each applied stress level, for complete and partial transformation conditions, respectively. Figure 26(b) indicates that a longer fatigue life resulted in deeper circumferential cracks. The crack depth is also found to increase near the fracture surface. The crack depth increase at the final failure location is most likely attributed to damage localization prior to final failure.

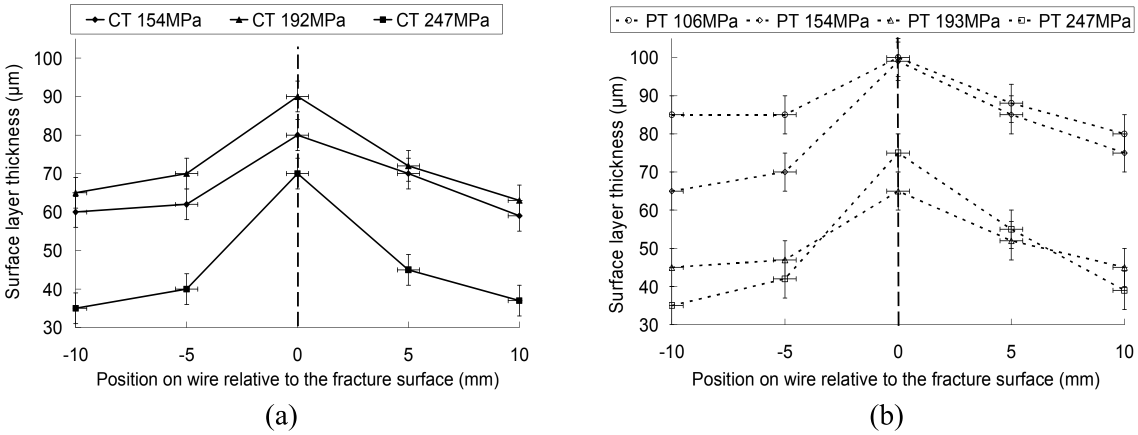

(a) (b)

Figure 26. Brittle layer thickness or crack depth measurement and evolution as a function of the applied stress and of the relative position to the fracture surface, (a) complete transformation, (b) partial transformation.

3.1.3. Proposed cyclic damage mechanism

Under both complete and partial transformation cycles, the actuation strain is in the order of a 1% to 3% and the result is the failure of the protective oxide layer allowing further oxidation of unpassivated metal. It was observed in the previous section that the depth of the circumferential cracks increases with increasing number of cycles to failure. Therefore this phenomenon is related to a slow and accumulating process where corrosion builds up as the thermomechanical cycles progress.

Figure 27 and Figure 28 are schematic representations of how cyclic phase transformation and corrosion are working concurrently. Figure 27 corresponds to the SMA wire actuator undergoing corrosion upon cooling. The principle is phase transformation, generation of inelastic recoverable actuation strain, failure of the protective oxide layer and exposure of unpassivated SMA to the corrosive environment, as martensite formation creates upheavals at the surface of the material [33]. Figure 28 describes how reverse phase transformation is contributing to the insertion of oxides into the material. It is expected that from the corrosion process, oxides form and contaminate the surface of the metal. This mechanism repeated over an extended number of cycles is assumed to the formation of a mixed SMA/oxide region. This region presents evidence of damage accumulation due to simultaneous transformation cycles and corrosion.

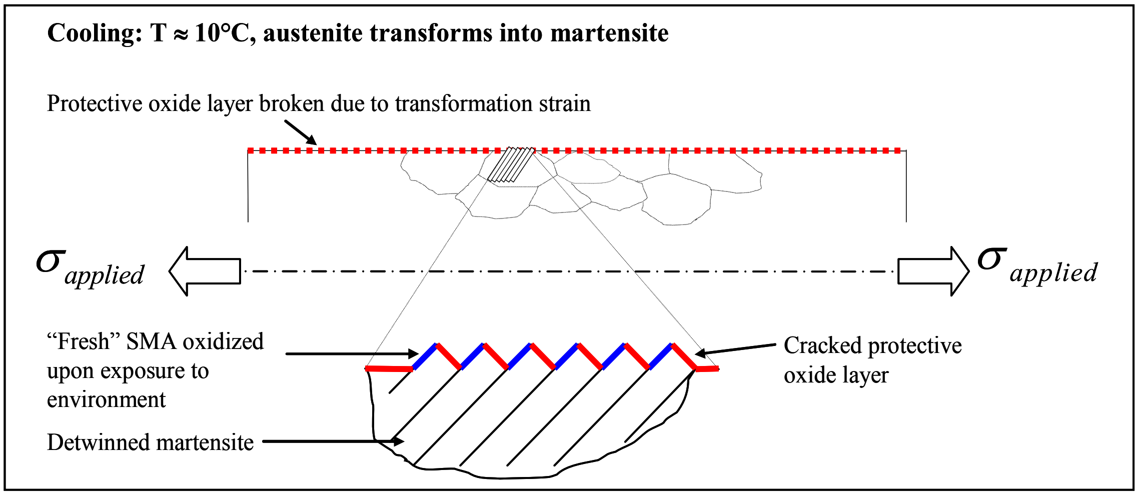

Figure 27. Proposed cyclic corrosion mechanism: SMA actuator was cooled and transformed from austenite to martensite. The large transformation strain was responsible for the failure of the protective oxide layer, exposing oxide free SMA material to the corrosive environment.

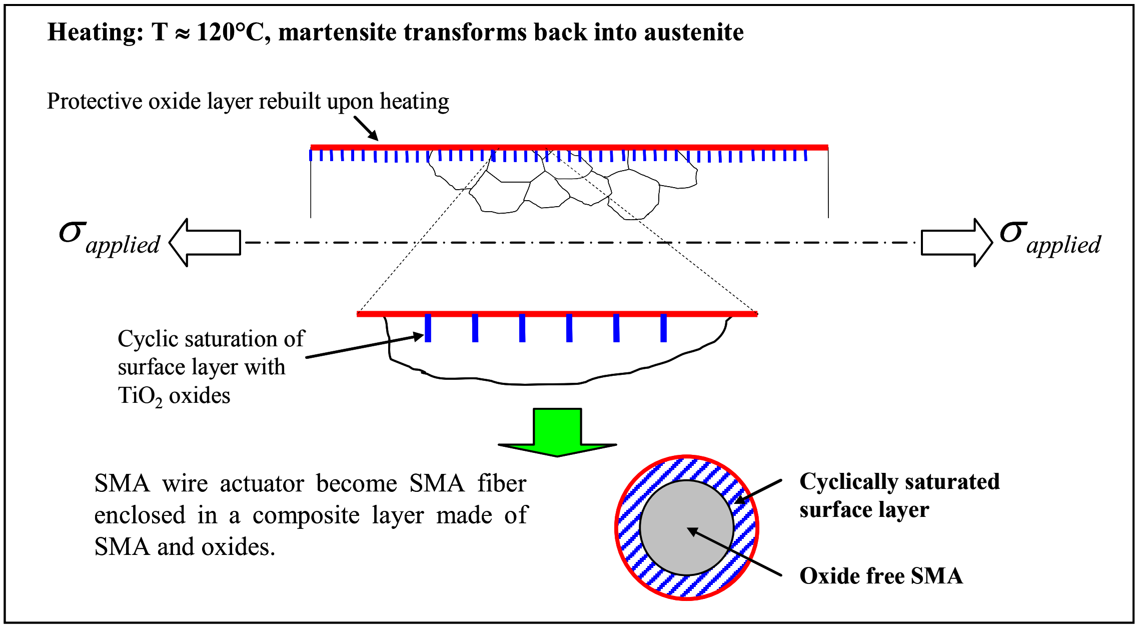

Figure 28. Proposed cyclic corrosion mechanism: SMA actuator transforms back into austenite trapping oxides in a cyclically saturated surface layer.

3.2. Analysis of SMA wire actuator with circular microcracks

3.2.1. Boundary value problem

The shear-lag model is applied to investigate the stress field generated in the surface layer due to stress transfer occurring between the SMA core and the surface layer that contains circumferential cracks. The mechanism of crack formation is assumed here to initiate with a few random cracks and after a certain amount of cycles and periodicity is expected to arise from the development of large axial stresses in the surface layer. The geometry of the surface layer suggests that the maximum stress is attained at the center of the surface layer, between two consecutive cracks. the saturation of the surface layer is then associated to a failure threshold in the surface layer where no additional cracks can be formed, hence leading the SMA core to ultimately bear the entire external load, resulting in final failure of the SMA wire actuator.

Figure 29 is a schematic representing a section of an SMA wire with a periodic distribution of circumferential cracks. Introduced in the previous section and represented in Figure 29, the circumferential cracks exhibit both irregular and periodic distributions. In the periodic distribution region of the SMA actuators, a representative volume element (RVE) is taken between two consecutive circumferential cracks, as shown in Figure 29. The presence of a brittle surface layer containing circumferential cracks is such that the SMA wire can be modeled as a composite cylinder made of an SMA core and a surface layer (SL), perfectly bonded. Therefore, a shear-lag modeling approach is one of the possible options to investigate the present stress-transfer problem [55, 56, 57].

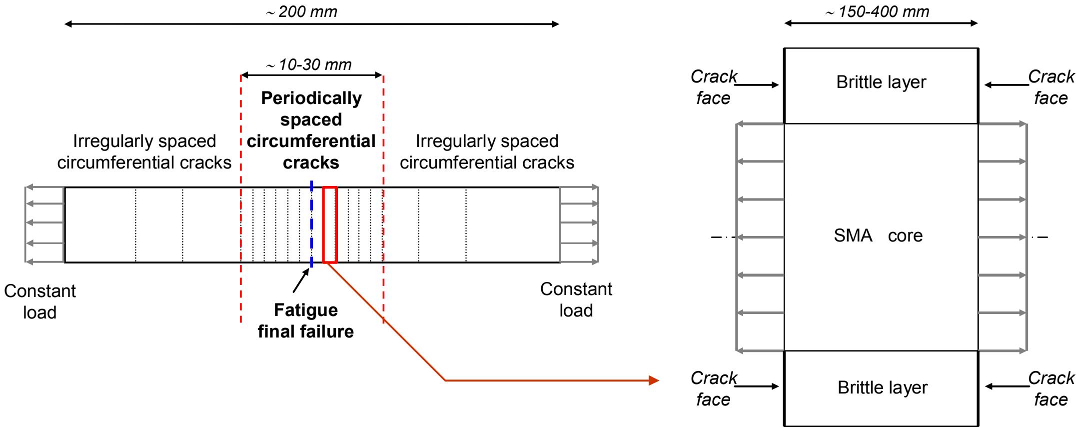

Figure 29. Schematic of the periodical microcraking pattern and selection of a representative volume element.

In order to avoid stress concentrations issues and to reduce the problem to one-dimension along the z-axis, quantities such as stress, strain and displacement are averaged over the respective cylindrical cross sectional areas of the SMA core and of the surface layer. The averaging of an (r,z)-dependent function into a z-dependent one is shown for the SMA core and for the surface layer in Eqs. (14) and (15), respectively.

$$\left\langle f_{zz}^{SMA}\right\rangle(z)=\frac{1}{\pi(R-e)^2}\int_0^{R-e}2\pi r f_{zz}^{SMA}(r,z)\,dr \tag{14}$$

$$\left\langle f_{zz}^{SL}\right\rangle(z)=\frac{1}{\pi\left(R^2-(R-e)^2\right)}\int_{R-e}^{R}2\pi r f_{zz}^{SL}(r,z)\,dr \tag{15}$$

Figure 30 shows a free body diagram of the selected RVE shown in Figure 29, where the composite cylinder is shown in equilibrium with the SMA core connected to the surface layer through an interfacial shear stress $\tau(z)=\sigma_{rz}(r,z)$ at $r=R-e$.

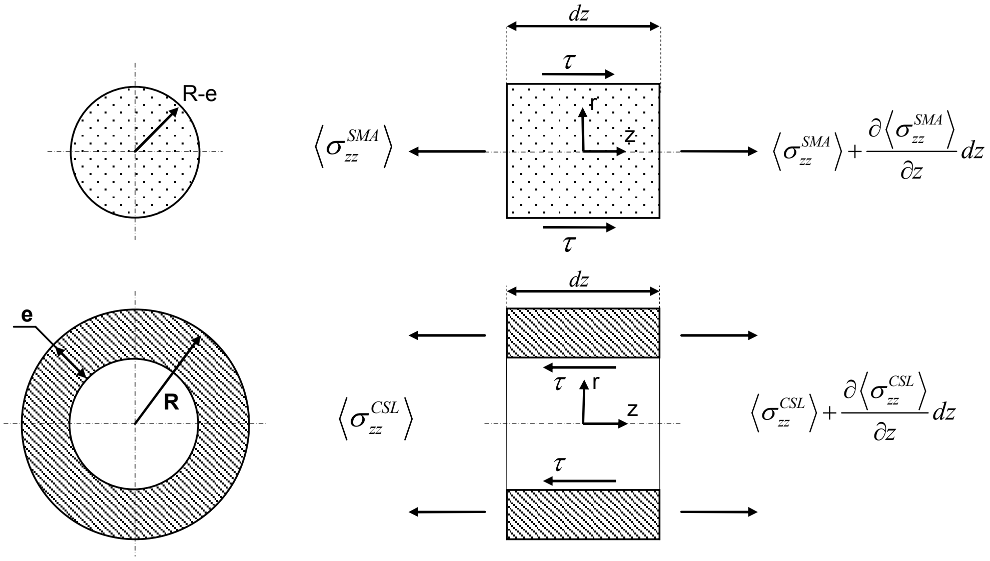

Figure 30. Force equilibrium for SMA core and surface layer (SL) for the selected RVE.

The balance of linear momentum along the z-axis in each body constituting the composite cylinder RVE, combined with the averaging of the axial stresses $\sigma_{zz}^{SMA}\left(r,z\right)$ and $\sigma_{zz}^{SL}\left(r,z\right)$, yields an equilibrium between the averaged axial stresses $\left\langle\sigma_{zz}^{SMA}\right\rangle$ and $\left\langle\sigma_{zz}^{SL}\right\rangle$, and the interfacial shear stress τ . The resulting equilibrium gives the two coupled differential equations shown in Eqs. (16) and (17).

$$\frac{\partial\left\langle\sigma_{zz}^{SMA}\right\rangle}{\partial z}+\frac{2}{R-e}\tau=0 \tag{16}$$

$$\frac{\partial\left\langle\sigma_{zz}^{SL}\right\rangle}{\partial z}-\frac{2c_{SMA}}{\left(R-e\right)c_{SL}}\tau=0 \tag{17}$$

Where c_{SMA} and c_{SL} are the respective surface area fraction of the SMA core and of the surface layer.

Considering the axial stress-strain constitutive equations, the total strain is additively decomposed into an elastic and inelastic strain. As the total strain includes the elastic contribution due to the application the external load, the inelastic strains to consider are the accumulated plastic strain and the actuation strain corrected by the elastic strain contribution, i.e. the transformation strain. The detailed formulation of the transformation strain is described in Chapter II. The macroscopic nature of the strain measurements using LVDTs leads to averaged strain values over the cross section. Due to corrosion and formation of the brittle surface layer, we assume that the transformation strain is inhibited in the surface layer and only formation of plastic strain remains whereas in the SMA core, transformation strain and accumulated transformation induced plastic strain coexist. Therefore, they are denoted by $\left\langle \varepsilon_{zz\_in}^{SMA} \right\rangle$ and $\left\langle \varepsilon_{zz\_in}^{SL} \right\rangle$, for the SMA core and for the surface layer, respectively and the constitutive relations for the SMA core and the surface layer are given in Eqs. (18) and (19).

$$\left\langle \varepsilon_{zz}^{SMA} \right\rangle = \frac{\left\langle \sigma_{zz}^{SMA} \right\rangle}{E^{SMA}} + \left\langle \varepsilon_{zz\_in}^{SMA} \right\rangle \tag{18}$$

$$\left\langle \varepsilon_{zz}^{SL} \right\rangle = \frac{\left\langle \sigma_{zz}^{SL} \right\rangle}{E^{SL}} + \left\langle \varepsilon_{zz\_in}^{SL} \right\rangle \tag{19}$$

Where $\left\langle \varepsilon_{zz\_in}^{SMA} \right\rangle$ and $\left\langle \varepsilon_{zz\_in}^{SL} \right\rangle$ are expressed in terms of the transformation and plastic strain recorded during the fatigue experiments described in Chapter II, as shown in Eqs. (20) and (21).

$$\left\langle \varepsilon_{zz\_in}^{SMA} \right\rangle = \varepsilon_k^t + \varepsilon_k^p \tag{20}$$

$$\left\langle \varepsilon_{zz\_in}^{SL} \right\rangle = \varepsilon_k^p \tag{21}$$

The total strain in the SMA core and in the surface layer can be expressed in terms of the displacement, as shown in Eqs. (22) and (23), respectively.

$$\varepsilon_{zz}^{SMA} = \frac{\partial u_z^{SMA}}{\partial z} \tag{22}$$

$$\varepsilon_{zz}^{SL} = \frac{\partial u_z^{SL}}{\partial z} \tag{23}$$

There is an equation in the shear-lag model that linearly relates the interfacial shear stress τ to the averaged displacement mismatch between the SMA core and the surface layer, i.e. $\left\langle u_z^{SMA} \right\rangle$ and $\left\langle u_z^{SL} \right\rangle$, respectively, as shown in Eq. (24).

$$\tau(z) = \Gamma\left(\left\langle u_z^{SL}\right\rangle(z) - \left\langle u_z^{SMA}\right\rangle(z)\right) \tag{24}$$

The constant Γ is proportional to an equivalent interfacial shear modulus and is a parameter for which several studies have been conducted. Its formulation is found identical to other works [55, 56, 57,] and is given by:

$$\Gamma = \frac{c_{SL}}{(R-e)\left(\frac{c_{SL}}{4\mu^{SMA}} + \frac{1}{2\mu^{SL}}\left(\frac{1}{c_{SL}}\ln\frac{1}{c_{SMA}} - 1 - \frac{c_{SL}}{2}\right)\right)} \tag{25}$$

It can be shown that by Averaging Eqs. (22) and (23), and combining them with Eqs. (16), (17), (18), (19) and (24) the interfacial shear stress τ satisfies the following second order ordinary differential equation, as shown in Eq. (26).

$$\frac{d^2\tau(z)}{dz^2} = k^2\tau(z) \tag{26}$$

With:

$$k^2 = \frac{2E^*}{(R-e)^2\,\eta E^{SMA}E^{SL}} \tag{27}$$

$$E^* = c_{SMA}E^{SMA} + c_{SL}E^{SL} \tag{28}$$

$$\eta = \frac{c_{SL}}{4\mu^{SMA}} + \frac{1}{2\mu^{SL}}\left(\frac{1}{c_{SL}}\ln\frac{1}{c_{SMA}} - 1 - \frac{c_{SL}}{2}\right) \tag{29}$$

Solving Eq. (26) and using Eqs. (16) and (17), the stress in the SMA core and surface layer are fully determined and shown in Eqs. (30) and (31):

$$\left\langle \sigma_{zz}^{SMA}\right\rangle(z) = -\frac{2}{k(R-e)}\left(-A_0e^{-kz} + B_0e^{kz}\right) + D_0 \tag{30}$$

$$\left\langle \sigma_{zz}^{SL} \right\rangle (z) = \frac{2}{k\left(R-e\right)} \frac{c_{SMA}}{c_{SL}} \left(-A_0 e^{-kz} + B_0 e^{kz}\right) + D_1 \tag{31}$$

Integration of Eqs. (30) and (31) leads to the expressions for the average axial displacements in the SMA core and in the SL, and are shown in Eqs. (32) and (33), respectively:

$$\left\langle u_z^{SMA} \right\rangle (z) = -\frac{2}{k^2\left(R-e\right)E^{SMA}} \left(A_0 e^{-kz} + B_0 e^{kz}\right) + \frac{D_0}{E^{SMA}} z + F_0 \tag{32}$$

$$\left\langle u_z^{SL} \right\rangle (z) = \frac{2}{k^2\left(R-e\right)E^{SL}} \frac{c_{SMA}}{c_{SL}} \left(A_0 e^{-kz} + B_0 e^{kz}\right) + \frac{D_1}{E^{SL}} z + F_1 \tag{33}$$

Where A_0, B_0, D_0, D_1, F_0 and F_1 are six constants determined from the boundary and symmetry conditions. These conditions are summarized in Eqs. (34) - (38).

$$\left\langle \sigma_{zz}^{SMA} \right\rangle (z = \pm\delta/2) - E^{SMA} \left\langle \varepsilon_{zz\_in}^{SMA} \right\rangle = \frac{\sigma_{applied}}{c_{SMA}} \tag{34}$$

$$\left\langle \sigma_{zz}^{SL} \right\rangle (z = \pm\delta/2) - E^{SL} \left\langle \varepsilon_{zz\_in}^{SL} \right\rangle = 0 \tag{35}$$

$$\tau(z = \pm\delta/2) = \Gamma\left(\left\langle u_z^{SL} \right\rangle (z = \pm\delta/2) - \left\langle u_z^{SMA} \right\rangle (z = \pm\delta/2)\right) \tag{36}$$

$$\tau\left(z=0\right)=0 \tag{37}$$

$$\left\langle u_z^{i} \right\rangle (z=0) = 0 \tag{38}$$

3.2.2. Parameters identification

In order to investigate the saturation of the surface layer with circumferential cracks exhibiting different crack spacing and to evaluate the stress developed in the surface layer, the shear-lag analysis requires the elastic properties of both the SMA core and the surface layer, the dimensions of the RVE and the amount of inelastic strain measured upon fatigue testing.

In this problem, the material is considered isotropic; therefore two material constants are needed, i.e. Young's modulus and axial shear modulus for both the SMA core and the surface layer, E^{SMA}, μ^{SMA} and E^{SL}, μ^{SL}, respectively. The elastic properties of the SMA core correspond to the elastic properties of the austenite or of the martensite [58], depending on the thermal loading condition. However, the elastic properties of the surface layer are more complex to estimate due to corrosion and cracks. The modifications of the elastic properties in the surface layer are solely attributed to the cyclic damage mechanism, i.e. to the insertion of oxides in the surface of the SMA wire actuator. The measurement of the thickness of the surface layer ranges from approximately 50 μm to approximately 100 μm, making impossible for a pure oxide layer to reach under the present test conditions [28]. Oxidation studies performed on NiTi shape memory alloys showed TiO_2 oxide layer thicknesses ranging between 1 μm and 2 μm under severe oxidizing conditions [59]. Therefore, under cyclic transformation, we assume that a similar formation is expected.

Table 4. Material parameters for SMA core [58], $TiO2$ oxides [60, 61, 62] and for the surface layer in complete and partial transformation conditions.

	SMA core	TiO_2 pure phase	Surface layer Complete transformation	Surface layer Partial transformation
Volume fraction of TiO_2 in surface layer	-	-	$c_{TiO_2} = 1\%$	$c_{TiO_2} = 2\%$
Young's modulus (GPa) at high temperature	67.9	230.0	68.7	69.4
Young's modulus (GPa) at low temperature	16.0	230.0	16.3	16.6
Shear modulus (GPa) at high temperature	26.0	90.0	26.4	26.7
Shear modulus (GPa) at low temperature	6.2	90.0	6.3	6.4

Table 5. Inelastic strain values for SMA core and SL. The values are obtained for fatigue tests performed under 154 MPa applied stress.

		SMA core $\left\langle \varepsilon_{zz\_in}^{SMA} \right\rangle$		Surface Layer (SL) $\left\langle \varepsilon_{zz\_in}^{SL} \right\rangle$
Test condition	Stress level (MPa)	Plastic strain $\varepsilon_k^p; k = N_f$	Transformation strain $\varepsilon_k^t; k = N_f$	Plastic strain $\varepsilon_k^p; k = N_f$
Ic	54	2.1%	2.9%	2.1%
IIc	106	2.9%	2.8%	2.9%
IIIc	154	4%	2.4%	4%
IVc	193	5.1%	1.9%	5.1%
Vc	247	6.2%	1.7%	6.2%
Ip	54	1.6%	1%	1.6%
IIp	106	1.5%	1%	1.5%
IIIp	154	1.8%	0.6%	1.8%
IVp	193	2.4%	0.4%	2.4%
Vp	247	2.9%	0.3%	2.9%

According to the damage mechanism introduced in the previous section, we can form the ratio between the oxide formation and the brittle surface layer formation, yielding volume fractions of oxides in the surface layer of nearly 1% and 2%, for complete and partial transformation, respectively. Considering the proposed damage mechanism and the cyclic formation and insertion of oxides in the surface of the SMA wire actuator, a Mori-Tanaka homogenization technique is chosen. The low volume fraction of high elastic properties oxide particles, i.e. E_{ox} ~ 230 GPa, in a softer SMA matrix, i.e. E_{SMA} ~ 16 GPa in martensite and E_{SMA} ~ 67.9 GPa in austenite, make this choice the best suited for this problem. The elastic properties of the SMA core, of the pure TiO_2 phase and of the effective surface layer are summarized in Table 4 [60, 61, 62]. The amounts of inelastic strain in the SMA core $\left\langle \varepsilon_{zz\_in}^{SMA} \right\rangle$ and in the surface layer $\left\langle \varepsilon_{zz\_in}^{SL} \right\rangle$ are directly taken from the experimental results [28] and are reported in Table 5.

The dimensions of the RVE are given by the SMA wire external radius R, the surface layer thickness ϵ and the crack spacing δ. The external radius R is a given constant while the experiments demonstrated that the thickness ϵ and the spacing δ are evolving with the number of cycles and type of transformation, i.e. complete or partial transformation. The analysis focuses on the saturation of the surface layer, where no additional cracks are formed. Therefore, values for the thickness and spacing are taken at final failure of the actuators and are referred to as critical thickness e_{crit} and critical crack spacing δ_{crit}; the values can be found in Table 6.

Table 6. Summary of experimental measurements of crack spacing and crack depth for calculation of failure strength in the surface layer using the Shear Lag Model accounting for inelastic strains.

		Observations / measurements		Shear Lag Model
Test condition	Nominal stress (MPa)	Crack spacing δ_{crit} (mm)	Surface layer thickness (mm)	Maximum stress in SL at δ_{crit} (MPa)
Ic	54	-	-	-
IIc	106	-	-	-
IIIc	154	0.200	0.065	144
IVc	193	0.160	0.060	108
Vc	247	0.140	0.040	130
Ip	54	-	-	-
IIp	106	0.375	0.085	129
IIIp	154	0.300	0.080	116
IVp	193	0.260	0.065	120
Vp	247	0.230	0.055	134

3.2.3. Results and discussion

In this analysis, the input parameters are the material constants, the different amounts of inelastic strain and the geometry of the saturated surface layer, while the output is the axial stress generated in the surface layer.

The state of the SMA is taken in martensite, for which the actuation strain is reaching a maximum, resulting in an inelastic strain mismatch between the SMA core and the surface layer equal to the total amount of the actuation strain. The results are presented for a nominal applied stress equal to 154 MPa with an averaged inelastic strain mismatch equal to 3% and 1.1% for complete and partial transformation cycles, respectively. Following the crack formation mechanism introduced earlier, an idealization of the last four crack formation steps is presented in Figure 31. From this idealized representation, the axial stress in the surface layer $\left\langle \sigma_{zz}^{SL} \right\rangle$ is plotted against the four last half-crack spacings, i.e. $\left(8\delta_{crit}\right)/2$, $\left(4\delta_{crit}\right)/2$, $\left(2\delta_{crit}\right)/2$ and $\delta_{crit}/2$, as shown in Figure 32(a) and Figure 32(b), for complete and partial transformation cycles, respectively.

The results in Figure 32(a) and Figure 32(b) show two different curves for each half-crack spacing: one is corresponding to the solution accounting for the actuation strain due to martensitic transformation and the other one to a solution where the sole elastic response of the SMA core and of the surface layer is considered.

The main result is the observation of the maximum stress in the surface layer attained in the middle of two consecutive cracks with values approximately equal to 400 MPa in complete transformation and 210 MPa in partial transformation. The maximum stress in the partial transformation case is lower than in complete transformation due to a larger thickness of the surface layer, resulting in a larger area to distribute the transferred load from the undamaged SMA core. As the crack spacing reduces when cracks are formed, the length over which shear stress is transferred is getting smaller leading to a lower stress transfer. From the experimental measurements, no additional cracks were formed when the crack spacing reached δ_{crit}, indicating that the axial stress in the surface layer was not high enough to induce further cracking of the surface layer. However, for the penultimate crack spacing $2\delta_{crit}$, the stress level in the surface layer was high enough to induce the last crack formation before saturation. This result indicates that in both cases, complete and partial transformation cycles, the failure strength of the surface layer was attained, thus defining a stress range corresponding to the failure threshold of the surface layer. this result is similar in both complete and partial transformation conditions, with a narrower failure threshold range in the case of partial transformation. The failure threshold range was found to be from approximately 144 MPa to 295 MPa for complete transformation and to be from approximately 116 MPa to 186 MPa for partial transformation. These values are similar to failure strength data recorded for TiO_2 oxide that are in a range of 140 MPa to 160 MPa [61, 63], which indicates a significant influence of the presence of oxide on the behavior of the SMA actuators. Further analyses for the different nominal stresses are reported in a comprehensive summary in Table 6. The analysis of the maximum stress developed in the surface layer at critical crack spacing δ_{crit} for the different loading conditions, i.e. different applied stress level and complete transformation versus partial transformation validates the assumption of a failure threshold below which the surface layer can not long crack. The other observation is that the type of transformation, complete or partial, dictates the crack spacing until saturation.

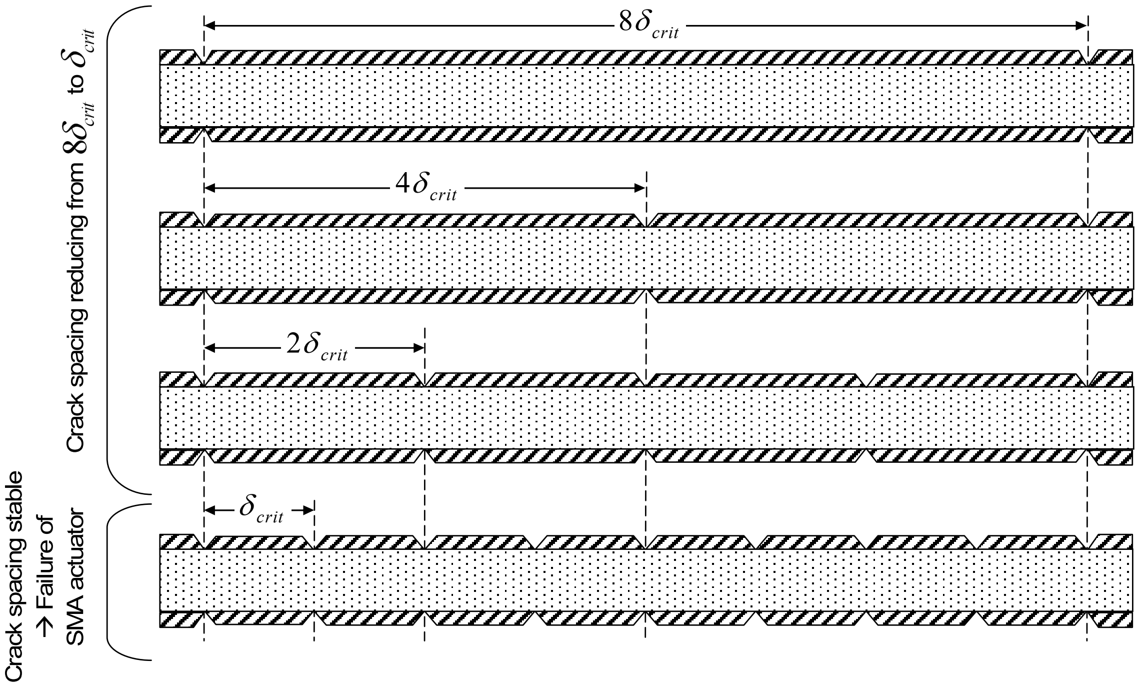

Figure 31. Schematic cross section of an SMA actuator showing circumferential crack formation upon axial stress transfer in the surface layer.

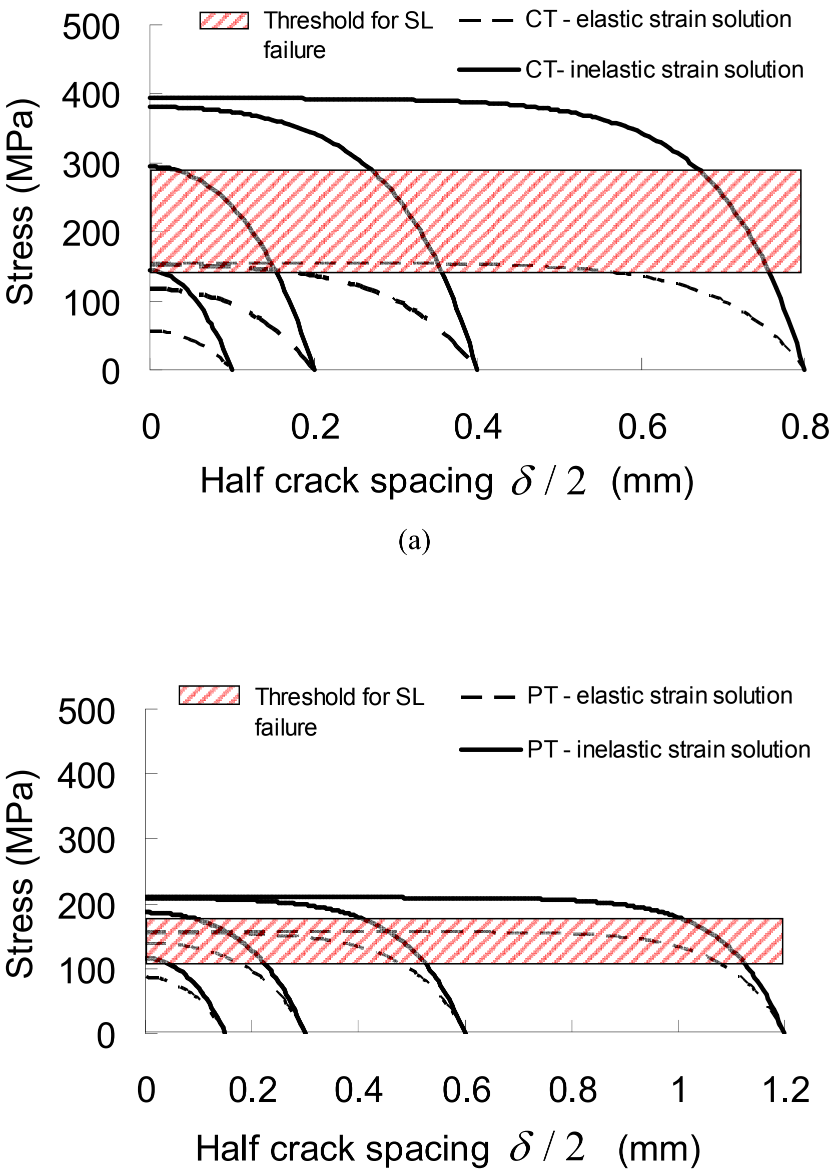

(a)

(b)

Figure 32. Axial stress profiles versus the crack spacing in the SL of TiNiCu SMA wire actuators subject to 154 MPa nominal stress, (a) for complete and (b) partial transformation cycles.

3.3. Fatigue life modeling under corrosive conditions

In the previous section, a shear-lag analysis was used to analyze circumferential crack formation and the associated saturation mechanism that was observed in Section 3. However, to perform fatigue life prediction, a new approach is introduced. The purpose of this section is to develop a fatigue life model using results from the analysis of the damage evolution coupled with Miner's rule, and two approaches are presented. One approach is semi-predictive using both corrosion-free and corrosion fatigue data, and is referred to as direct Miner's rule. The second approach is fully predictive using only corrosion fatigue data to predict results in corrosion-free conditions, and is referred to as inverse Miner's rule.

3.3.1. Stress renormalization procedure using cracked surface layer evolution

The formation of circumferential cracks results in SMA actuators no longer subject to a nominal stress $\sigma_{applied}$ but to a larger stress. In this Section, the cracks are assumed to exist in the material, with a theoretical thickness equal to zero at the beginning of the experiments. From this assumption, a damage accumulation law is identified for which the crack depth measurements made in Section 2 and shown in Figure 26 are plotted against the number of cycles to failure, and are shown in Figure 33. Considering the sole action of corrosion, the surface layer would strictly consist of an oxide layer and its evolution law would be parabolic due to the absence of repeated actuation [64, 65]. However, in the current study, corrosion is coupled with transformation cycles under constant stress. Assuming that there is no initial oxide layer, to the exception of a passivation layer a few nanometers thick [59], the data presented in Figure 33 are approximated with a linear equation using a least square approximation technique, enforced to be equal to zero, at zero cycle.

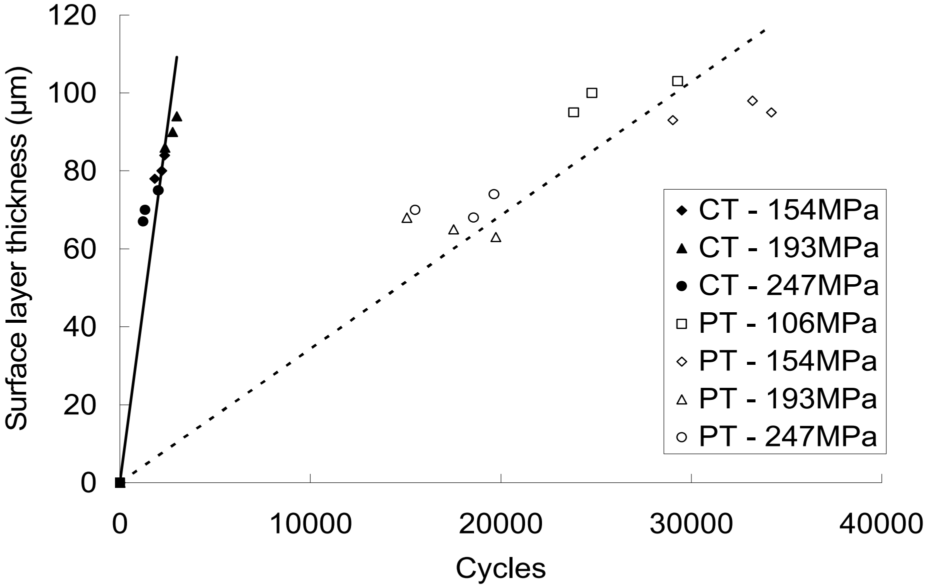

Figure 33. Experimental measurement of surface layer thickness (crack depth) with respect to the number of cycles to failure. Experimental data is shown for complete transformation (CT) and partial transformation (PT).

The crack depth, related to the formation of a damaged surface layer and defined as e_{SL}^{CT} in complete transformation and e_{SL}^{PT} in partial transformation, is expressed as a linear function of the number of cycles N, as shown in Eqs. (39) and (40), respectively.

$$e_{SL}^{CT}\left(N\right)=\gamma^{CT}N \tag{39}$$

$$e_{SL}^{PT}(N) = \gamma^{PT} N \tag{40}$$

With γ^{CT} and γ^{PT} damage accumulation coefficients for complete and partial transformations, respectively. In reality, the formation of damage corresponds to an incremental accumulation of damage as the number of cycles increases towards the final failure of the SMA actuators. However, the proposed formulation using a linear relationship between the damaged surface layer and the number of cycles results in the definition of continuous damage formation. The transition from discrete to continuous enables to work with integral formulations rather than with summations. This transition is the basis for the proposed modeling approach.

The continuous renormalization of the actual applied stress to the SMA wire actuators can therefore be expressed from the nominal stress level applied to the SMA actuators, as shown in Eqs. (41) and (42).

$$\sigma_{renorm}^{CT}(N) = \frac{\sigma_{applied}}{c_{SMA}^{CT}(N)} \quad \text{and} \quad \sigma_{renorm}^{PT}(N) = \frac{\sigma_{applied}}{c_{SMA}^{PT}(N)} \tag{41}$$

$$c_{SMA}^{CT}(N) = \left(\frac{R - e_{SL}^{CT}(N)}{R}\right)^2 \quad \text{and} \quad c_{SMA}^{PT}(N) = \left(\frac{R - e_{SL}^{PT}(N)}{R}\right)^2 \tag{42}$$

$\sigma_{applied}$ is the nominal applied stress level to the SMA actuator prior to corrosion and crack formation. R is the initial radius of the actuator, and σ_{renorm}^{CT} and σ_{renorm}^{PT} are the averaged renormalized stress level due to the growth of circumferential cracks at the surface of the SMA actuators.

3.3.2. Fatigue life modeling using Miner's rule

Miner's rule is one of the oldest approaches to fatigue life correction due to variable cyclic loading. In conventional metal fatigue, Miner's rule is applied to varying stress levels that result in different levels of damage accumulated over the life of the metallic component. In the case of the SMA wire actuators investigated in this work, the damage is characterized by a continuous stress increase due to circumferential crack growth.

The fatigue life or total fatigue life of a component is divided into initiation life and propagation life. The initiation life corresponds to the microscopic phenomena that occur upon cyclic loading leading to the initiation of a first crack, which is usually very difficult to identify, while propagation life corresponds to the propagation of an initiated crack that reached the macroscopic scale resulting in nearly constant crack growth under cyclic loading [66]. While a fracture mechanics framework would allow more accurate results on the propagation contribution of the fatigue life, the initiation part, in the other hand, can be inaccurate. In the specific case of SMA wire actuators tested under corrosive conditions, the stress renormalization procedure is applied from the beginning of the cycles, as the coupling between corrosion and cyclic phase transformation is induced from the first cycle until failure. This indicates that we assume a crack with a theoretical thickness equal to zero that is growing until failure occurs. A fracture mechanics approach requires an initial crack size to monitor its evolution and propagation until the crack reaches a critical size leading to instability and final failure.

The proposed assumption represents the basics for the application of Miner's rule in our case. This model corresponds to the first attempt to model the fatigue life of SMA wire actuators under coupled cycle phase transformation and corrosion.

3.3.2.1 Model formulation

The stress renormalization procedure, i.e. damage accumulation formulation, can be schematically represented for each nominal applied stress level, as shown in Figure 34.

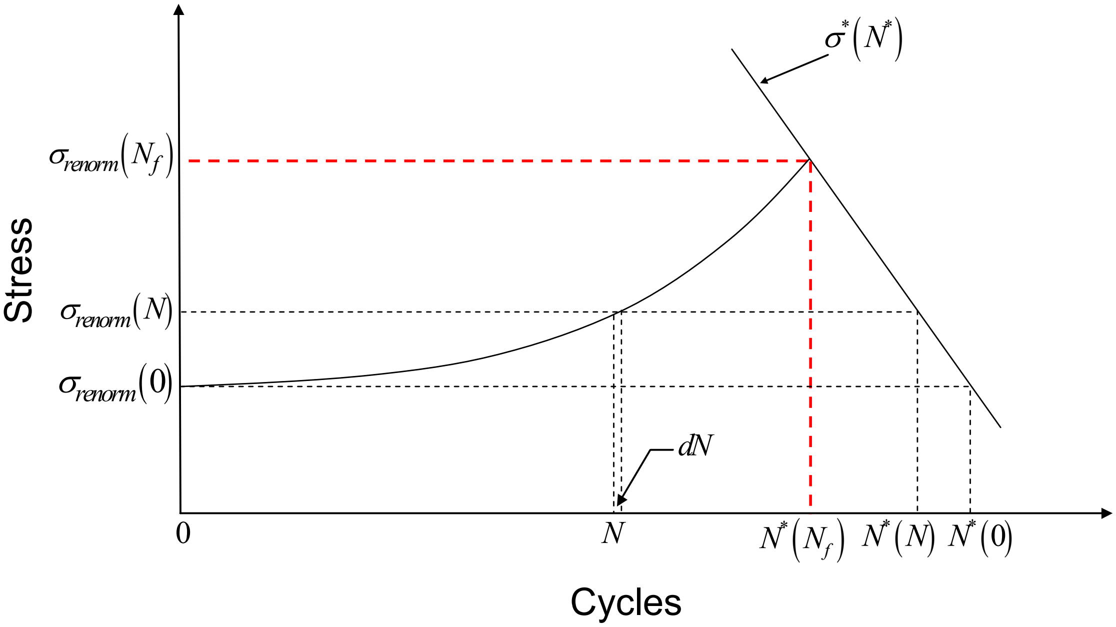

Figure 34. Representation of the renormalized applied stress level and corresponding available cycles to failure from corrosion-free fatigue limit to corrosion fatigue life reduction.

The fatigue data obtained in corrosion-free environment allows the definition of the continuous corrosion-fatigue life shown in Figure 19 with their respective equations summarized in Table 7.

Table 7. Semi-logarithmic curve fitting equations from Figure 19, measured in MPa.

Transformation	Corrosive conditions	Corrosion-free conditions
Complete transformation	$\sigma(N) = -87.7\ln(N) + 860.6$	$\sigma(N^*) = -95.8\ln(N^*) + 1057.9$
Partial transformation	$\sigma(N) = -151.5\ln(N) + 1689.7$	$\sigma(N^*) = -147.3\ln(N^*) + 1723.6$

The fatigue life equations are linear in the semi-logarithmic space; therefore they are defined as semi-logarithmic functions, as shown in Eqs. (43) and (44). The corrosion-free fatigue life can be written as shown in Eq. (43).

$$\sigma^*\left(N^*\right) = A^* \ln\left(N^*\right) + B^* \tag{43}$$

With N^*, σ^*, A^* and B^* the number of cycles to failure under corrosion-free conditions, the corrosion-free nominal stress level applied to SMA wire actuator that will result in a number of cycles to failure N^*, the slope and the position of the corrosion-free stress-life equation, respectively. The corrosion fatigue life can be written in a similar manner, as presented in Eq. (44).

$$\sigma_{corr}\left(N_f\right) = A_{corr} \ln\left(N_f\right) + B_{corr} \tag{44}$$

With $N_f, \sigma_{corr}, A_{corr}$ and B_{corr} the number of cycles to failure under corrosive conditions, the nominal stress level applied to the SMA wire actuator under corrosive conditions that will result in the number of cycles to failure N_f, the slope and the position of the corrosion stress-life equation, respectively.

The assumption is made that the stress level increase due to damage accumulation results in the reduction of the number of cycles to failure of an equivalent SMA actuator, tested in corrosion-free conditions. This assumption allows to define the number of cycles to failure in corrosion-free conditions N^* with the number of cycles at which damage is introduced N, as graphically shown in Figure 34, and expressed in Eq. (45) and Eq. (46).

$$\sigma_{renorm}\left(N\right) = \sigma^*\left(N^*\right) \tag{45}$$

$$N^*\left(N\right) = e^{\frac{1}{A^*}\left(\left(\frac{R}{R-e_{SL}(N)}\right)^2 \sigma_{applied} - B^*\right)} \tag{46}$$

In order to use the Miner's rule, a damage fraction needs to be defined. The infinitesimal damage fraction dD is the infinitesimal number of cycles dN consumed at the stress level $\sigma_{corr}\left(N\right)$ over the corresponding number of cycles to failure under corrosion-free conditions $N^*\left(N\right)$.

$$dD = \frac{dN}{N^*\left(N\right)} \tag{47}$$

The summation of the damage fractions over the number of cycles to failure N_f is theoretically equal to one and has been found experimentally to range between 0.7 and 2 [35, 67, 68, 69], as given in Eq. (48).

$$0.7 \le \int_0^{N_f} dD \le 2 \tag{48}$$

The variation in the values is due to the variations in the load history, i.e. low-high and high-low load conditions for example [35], and the rule was found to be more accurate when damage was following a low-high load history. Here, the SMA actuator is continuously accumulating damage with a damage level that is stress dependent. Those conditions are favorable to the use of Miner's rule. Hence, we propose the formulation of a continuous Miner's rule using continuous damage accumulation. The continuous Miner's rule can be written as shown in Eq. (49).

$$\int_{N=0}^{N=N_f} \frac{1}{e^{\frac{1}{A^*}\left(\left(\frac{R}{R-e_{SL}(N)}\right)^2 \sigma_{applied} - B^*\right)}} dN = 1 \tag{49}$$

The proposed Miner's rule can be directly applied to a damage law due to corrosion and to corrosion-free fatigue results to determine the number of cycles to failure under corrosive conditions. However, by taking a inverse approach, corrosion-free fatigue life can be predicted from corrosion fatigue results and damage evaluation. The two different approaches will be discussed next.

3.3.2.2. Direct Miner's rule

In order to determine the number of cycles to failure under corrosive conditions, the knowledge of the nominal applied stress $\sigma_{applied}$, of the damage evolution equation $e_{SL}\left(N\right)$, of the stress renormalization function $\sigma_{corr}\left(N\right)$ and of the corrosion-free fatigue life $\sigma^{*}\left(N^{*}\right)$ is needed to be able to predict the number of cycles to failure N_f. This is what the authors define to as direct Miner's rule. Its resolution requires the computation of one non-linear integral equation with the unknown N_f, as shown in Eq. (49). The numerical solution from the non-linear equation yields a number of cycles to failure per each nominal stress level $\sigma_{applied}$. The predictions for complete and partial transformation conditions performed in a corrosive environment are shown in Figure 35 and Figure 36, respectively.

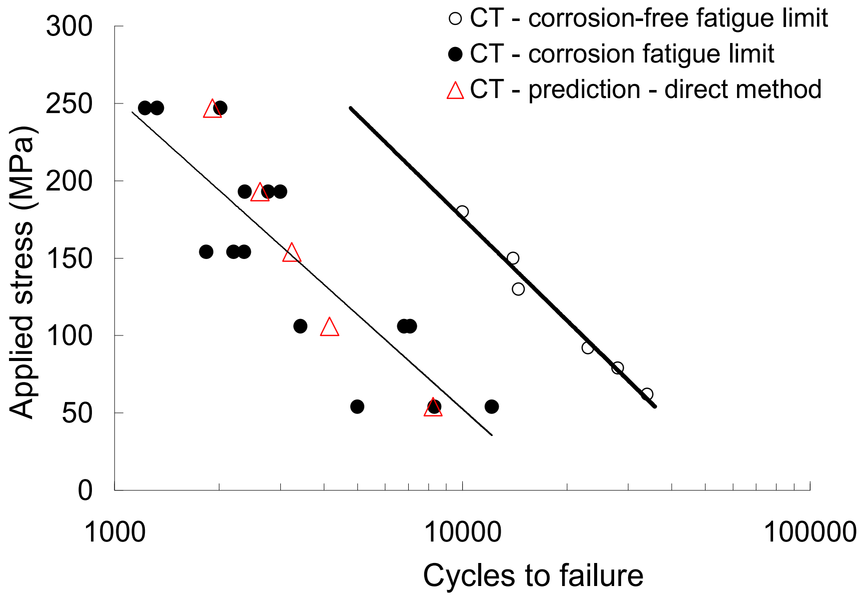

Figure 35. Direct Miner's rule: comparison of corrosion fatigue life predictions to experimental corrosion fatigue data, for complete transformation cycles.

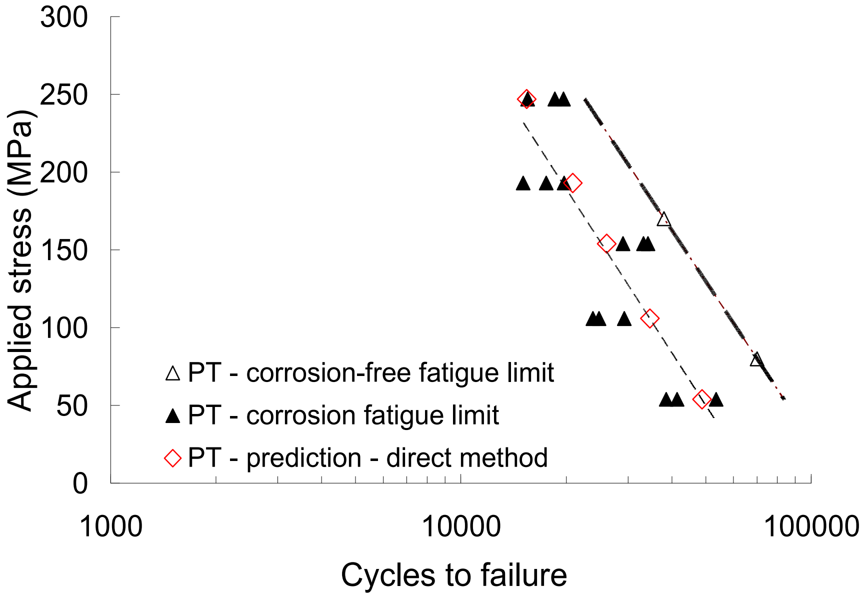

Figure 36. Direct Miner's rule: comparison of corrosion fatigue life predictions to experimental corrosion fatigue data, for partial transformation cycles.

The main result is that the predictions are found well between the experimental data, which indicates that the model is working well under such conditions. Furthermore, the damage evolution shown in Figure 33 was modeled with fatigue data corresponding to stress levels ranging between 154 MPa and 247 MPa for complete transformation and between 106 MPa and 247 MPa for partial transformations. Therefore, the determination of the number of cycles to failure N_f for nominal stress levels of 54 MPa and 106 MPa in complete transformation and 54 MPa in partial transformation is predictive and represents a way to validate the model assumptions. The results from the predictions under such stress levels also show excellent agreement with the experimental, hence validating the model formulation.

3.3.2.3. Inverse Miner's rule

The direct method is however limited in the sense that it requires both corrosion and corrosion-free fatigue data. Hence the definition of the inverse Miner's rule to make use of only corrosion fatigue data in order to define a fully predictive model to model the corrosion-free fatigue life of SMA actuators.

In the inverse Miner's rule, the inputs to the model are the nominal applied stress level $\sigma_{applied}$, the damage evolution $e_{SL}(N)$, the stress renormalization function $\sigma_{corr}(N)$ and the number of cycles to failure N_f where the unknown is the corrosion-free fatigue life $\sigma^*(N^*)$. The direct Miner's rule was producing a number of cycles to result for each nominal applied stress level. Here, the inverse Miner's rule is slightly more complicated in the sense that to define the number of cycles under corrosion-free conditions N^*, one needs to determine the coefficients A^* and B^*, introduced in Eq. (43). From experimental results in both corrosive and corrosion-free testing conditions, the slopes of the applied stress versus cycles to failure curves are very similar, for both complete and partial transformation conditions, as shown in Figure 19 and Table 7. This experimental result permits rewriting Eq. (43) with the coefficient B^* remaining unknown, as shown in Eq. (50).

$$\sigma^*\left(N^*\right) = A_{corr} \ln\left(N^*\right) + B^* \tag{50}$$

The new formulation for the cycles to failure in corrosion-free testing conditions simplifies the problem from a highly non-linear system of integral equations in A^* and B^* to a series of equations for which the remaining unknown is B^*. To each nominal applied stress levels $\sigma_{applied}$ corresponds a unique value for B^*, which are then averaged to give the predictions shown in Figure 37 and Figure 38. To ensure reasonable results and to avoid any upper and lower bounds in the selected stress levels, the B^* coefficients are calculated for nominal stress levels equal to 106, 154 and 193 MPa. The determination and averaging of the B^* coefficients yields average values equal to 1093.6 and 1757.5, for complete and partial transformations, respectively. The results show good agreement with the experimental fatigue data obtained under corrosion-free conditions, for both complete and partial transformation conditions. The predictions are slightly conservative and validate the definition of the inverse Miner's rule.

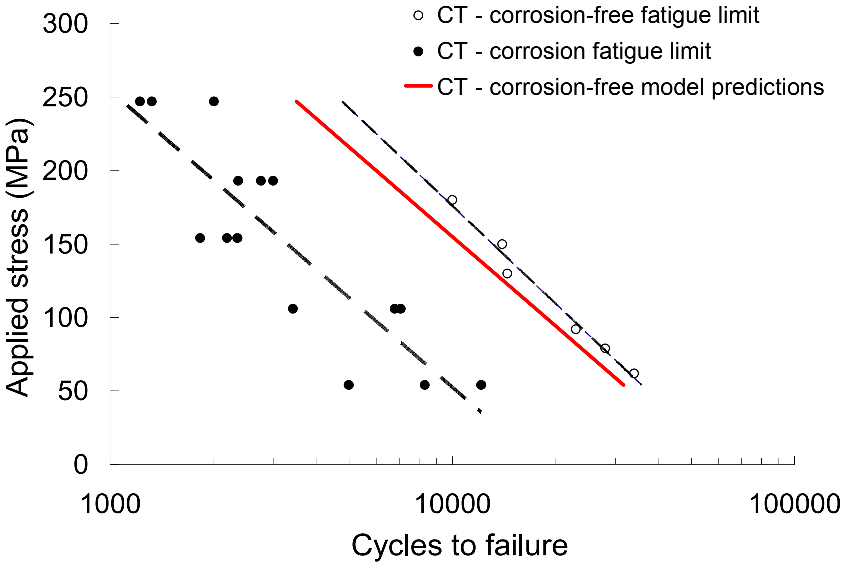

Figure 37. Inverse Miner's rule: comparison of corrosion-free fatigue life predictions to experimental corrosion-free fatigue data, for complete transformation cycles.

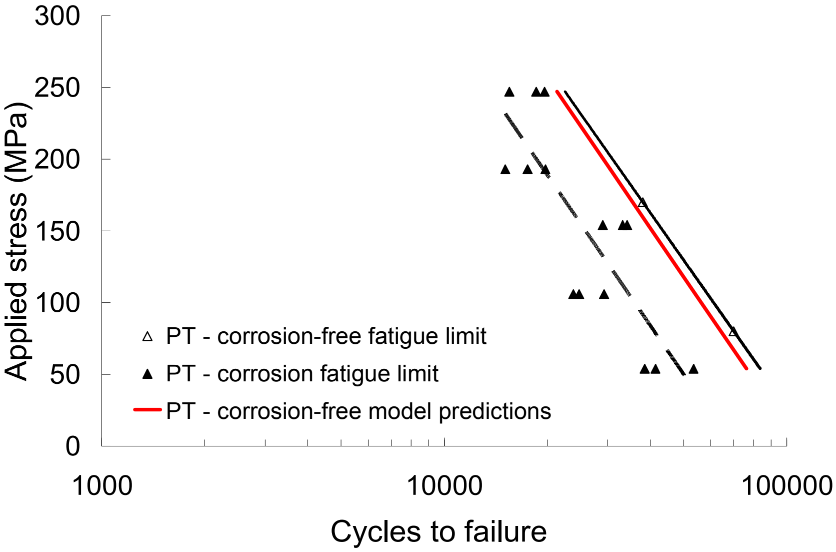

Figure 38. Inverse Miner's rule: comparison of corrosion-free fatigue life predictions to experimental corrosion-free fatigue data, for partial transformation cycles.

The results show satisfying agreements to the experimental data and damage accumulation under corrosive conditions modeling using stress correction function coupled with a Miner’s rule of damage accumulation. The model demonstrates less accurate predictions towards higher stress levels. The modeling of stress correction at high stress and of fatigue life predictions due to corrosion is more likely to generate errors. The errors are due to the development of very high stresses that are no longer admissible in the frame of low-cycle fatigue but more in an intermediate one, i.e. between monotonic and low-cycle fatigue regime. Therefore, the response of the material is expected to differ. Despite the observed relatively low discrepancies between the numerical and experimental results, we can conclude that the damage accumulation theory using a nominal stress correction criterion due to crack formation is a valid approach to represent the influence of corrosion on the fatigue response of SMA actuators.

Table 8. List of parameters used for the direct and inverse Miner's rule.

Direct Miner's rule parameters

	Complete transformation (CT)	Partial transformation (PT)
SMA actuators wire radius R	$R = 0.3mm$	$R = 0.3mm$
Surface layer evolution coefficient γ	$\gamma^{CT} = 36.4\times10^{-6} mm/N$	$\gamma^{PT} = 3.4\times10^{-6} mm/N$
Corrosion-free stress-life equation coefficients	$A^* = -95.8MPa/N^*$ $B^* = 1057.9MPa$	$A^* = -147.3MPa/N^*$ $B^* = 1723.60MPa$
Corrosion stress-life equation coefficients	$A_{corr} = -87.7MPa/N^*$ $B_{corr} = 860.6MPa$	$A_{corr} = -151.5MPa/N^*$ $B_{corr} = 1689.7MPa$

Inverse Miner's rule parameters

	Complete transformation (CT)	Partial transformation (PT)
SMA actuators wire radius R	$R = 0.3mm$	$R = 0.3mm$
Surface layer evolution coefficient γ	$\gamma^{CT} = 36.4\times10^{-6} mm/N$	$\gamma^{PT} = 3.4\times10^{-6} mm/N$
Corrosion-free stress-life equation coefficients	$A^* = A_{corr} = -87.7MPa/N^*$ $B^* = 1057.9MPa$	$A^* = A_{corr} = -151.5MPa/N^*$ $B^* = 1723.6MPa$

CHAPTER IV

TRANSFORMATION INDUCED FATIGUE OF Ni-RICH NiTi SMA ACTUATORS: EXPERIMENTS AND RESULTS

In this chapter, the transformation induced fatigue testing of Ni-rich NiTi SMA actuators will be presented. The purpose of this chapter is driven by the new and unique properties of the precipitation hardening found in Ni-rich NiTi SMAs. The enhanced cyclic stability and training ability of the alloy make it a premium choice for the aerospace industry and their potential applications [45, 48, 49]. The need for the Boeing Company to determine and certify the fatigue life of SMA actuators for future jet noise reduction applications is another element that confirms the necessity to investigate the transformation induced fatigue life of Ni-rich NiTi SMA actuators [14, 15]. As a new class of material, the Ni-rich NiTi SMA is still under investigation. However, the dominant factor of failure in complex structures is cyclic loading.

Constant stress thermally induced transformation cycles will be performed on small dogbone SMA actuators. A parametric study on the cyclic response and transformation fatigue behavior of Ni-rich NiTi SMAs led to the optimization of several material/process and test parameters, namely: the applied stress range, the heat treatment, the heat treatment environment and the specimen thickness. The purpose of this thermomechanical fatigue study is to evaluate the shape recovery stability, the influence of large applied stresses, the amount of permanent deformation and the resulting failure mechanisms in Ni-rich NiTi SMA actuators.

Due to different processing methods, different surface properties are found to have an influence on the fatigue life. Recast layer form upon wire EDM cutting and an oxide layer form upon heat treatment; therefore all surface layers were removed. Then an ultra-fine surface finish (0.1µm) is applied to eliminate any external factors such as oxide layer/recast layer, microcracks and other surface defects (discussed in Chapter V).

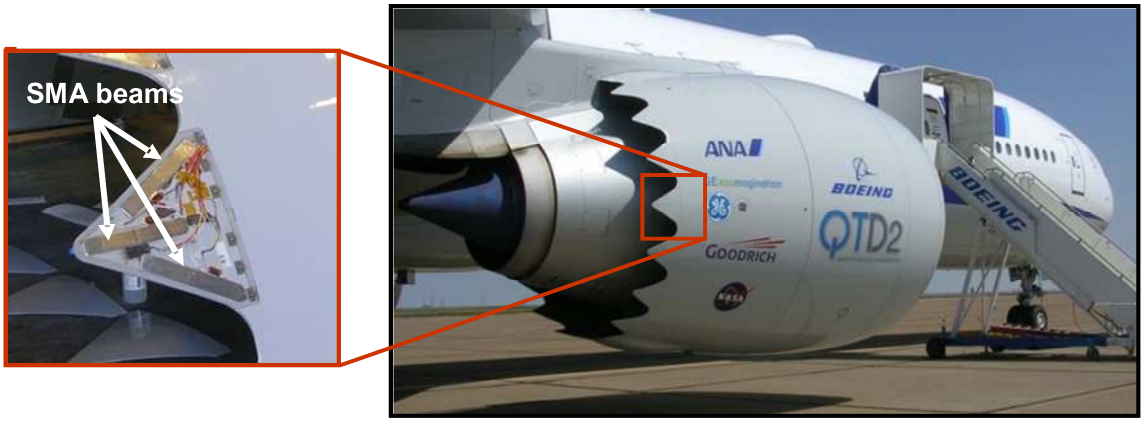

Figure 39. Boeing Variable Geometry Chevrons at the fan nozzle of jet engines for noise reduction [15].

4.1. Fatigue test specimens

The material used in this work is a Ni-rich $Ni_{60}Ti_{40}$ (wt.%) Shape Memory Alloy. The geometry of the specimens was driven by the fatigue frames capabilities and by the configuration of the actual VGC application. The fatigue frame used to perform fatigue testing has a load capacity of nearly 100 lbs (~ 45 kg), therefore loads transmitted to the SMA actuators through application of a dead weight cannot be higher than 33 lbs per specimen, as the fatigue frame can test three Ni-rich NiTi fatigue specimens at a time. The beam geometry of the actual SMA actuator for the VGC application is designed as a curved constant stress profile beam, i.e. cross-section reduction from the root towards the tip (Beam design proprietary of Boeing), as shown in Figure 40. The beam dimensions are 10 in (254 mm) long and 1.5 in (38.1 mm) wide, and a thickness ranging between 0.065 in (1.65 mm) at the tip and 0.175 in (4.45 mm) at the root.

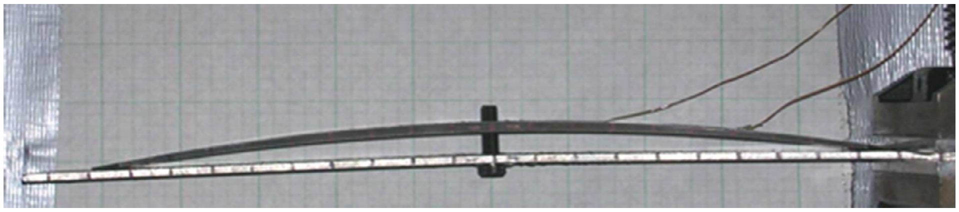

Figure 40. Ni-rich NiTi SMA curved beam profile clamped against aluminum elastic structure for load-displacement analysis.

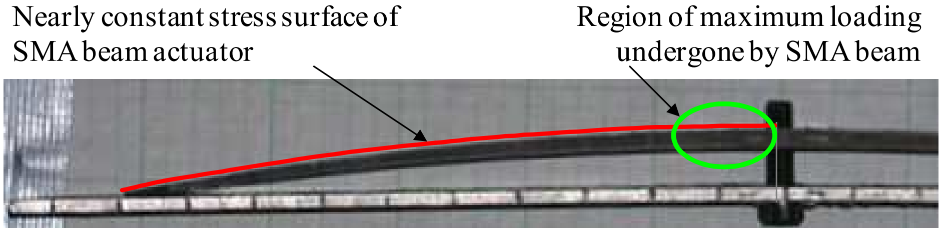

Figure 41.Ni-rich NiTi SMA beam actuator with highlighted nearly constant stress profile and location of maximum stress fields.

Due to the bending nature of the SMA beam actuation, surface stresses are maximum. The presence of tapped holes in the SMA beam will account for additional stress concentration, therefore without additional external damage; repeated loading of the SMA beam is most likely to initiate cracks and failure at the root. In order to represent fatigue damage and failure in a similar geometry, thin dogbone specimens with a thickness to width ratio similar to the one seen in the actual SMA actuators mounted onto the VGCs, seen in Figure 42.

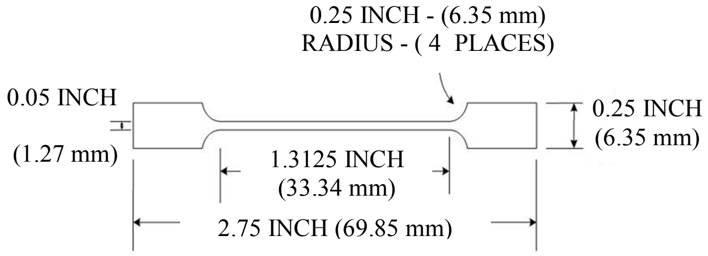

Figure 42. Drawing of the selected shape for Ni-rich NiTi fatigue test specimen.

With a total length of 2.75 in (69.85 mm) and a test gauge of 1.3125 in (33.34 mm), three different thicknesses were selected to assess any size effect on the fatigue life. The three selected thicknesses were 0.005, 0.01and 0.015 inches (0.127, 0.254, and 0.381 mm respectively).

4.2. Heat treatments, transformation temperatures and thermomechanical response

4.2.1. Heat treatments

One particular property of the Ni-rich $\mathrm{Ni_{60}Ti_{40}}$ SMA is that it can exhibit SME without any cold work process [50, 51]. The presence of precipitates favors the storing of elastic energy and therefore the realization of recoverable strains upon martensitic phase transformation [45, 46]. The proportions, the distribution and the composition of the precipitates can be modified / adjusted by applying appropriate heat treatments [44, 48]. The heat treatments consist of a homogenization treatment of one hour at 850°C with furnace controlled cooling (FC) to allow homogenization and formation of precipitates. The shape-set is then followed by an aging treatment of either 1 or 20 hours at 450°C, subsequently followed by water quench cooling (WQ). A summary of the different heat treatments is given in Table 9. The selected heat treatments were chosen to have different thermomechanical response with different hysteresis and transformation temperatures due to the high precipitation and Ni-rich exchange between the NiTi matrix and the Ni-rich precipitates [45, 50, 51] but also in order to obtain transformation temperatures for one heat treatment (HT#1) with a low M_{0f} allowing passive transformation into the martensitic phase when reaching cruising flight altitudes and HT#2 with a higher M_{0f} to allow the active control of the actuation from the inside of the airplane [15, 49].

Table 9. Identification and description of the different applied heat treatments.

Shape-Set Treatment	Homogenization: 1 hr. @ 850°C + 12 hrs. FC
Heat Treatment #1 (HT#1)	Homogenization: 1 hr. @ 850°C + 12 hrs. FC + Aging: 1 hr. @ 450°C + WQ
Heat Treatment #2 (HT#2)	Homogenization: 1 hr. @ 850°C + 12 hrs. FC + Aging: 20 hr. @ 450°C + WQ

4.2.2. Transformation temperatures

After the presentation of two different heat treatments, HT#1 and HT#2, the determination of the transformation temperatures is needed to characterize any differences due to microstructural modifications in terms of precipitates. For this purpose, a differential scanning calorimeter (DSC) was used to determine the transformation temperatures under zero-stress, as seen in Figure 43 and Figure 44. The method of intersecting tangents was used to determine the zero-stress transformation temperatures indicated in Table 10. The latent heat of transformation can be estimated by calculating the peak area defined by the onset and end of transformation. It appears clearly that HT#2 (Figure 44) has a larger latent heat of transformation than in HT#1 (Figure 43).

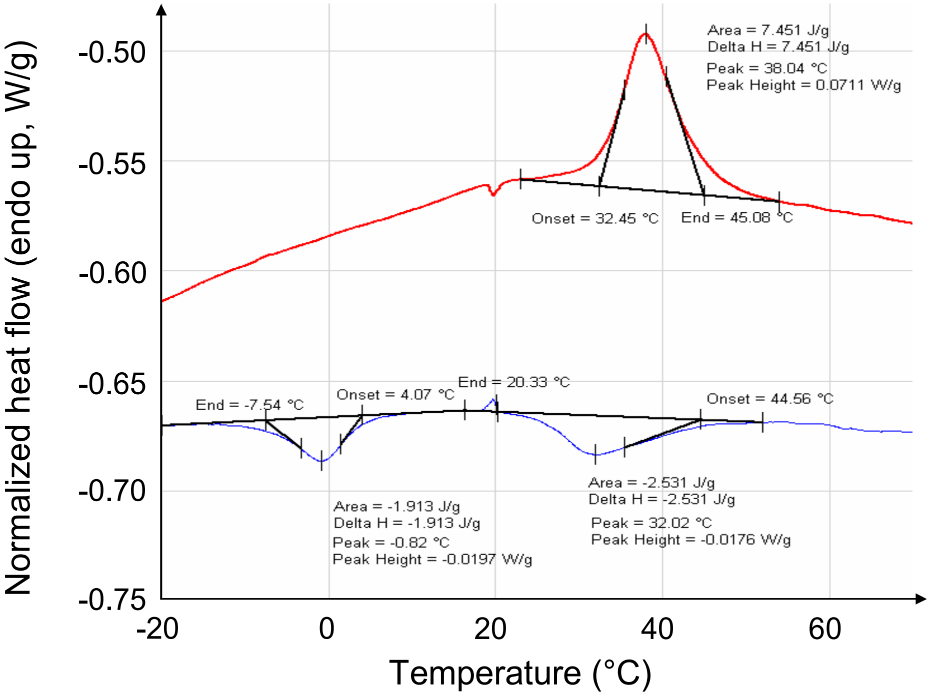

Figure 43. DSC results for $Ni_{60}Ti_{40}$ SMA for HT#1: tangent method applied to determine transformation temperatures.

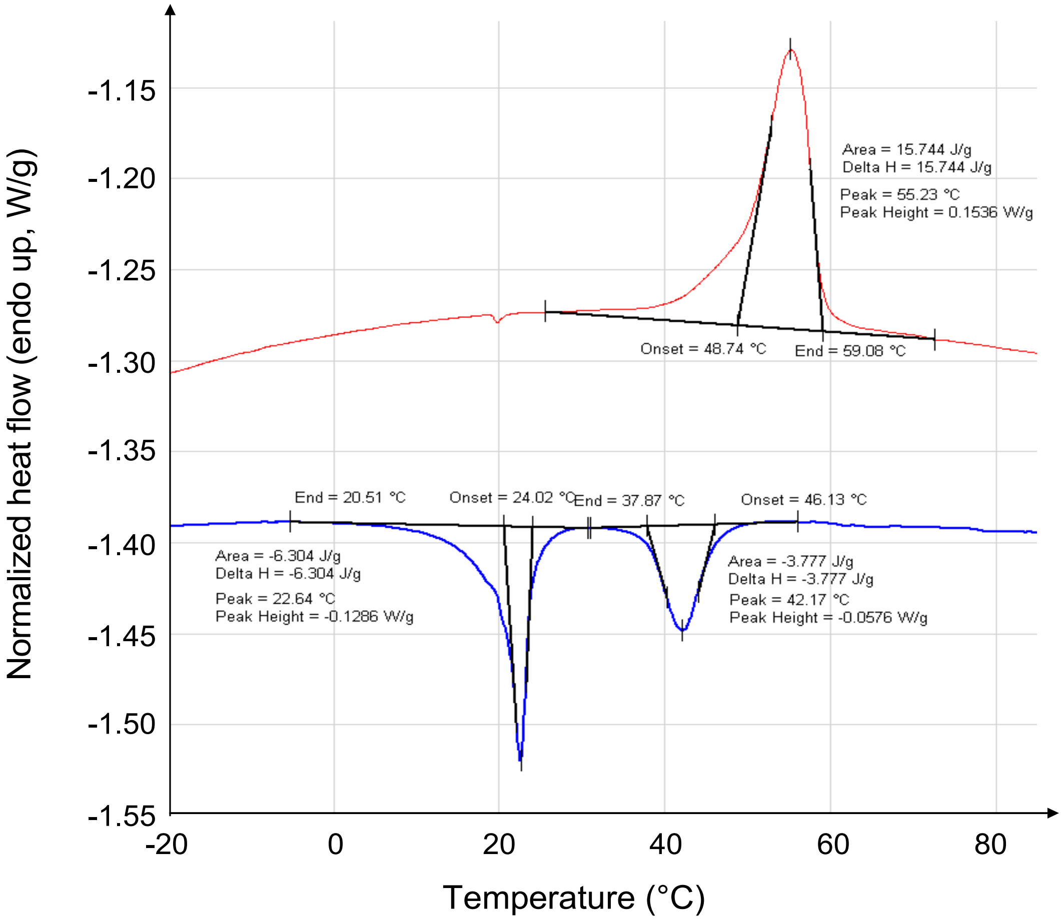

Figure 44. DSC results for $Ni_{60}Ti_{40}$ SMA for HT#2: tangent method applied to determine transformation temperatures.

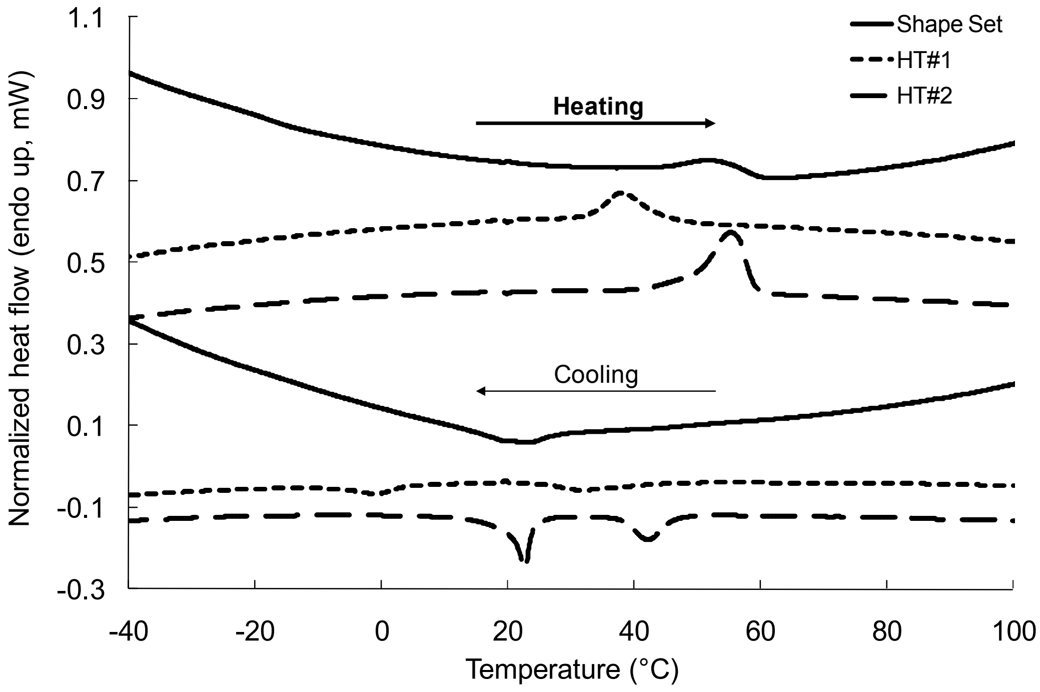

Figure 45. Summary and comparison between DSC results for $Ni_{60}Ti_{40}$ SMA processed with the two different heat treatments HT#1 and HT#2, compared to the initial shape-set treatment transformation temperatures.

Table 10. Transformation temperatures for $Ni_{60}Ti_{40}$ SMA.

HT#1	M_{0s} = 4°C	R_{0s} = 45°C	A_{0s} =32°C
	M_{0f} = -7°C	R_{0f} = 25°C	A_{0f} =45°C
HT#2	M_{0s} = 24°C	R_{0s} = 46°C	A_{0s} =48°C
	M_{0f} = 20°C	R_{0f}= 37°C	A_{0f}=59°C

The results indicate a significant increase of the transformation temperatures from HT#1 to HT#2. One can also identify from Figure 43 and Figure 44 the amount of latent heat of transformation, characterized by the area defined by the peak and the intersecting tangents. The latent heat of transformation observed in HT#1 is much less than in the case for HT#2.

It is also important to note that at zero stress, M_{0f} is below the cooling temperature of the fatigue testing apparatus. However, under the application of non-zero stress and due to the near-linear relationship between transformation temperature and applied stress (Clausius-Clapeyron equation, 8 MPa/°C < C_M < 10MPa/°C, C_M: stress coefficient), the transformation temperature increases (M_f reaches a value of +2.5°C to +5°C when loaded under 100MPa constant stress). Therefore, one can be assured that full transformation cycles were achieved for the selected stress range (100 MPa – 250 MPa).

4.2.3. Thermomechanical response

The relatively high cycling frequency achieved during fatigue testing in the custom built fatigue test frame may have some influence on the completion of the thermomechanical transformation cycles undergone in the SMA specimens. Therefore, near quasi-static thermal actuation tests were achieved on an MTS thermomechanical test frame, for heat treatments HT#1 and HT#2, as shown in Figure 46 and Figure 47, respectively. In order to test such small specimens under constant stress loading conditions, a 150 lbs load cell was used and a heating / cooling chamber was mounted to the frame with extensometer and thermocouples attached to the specimens.

The loading paths for both heat treatments are presented in Figure 48. The loading path is shown for each constant applied stress level, in terms of the zero-stress transformation temperatures. The hysteresis loops for 50 MPa, 150 MPa and 250 MPa are reported in Figure 49 and Figure 50, for HT#1 and HT#2 respectively.

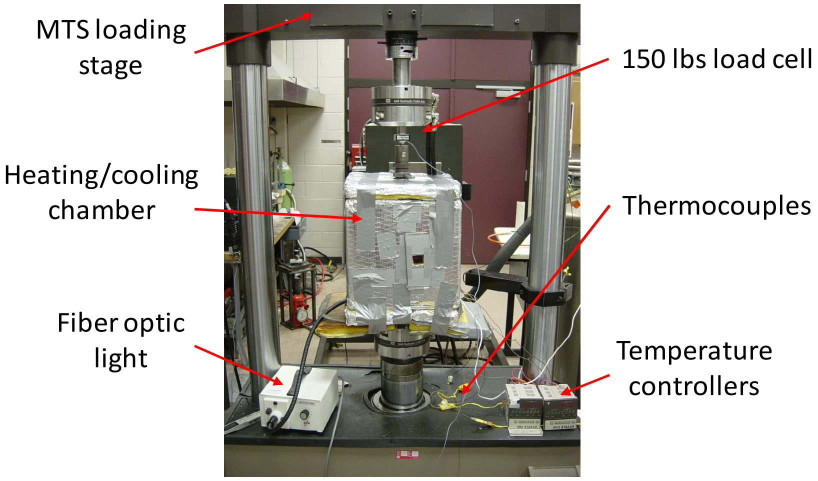

Figure 46. Overview of the MTS thermomechanical test frame with heating/cooling chamber.

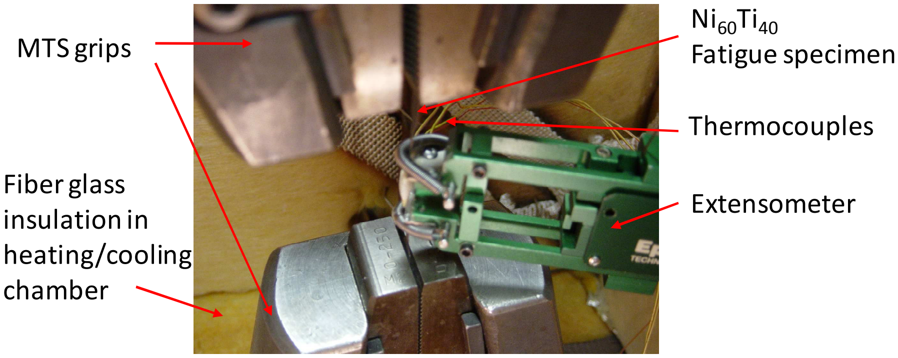

Figure 47. Inside view of the heating/cooling chamber with fatigue test specimen mounted in MTS loading stage with thermocouples and extensometer.

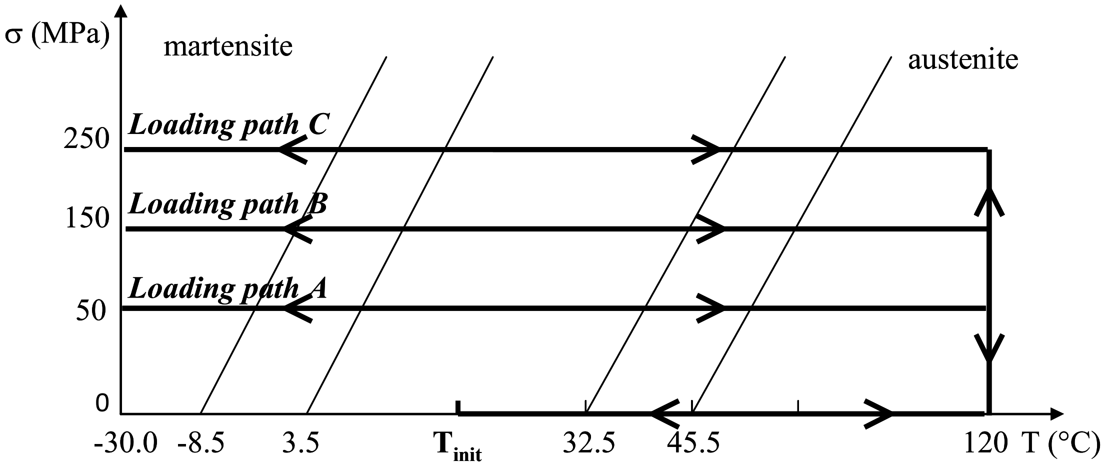

(a)

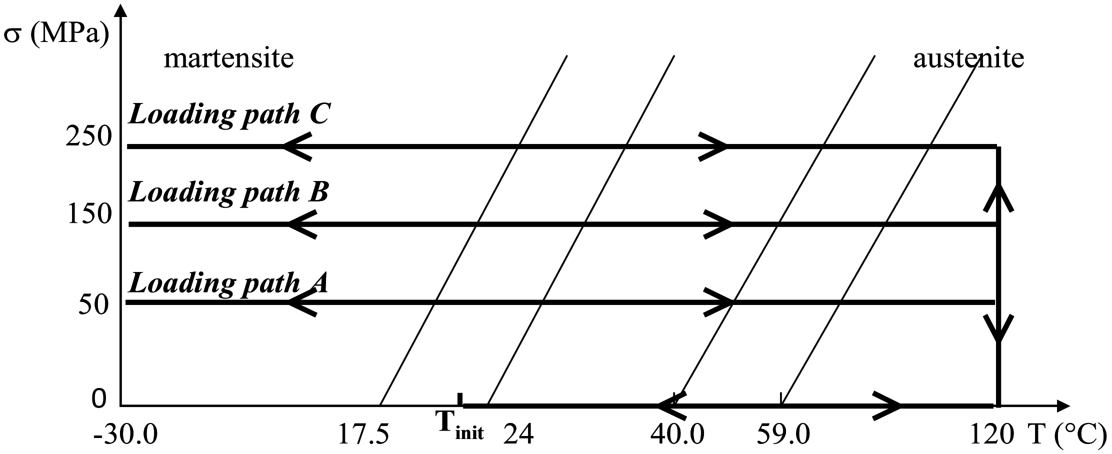

(b)

Figure 48. Loading paths for (a) heat treatment HT#1 and (b) heat treatment HT#2 with T_{init} = room temperature.

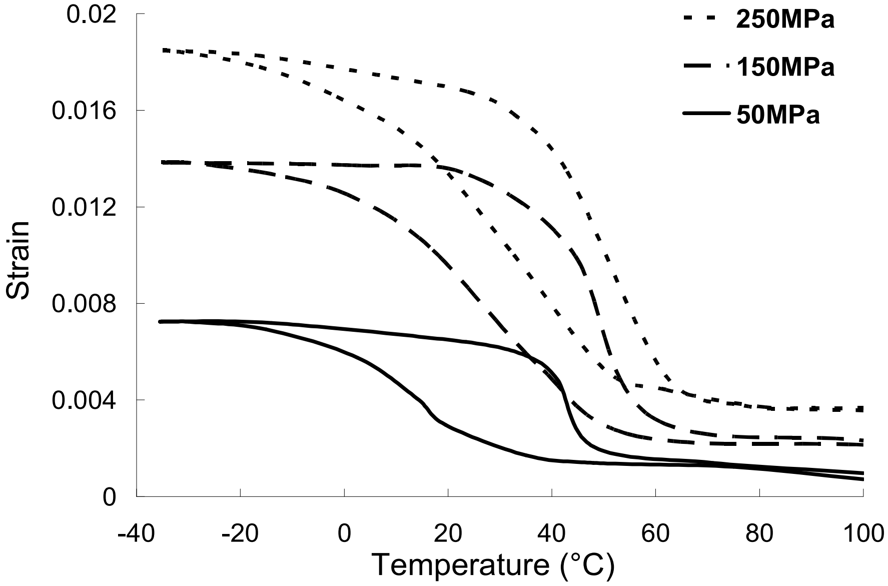

Figure 49. Constant stress hysteresis loops for $Ni_{60}Ti_{40}$ SMA aged under HT#1 conditions.

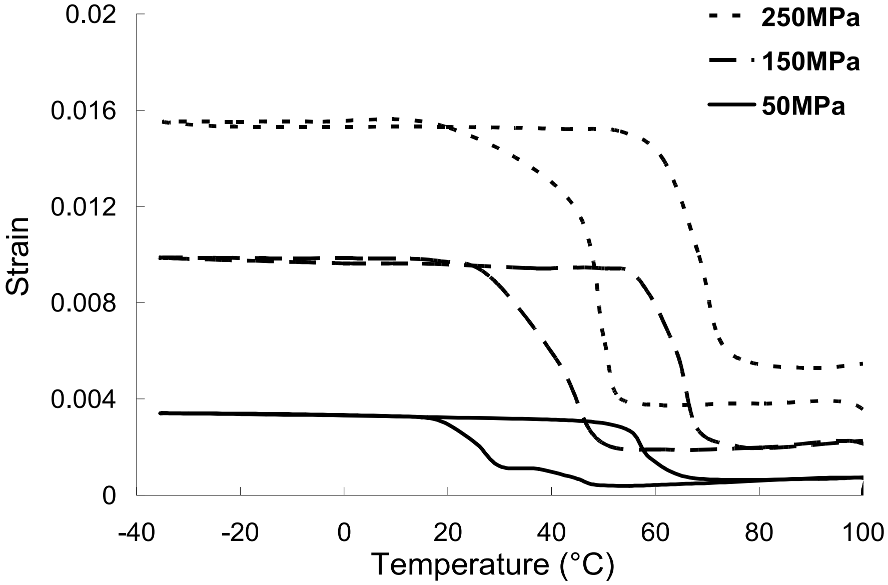

Figure 50. Constant stress hysteresis loops for $Ni_{60}Ti_{40}$ SMA aged under HT#2 conditions.

From the tests performed under quasi-static conditions for HT#1, we can observe smooth phase transitions with low residual strain upon completion of the thermomechanical cycle. In the case of HT#2, we can see sharp phase transitions with a consequential amount of non-recoverable strain upon completion of the thermomechanical cycle. One can see from both tests (HT#1 and HT#2) that under 50 MPa stress level the R-phase identified during the DSC measurement is visible with a two stage transition upon cooling. Under larger stress levels, the R-phase is transformation is not visible anymore due to the large detwinning generated during the martensitic transformation.

The amount of recoverable strain generated for both HT#1 and HT#2 from the quasi-static testing are reported in Table 11 and are compared to values obtained in the fatigue frame.

Table 11. MTS constant stress test results vs. constant stress test results from fatigue frame.

	50MPa (HT#1 / HT#2)	150MPa (HT#1 / HT#2)	250MPa (HT#1 / HT#2)
MTS loading stage	0.35% / 0.35%	0.7% / 0.75%	1.3% / 1.0%
Fatigue frame	0.25%* / 0.35%*	0.6% / 0.7%	1.1% / 1.0%

*These values were found to be within the measurement noise produced by the LVDTs.

These results validate that the fatigue frame can perform as well as the thermomechanical testing frame in terms of amount of recoverable strain. There was another feature from the different heat treatments that has been identified. The amount of latent heat of transformation in the case of HT#1 is smaller than in the case of HT#2. The specimen that exhibiting the least amount of latent heat of transformation (HT#1) was characterized by a more gradual transformation occurring upon thermal loading under the application of constant stress. The specimen exhibiting the highest amount of latent heat of transformation (HT#2) displayed a sharp and quick transformation under the same conditions. This is another indication that significant microstructural differences were generated with the application of these two different heat treatments.

4.3. Experimental setup and cooling environment

The identification of the loading conditions of the SMA components led to the definition of a series of uniaxial constant load thermal cycles, showed in Figure 51. The following schematic represents the stress-temperature phase diagram of NiTi SMAs. The horizontal double arrow indicates the selected loading path, i.e. constant load thermal cycles. The selected stress range is 100 MPa to 250 MPa to represent the minimum and maximum load generated in the VGC during actuation in service [52].

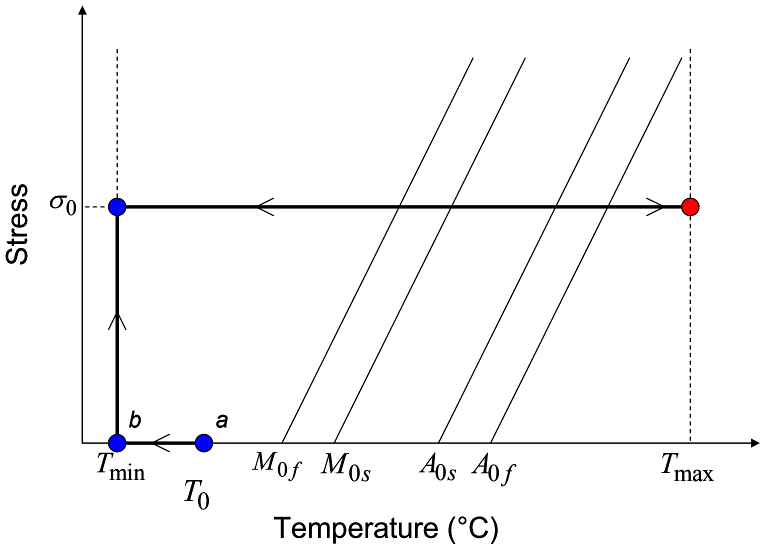

Figure 51. Schematic of the martensitic phase transformation phase diagram for NiTi SMA with a representative constant stress loading path.

The experiments are performed in the same fatigue test frame presented in Chapter II, as shown in Figure 5 and Figure 6. The difference from Chapters II and III however is the selection of a new blend of waterless ethylene and propylene glycol coolant for enhanced corrosion resistance. The selected coolant is NPG+ (non-aqueous propylene glycol) from Evans Cooling systems Inc. the heating and cooling methodology are also identical to what was used in Chapter II. The displacements of the SMA actuators are recorded through LVDT transducers and the strains in the austenitic and martensitic states are used to define total, plastic and recoverable strains. The equations defined in Chapter II, i.e. Eqs. (1) - (12), are still valid and are applied to determine the strains in austenite, martensite as well as the actuation strain. Thermal loading cycles are achieved at a frequency of approximately 0.1 Hz. The advantage of such design is the capacity to produce thermomechanical fatigue data between 48 hours and one week in average.

The results seen in Chapters II and III support the fact that phase transformation induced under resistive heating is sensitive to the cooling environment. Therefore a new custom built fatigue frame using gaseous Nitrogen cooling was developed, as shown in Figure 52 and Figure 53. The glycol coolant temperature was maintained at nearly 5°C which resulted in about 8 seconds cooling time to achieve full forward transformation. The gaseous Nitrogen was sprayed in a closed and insulated chamber that allowed temperatures to reach and maintain a constant -20°C, resulting in similar actuation frequency of approximately 0.1 Hz. Details of the design and specifications of the new fatigue frame using GN2 can be found in [70].

The use of a dry, corrosion-free environment is selected to reflect better the actual working conditions of the SMA beams in the VGCs. The actuators are embedded in a composite substrate that prevents the actuators to be exposed to any corrosive environment. Therefore, corrosion-free fatigue testing of the fatigue test specimens is needed.

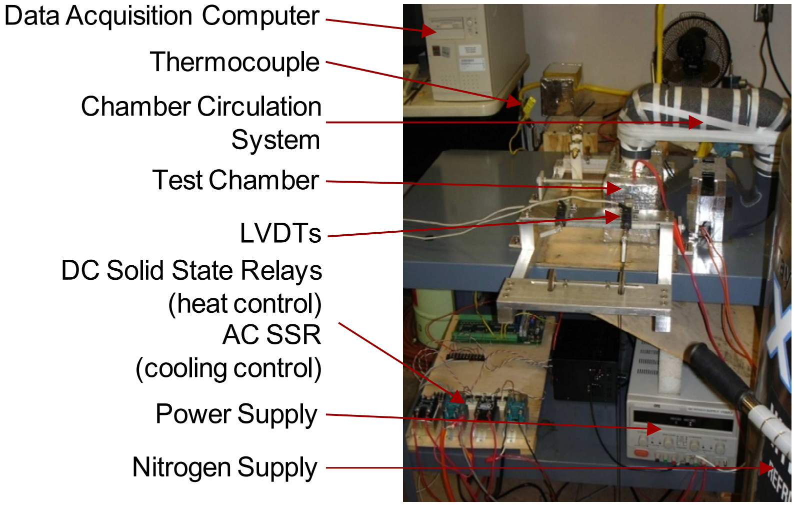

Figure 52. Custom built constant stress fatigue test frame using sprayed gaseous Nitrogen coolant [70].

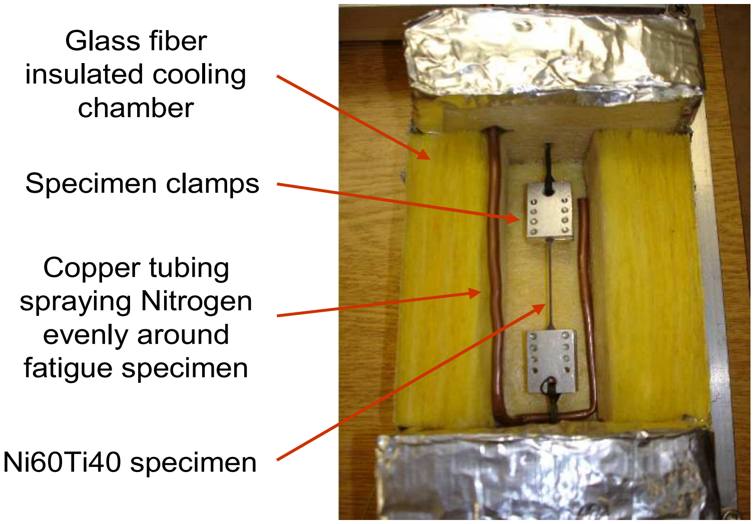

Figure 53. Nitrogen frame environmental chamber [70].

4.4. Selected parameters and fatigue test matrix

The present research effort underlies the analysis of the influence of different parameters on the fatigue response of nickel-rich SMA actuators. The application of thermomechanical cycles is conducted until failure of the SMA specimens is achieved. Therefore, seven different parameters were selected to be scrutinized in terms of influence on the stress life response as well as on the level of accumulated plastic strain at failure. They are divided in two categories, the material and process parameters and the test parameters.

4.4.1. Process parameters

As discussed earlier, Ni-rich NiTi SMA have the unique capacity to exhibit SME by formation of precipitates that affect the local stress field and therefore resulting in assisting the phase transformation in the NiTi matrix. Therefore, heat treatments have become a key parameter to tune and adjust the SMA actuators behavior and performances.

The process parameters are parameters related to the elaboration and thermomechanical treatments that were performed on the material prior to fatigue testing. Hot rolling at 900°C was performed to shape the solidified ingot into large plates from which the actual SMA beam actuators for the VGC application are cut. The fatigue specimens described in subsection 4.2 were also cut from the same hot rolled plate. The post hot rolled material cut to the desired shape, were shape-set. The shape set treatment is a constrained heat treatment at in the range of homogenization temperatures. This treatment is performed at 850°C during one hour and then the material is slowly cooled. The result is the permanent shape of a particular geometry achieved during homogenization treatment, i.e. SMA beam actuators for the VGC is initially flat prior to being clamped on curved fixture and then homogenized. For this study, the shape-set treatment is slightly different with the fatigue test specimen having non constrained heat treatments. After shape setting of the SMA actuators, aging treatments were applied with at lower temperatures and for different times. The selected aging treatments are 450°C during one hour for one set of actuators and twenty hours for the other set of specimens. However, for the aging treatments, water quenching is used to fix the metastable nature of the formed precipitates during aging. The details on the microstructure resulting from the various heat treatments will be discussed in Chapter V.

While the atmosphere does not seem relevant for the aging treatments at 450°C, it becomes a crucial element during the shape set treatment performed at 850°C. Therefore, for production enhancement purposes and identification of its effects, the heat treatments were performed in two different atmospheres, vacuum or air.

4.4.2. Test parameters

Test parameters are numerous, making the identification of the most important parameters more difficult. This is accentuated when the tests are to be performed on a custom designed test setup. However, for SMAs, one can establish a list of parameters common to most SMAs, in the optic of a possible standardization, namely: applied stress level, amount of actuation strain, specimen dimensions, specimen surface quality, testing environment, etc. In this parametric study, the focus is on the applied stress level, the specimen geometry, the heat treatment environment, i.e. high vacuum versus air heat treatment, and the heat treatment time.

Selection of a set of parameters and consolidation of the fatigue data with focus on the influence of surface quality and of the cooling environment will be introduced later in the Chapter and will be the basis for the discussion on the failure mechanisms identified in Chapter V.

The constant applied stress ranges from 100 MPa to 250 MPa in 50 MPa increments. The specimen thickness is a parameter that allows for observation of size effect. The three selected thicknesses were 0.005, 0.01 and 0.015 inches (0.127, 0.254, and 0.381 mm respectively). The selected thicknesses correspond to the realization of the designed stress level to accommodate the dimension and load capacity of the fatigue test frame. Three different thicknesses are chosen to investigate the size effect of the specimen cross section on the transformation induced fatigue.

4.4.3. Fatigue test matrix

The first series of experiments correspond to a parametric study investigating the influence of various parameters on the fatigue life and plastic strain accumulation response of the Ni-rich NiTi SMA actuators, as shown in Table 12.

The second series of experiments, conducted by Justin R. Schick in his master's thesis [70], corresponds to the characterization of the influence of surface quality and of the cooling environment on $Ni_{60}Ti_{40}$ SMA actuators after selection of the second heat treatment performed in high vacuum, i.e. V-HT#2, and will be discussed in Section 4.6.

Table 12. Test matrix for $Ni_{60}Ti_{40}$ SMA actuators corresponding to initial parametric study.

Heat Treatment Environment	Aging Time	Specimen Thickness		
Vacuum Heat Treatment	V-HT#1 - 1 hr 450ºC	5 mils (0.127 mm)	10 mils (0.254 mm)	15 mils (0.381 mm)
	V-HT#2 20 hrs 450ºC	5 mils (0.127 mm)	10 mils (0.254 mm)	15 mils (0.381 mm)
Air Heat Treatment	A-HT#2 - 20 hrs 450ºC	5 mils (0.127 mm)	10 mils (0.254 mm)	15 mils (0.381 mm)
Applied Stress Level: 100 MPa – 150 MPa – 200 MPa – 250 MPa				

4.5. Experimental results to parametric study

The main objective for this parametric study is the identification of influences of the selected parameters on the fatigue life of Ni-rich NiTi SMA actuators in terms of number of cycles to failure, applied stress and accumulated plastic strain, which can be extracted from the raw test data plotted in terms of the strain in martensite, strain in austenite and actuation strain versus the number of cycles, as shown for both HT#1 and HT#2 in Figure 54.

The various investigated parameters are analyzed using different criteria. The first set of results identifies the number of cycles to failure of Ni rich SMA actuators as a function of the applied stress and the second of the accumulated plastic strain at failure. Such results provide a macroscopic understanding of the fatigue behavior.

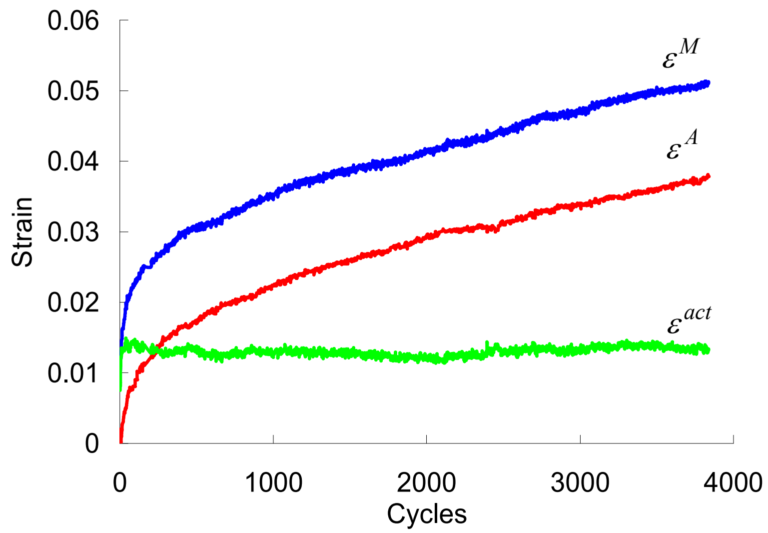

(a)

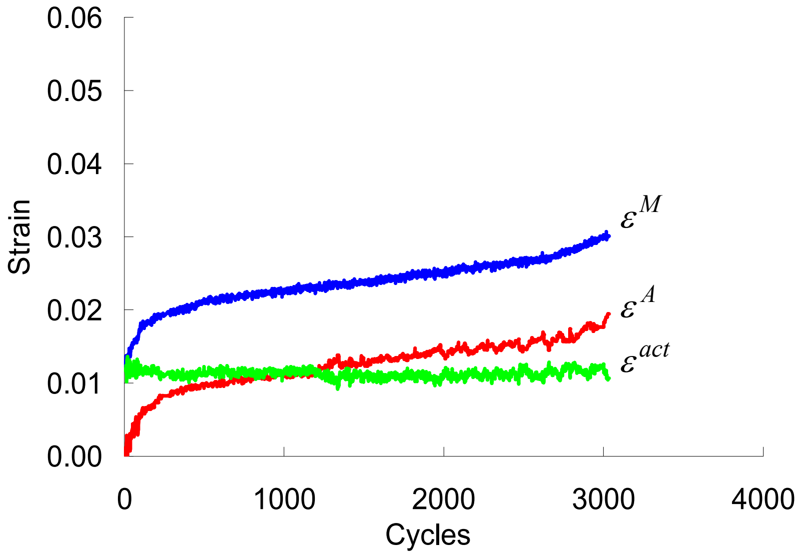

(b)

Figure 54. Representative Fatigue Data: (a) presents results for a 10 mils thick HT#1 specimen under 250 MPa; (b) presents results for a 5 mils thick HT#2 specimen under 250 MPa.

In Figure 55 we compare recoverable strain levels achieved under the various applied constant stress levels. A first series of results was generated under quasi-static loading conditions using a MTS test frame on as received fatigue test specimens (untrained); the second series of results corresponds to values of recoverable strain recorded during the last cycle before failure occurred and are referred to as saturated values. Calibration on MTS test frame (1st cycle - thick trend lines) compared to values recorded at saturation (thin trend lines). Similar trend observed between initial and saturated recoverable strain in both heat treatments. Error bars are added to each saturated data point in Figure 55. They represent variations recorded among multiple samples tested at the same stress level while no bars are reported for the 1st cycle results because of one measurement done at each level.

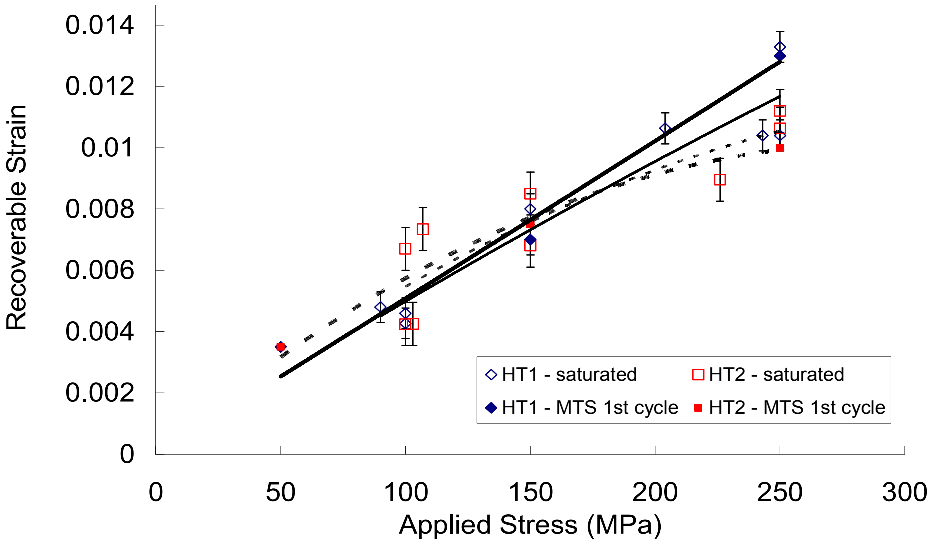

Figure 55. Actuation (recoverable) Strain vs. Applied Stress Level.

4.5.1. Influence of heat treatment time on transformation induced fatigue

One particular property of the nickel-rich $Ni_{60}Ti_{40}$ SMA is that it can exhibit SME without any cold work process. The presence of precipitates favors the storing of elastic energy and therefore the realization of recoverable strains upon martensitic phase transformation. The proportions, the distribution and the composition of the precipitates can be modified and adjusted by applying appropriate heat treatments. The heat treatments consist of a homogenization treatment of one hour at 850°C with furnace controlled cooling to allow formation of precipitates followed by an annealing treatment of either 1 or 20 hours at 450°C.

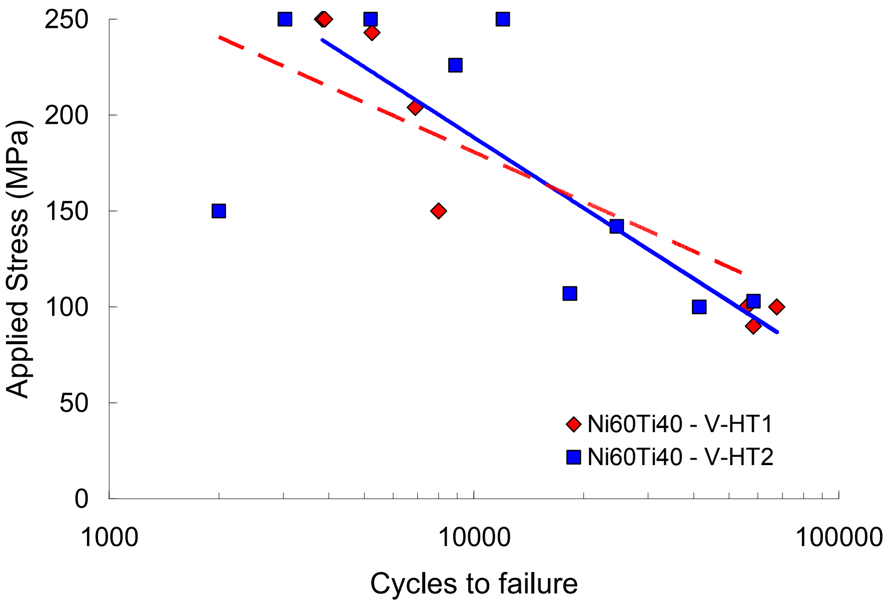

Figure 56. Applied stress level vs. number of cycles to failure for $Ni_{60}Ti_{40}$; comparison between V-HT#1 and V-HT#2.

In this first series of tests, the purpose was to determine if a different aging time had any major influence on the stress life response of the nickel-rich SMA actuators. Fatigue limits of ~ 70,000 cycles were identified for stress levels of ~ 100 MPa and were found to reduce to ~ 4,000 cycles under ~ 250 MPa applied stress. However, the main result from these experiments is that V-HT#1 and V-HT#2 gave the same fatigue life in the stress life space. An additional important result is that no size effect was observed, for both V-HT#1 and V-HT#2. The purpose of the three different thicknesses was to identify any size effect due to the small specimen size and for heat treatment performed in high vacuum, it is shown that no effect is observed.

The results shown in Figure 56 did not demonstrate any differences between V-HT#1 and V-HT#2, however, the values of accumulated plastic strain in terms of applied stress level clearly shows dependence of V-HT#1 on the applied stress level while V-HT#2 does not (Figure 57). V-HT#1 displays plastic strain accumulation values ranging between 1 % and 3.5 % for applied stress levels from 100 MPa to 250 MPa, indicative of an applied stress driven failure. However, the results from V-HT#2 are very different. For the same testing conditions, V-HT#2 does not show any dependence of the accumulated plastic strain on the level of applied stress (Figure 57 and Figure 58).

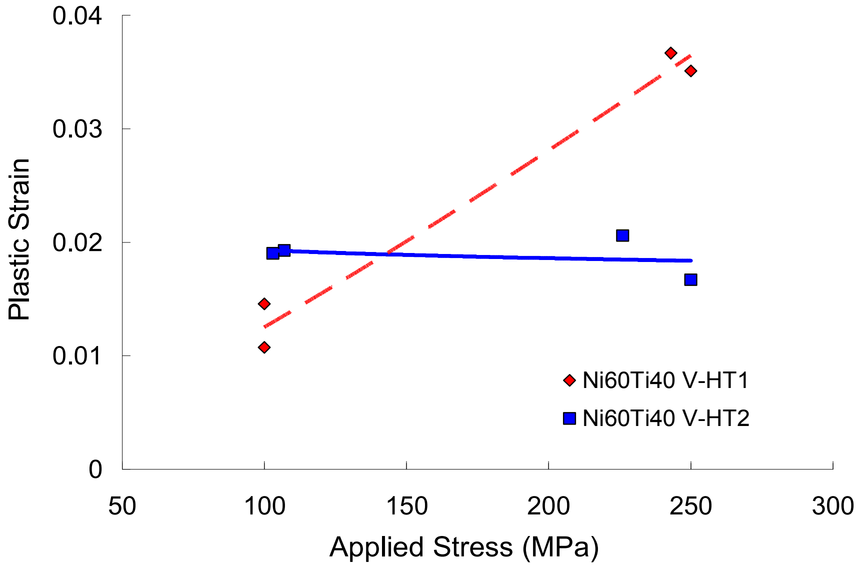

Figure 57. Accumulated plastic strain vs. applied stress level for $Ni_{60}Ti_{40}$: comparison between V-HT#1 and V-HT#2.

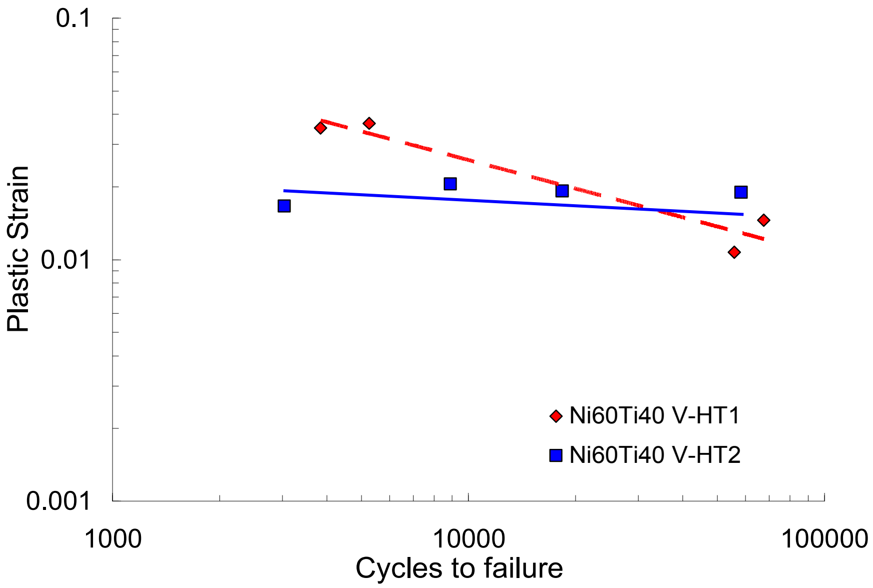

Figure 58. Accumulated plastic strain vs. number of cycles to failure for $Ni_{60}Ti_{40}$: comparison between V-HT#1 and V-HT#2.

A detailed description of the test specimens, the testing conditions and the testing order is given in Table 13 and Table 14. The stress levels are different from the prescribed levels due to recalculation of the recalibration of the applied stress levels due to varying cross sections in the specimens due to specimen cutting uncertainties.

Table 13. Testing sequence and loading conditions for $Ni_{60}Ti_{40}$ vacuum heat treated.

Run order	Specimen #	Heat treatment	Thickness (mils)	Applied stress (MPa)
1	SP# 6	HT#2	10	226
2	SP# 4	HT#2	5	107
3	SP# 3	HT#1	5	204
4	SP# 7	HT#1	15	243
5	SP# 5	HT#2	5	103
6	SP# 5	HT#1	10	90
7	SP# 3	HT#2	15	142
8	SP# 7	HT#2	5	250
9	SP# 2	HT#1	10	250
10	SP# 4	HT#1	15	203
11	SP# 8	HT#1	10	100
12	SP# 9	HT#1	15	100
13	SP# 10	HT#1	5	100
14	SP# 9	HT#2	10	100
15	SP# 10	HT#2	10	250
Heat Treatments		HT#1	1 hr @ 850°C, 1 hr @ 450°C	
		HT#2	1 hr @ 850°C, 20 hrs @ 450°C	

Table 14. Specimens with non-standard test results.

SP# 1 HT#1	Damaged during preliminary testing
SP# 1 HT#2	Damaged during preliminary testing
SP# 2 HT#2	Not applicable for constant stress uniaxial fatigue testing Irregular cross section with major notches
SP# 6 HT#1	MTS tested
SP# 8 HT#2	MTS tested
SP# 5 HT#1	No failure (run out at ~60K cycles)
SP# 5 HT#2	No failure (run out at ~60K cycles)
SP# 4 HT#1	Data Loss (Computer malfunction)

An overview of the results obtained for water jet processed specimens for heat treatment HT#1 and HT#2 is shown in Table 15 and Table 16, respectively. Again, the stress levels are different from the prescribed levels due to recalculation of the recalibration of the applied stress levels due to varying cross sections in the specimens due to specimen cutting uncertainties.

Table 15. Recoverable strain and accumulated plastic strain at half of the specimen life then at the specimen failure for HT#1, arranged according to specimen thickness.

HT#1 - 1 hr @ 850°C, 1 hr @ 450°C							
Specimen number	Thickness (mils)	Applied stress (MPa)	Cycles to failure Nf	Recoverable strain @ 1/2 Nf	Plastic strain @ 1/2 Nf	Recoverable strain @ Nf	Plastic strain @ Nf
3	5	204	6896	0.01073	0.00257	0.01063	0.00685
10	5	100	67571	0.00464	0.00861	0.0046	0.01457
2	10	250	3838	0.01209	0.02585	0.01329	0.03511
5	10	90	57598 (run out)	0.00583	0.01337	0.0048	0.0323
7	15	243	5251	0.0106	0.026	0.0104	0.03667
9	15	100	55811	0.00383	0.00726	0.00427	0.01074
1	Damaged during preliminary testing						
4	Data Loss (computer malfunction)						
6	MTS tested						
8	Data Loss (computer malfunction)						

Table 16. Recoverable Strain and Accumulated Plastic Strain at half of the specimen life then at the specimen failure for HT#2, arranged according to specimen thickness.

HT#2 1 hr @ 850°C, 20 hrs @ 450°C

Specimen number	Thickness (mils)	Applied stress (MPa)	Cycles to failure Nf	Recoverable strain @ 1/2 Nf	Plastic strain @ 1/2 Nf	Recoverable strain @ Nf	Plastic strain @ Nf
4	5	107	18338	0.0067	0.01406	0.00734	0.01926
5	5	103	58341 (run out)	0.00495	0.01676	0.00425	0.01901
7	5	250	3035	0.01123	0.00956	0.01063	0.01669
6	10	226	8897	0.00955	0.01154	0.00895	0.02059
9	10	100	41463	0.00384	0.01581	0.00424	0.02473
10	10	250	creep like behavior - slip in grips				
3	15	142	creep like behavior - slip in grips				
1	Damaged during preliminary testing						
2	Not applicable for constant stress uniaxial fatigue testing - irregular cross section with major notches						
8	MTS tested						

4.5.2. Influence of heat treatment atmosphere on transformation induced fatigue

For the next step of this parametric study, vacuum heat treatment 2 (V-HT#2) is compared to air heat treatment 2 (A-HT#2) for $Ni_{60}Ti_{40}$. Again all specimen sizes are studied in terms of applied stress versus the number of cycles to failure as well as the accumulated plastic strain versus applied stress and versus the number of cycles to failure.

The result is the observation of a major influence on the fatigue life of thin specimens while larger specimens don't seem to be so affected. Also, the existence of a consequential oxide layer formed upon heat treatments performed in air is observed and will be discussed later.

For the first series of specimens heat-treated in high vacuum, the S-N curves didn't show much difference between in the influence of the different thicknesses on the two different heat treatments. However, the presence of an oxide layer caused the thin specimens (0.005 in., 0.127 mm) to fail prematurely while the thick ones sustained similar number of cycles to failure as the ones heat-treated in high vacuum, as seen in Figure 59. Due to the presence of a significant oxide layer, stress correction is necessary to evaluate the actual stress level under which the specimens failed. The results from Figure 59 take this correction into account; for an oxide layer measured to be 0.001 inch (0.0127 mm) thick. Noticeable fatigue life reduction with thin oxidized specimens failing no more than after 2,000 cycles for applied stresses as low as 100 MPa while thick specimens failed around 15,000 cycles, under an applied stress equal to 150 MPa.

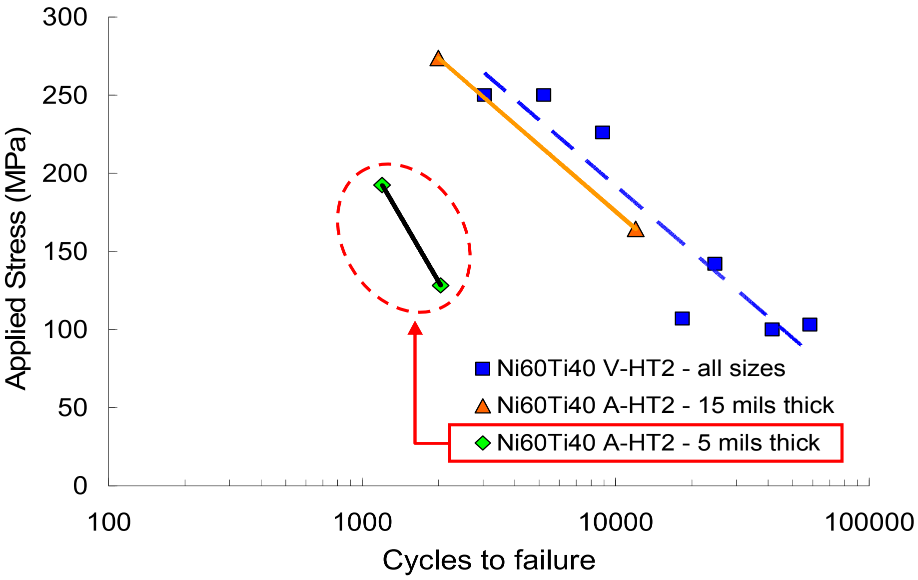

Figure 59. Applied stress level vs. number of cycles to failure for $Ni_{60}Ti_{40}$: comparison between A-HT#2 and V-HT#2.

Figure 60 and Figure 61 compare the previous results for V-HT#2 to the ones obtained for A-HT#2. The results from Figure 60 compare the amount of accumulated plastic strain in terms of the applied stress for A-HT#2 and for V-HT#2 while Figure 61 shows a similar trend of the accumulated plastic strain attained at failure under both heat treatment environments. The only difference was found to be a larger amount of plastic strain for the tests performed on air heat treated specimens.

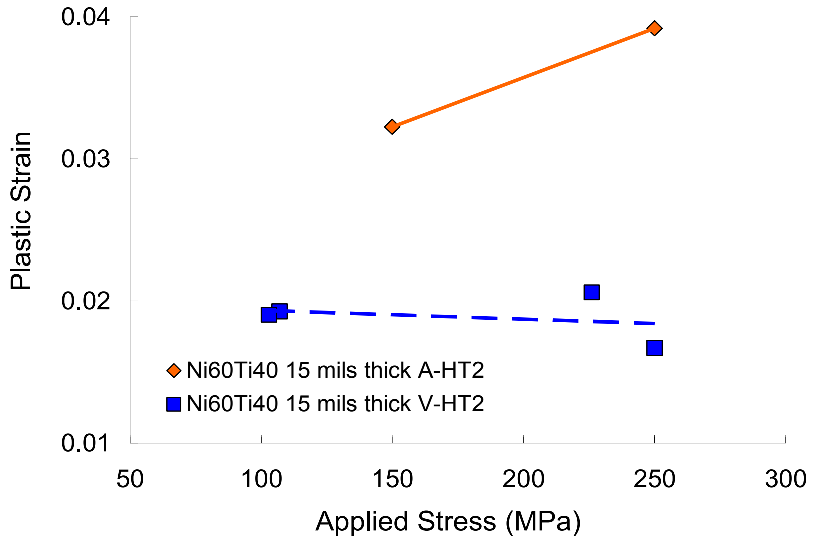

Figure 60. Accumulated plastic strain vs. applied stress level for $Ni_{60}Ti_{40}$ thick specimens: comparison between A-HT#2 and V-HT#2.

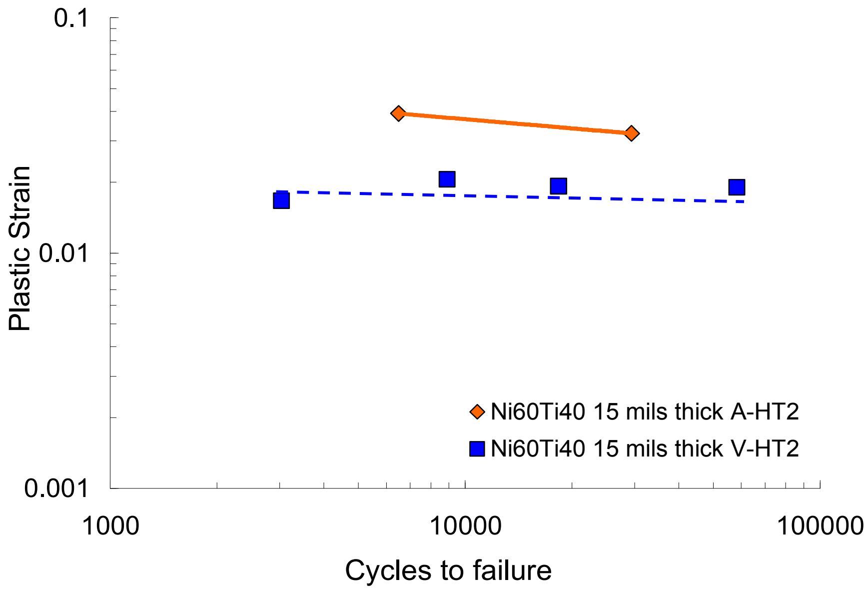

Figure 61. Accumulated plastic strain vs. number of cycles to failure for $Ni_{60}Ti_{40}$ thick specimens: comparison between A-HT#2 and V-HT#2.

Two consecutive series of specimens were processed in two different manners. The first series was water-jet cut to the required dogbone dimensions and heat treated in high vacuum atmosphere while the second series was EDM cut and heat treated in air (Table 9). The result is the observation of a major influence on the fatigue life of thin specimens while larger specimens don't seem to be so affected. Also, the existence of a consequential oxide layer is observed on the fracture surfaces of the failed specimens heat treated in air. A summary of the test specimens, the testing conditions and the testing order is given in Table 17.

Table 17. Testing Sequence and Loading Conditions for 60-NiTi air heat treated.

60-NiTi Air Heat Treated				
Run order	Specimen #	Heat treatment	Thickness (mils)	Applied stress (MPa)
17	EDM SP# 1	HT#1	15	250
18	EDM SP# 4	HT#2	15	250
19*	EDM SP# 2	HT#1	15	150
20*	EDM SP# 5	HT#2	15	150
21	EDM SP# 6	HT#1	5	100
22	EDM SP# 8	HT#2	5	100
23	EDM SP# 7	HT#1	5	150
24	EDM SP# 9	HT#2	5	150

*NOTE: Electrical issues caused a heating problem during the life of the specimens.

An overview of the results for EDM processed specimens for heat treatment HT#1 in air is given in Table 18 and for results for EDM processed specimens for heat treatment HT#2 in air in Table 19.

Table 18. Recoverable Strain and Accumulated Plastic Strain at half of the specimen life then at the specimen failure for HT#1, arranged according to increasing thickness.

HT#1 - 1 hr @ 850°C, 1 hr @ 450°C							
Specimen number	Thickness (mils)	Applied stress (MPa)	Cycles to failure Nf	Recoverable strain @ 1/2 Nf	Plastic strain @ 1/2 Nf	Recoverable strain @ Nf	Plastic strain @ Nf
6	5	100	949	0.01106	0.0043	0.01066	0.00807
7	5	150	1588	0.00855	0.00539	0.00853	0.00803
1	15	250	3899	0.01037	0.04687	0.01042	0.0531
2*	15	150	16104	0.00729	0.01948	0.00137	0.02953

*Electrical issues impacted results.

Table 19. Recoverable Strain and Accumulated Plastic Strain at half of the specimen life then at the specimen failure for HT#2, arranged according to increasing thickness.

HT#2 - 1 hr @ 850°C, 20 hrs @ 450°C							
Specimen number	Thickness (mils)	Applied stress (MPa)	Cycles to failure Nf	Recoverable strain @ 1/2 Nf	Plastic strain @ 1/2 Nf	Recoverable strain @ Nf	Plastic strain @ Nf
8	5	100	2039	0.00491	0.00279	0.00572	0.0037
9	5	150	1917	0.00822	0.00918	0.00767	0.0148
4*	15	250	6492	0.00531	0.03791	0.01186	0.03919
5*	15	150	29399	0.0006	0.03225	0.00471	0.03225

*Electrical issues impacted results.

4.6. Influence of surface quality and cooling environment on transformation induced fatigue

In the previous chapter, fatigue data were obtained for various parameters and decision was made to select the material that was 15 mils thick and that received heat treatment HT#2 in vacuum. From this choice, the goal was to then improve the fatigue life of $Ni_{60}Ti_{40}$ SMA actuators with this particular set of parameters (HT time, HT atmosphere and specimen thickness).

4.6.1. Additional parameters and updated fatigue test matrix

Due to different processing methods (EDM wire cutting, waterjet cutting, heat treatments, etc.), different surface properties were found to have an influence on the fatigue life. Recast layer form upon wire EDM cutting and an oxide layer formed upon heat treatment; therefore all surface layers were removed. Then an ultra-fine surface finish (0.3μm) is applied to eliminate the influence of external factors such as oxide layer/recast layer, microcracks and other surface defects.

The preliminary fatigue data obtained during the parametric study are consolidated with more specimens tested under similar conditions. The recast-layer and HAZ are left on purpose as the actual SMA beam actuator utilized in the VGC application is not polished and is very similar to that of the fatigue test specimens. However, in order to assess the influence of the recast-layer and HAZ on the fatigue response and failure mechanism, a series of specimens are polished for comparison purpose and to isolate the influence of external factors such as the surface quality to limit the analysis to the material's response only. This will be discussed in more details with the failure mechanisms description in the next chapter. The new set of parameters with the selected ones from the previous parametric study is given in Table 20.

Table 20. Test matrix for $Ni_{60}Ti_{40}$ SMA actuators corresponding to emphasized parameters, i.e. cooling environment and surface finish [70].

Initial parameters selection	Parameters under investigation		
	Cooling environment	Surface finish	Applied stress level
Composition $Ni_{60}Ti_{40}$ (wt.%) Aging treatment High vacuum 20 hrs. @ 450°C Specimen thickness 20 mils (508 µm)	Glycol cooling fatigue frame	As-received	100 MPa
			150 MPa
			200 MPa
		Polished (recast-layer/HAZ removed)	100 MPa
			150 MPa
			200 MPa
	Gaseous Nitrogen fatigue frame	Polished (recast-layer/HAZ removed)	100 MPa
			150 MPa
			200 MPa

4.6.2. Removal of recast-layer and heat affected zone due to EDM wire cutting

The hard workability of Ni-rich NiTi SMAs makes them difficult to machine and therefore EDM wire cutting is an appropriate solution to cut SMA sample out of a hot rolled large sheet of $Ni_{60}Ti_{40}$ SMA. Waterjet cutting was also an option, however, the required tolerance and small specimen geometry made the latter solution unreliable. Therefore all specimens were EDM wire cut into the flat dogbones previously described in the chapter.

The EDM wire cutting process is highly efficient and provides excellent maintain of geometric specifications. It is a process that permits to cut specimens to very complex geometry that regular turning and milling wouldn't compare to, but it presents a major inconvenient. The fact that cutting is achieved through local and very fast melting of the material results in the formation of a thin layer that can reach a depth of approximately 1 mil (~ 25 μm) in the worst case [71]. This layer is called recast-layer and is by nature of the same composition of the precut SMA but such drastic melting and solidification results in a totally different microstructure and therefore, response. The extreme cooling rates due to very small melted volumes are in the order of 10^6 °C/s. such high cooling conditions result in hardening and yield limit increase of the recast layer, making the surface of the material hard and brittle (hardness of recast-layer ~ 1000 HV while hardness of unaffected SMA is approximately around 300 HV.

Not only the recast-layer is detrimental, but also due to the temperature gradients resulting from the fast and high temperature melting, a heat affected zone (HAZ) is induced. In this region of the SMA, the alloy was not melted but severely heat treated; this layer can measure up to 1.4 mils (~ 35 μm). The overall result from performing EDM wire cutting is the formation of a detrimental region that can reach a depth of 2.5 mils (~ 60 μm).

In this work, a safety margin is taken and the removal of the recast-layer and of the HAZ is extended to a 4 mils (~ 100 μm) depth to insure fully unaffected Ni-rich dogbone specimens. A polishing procedure was defined in order to provide a near stress-free mechanical polishing of the fatigue specimens. The polishing procedure can be found in details in the work of Justin R. Schick in his Master's thesis [70].

The removal of the recast-layer/HAZ was performed using automated mechanical polishing at very low force to minimize the formation of residual stresses in the surface of the polished specimens. The polishing consists of grinding off the damaged layer and finishes with an ultra-fine polish, i.e. 0.1μm. Figure 62(a) show the surface quality of the as-received specimens, Figure 62(b) the intermediate removal of the recast-layer with deeper recast pits and the remaining HAZ, and Figure 62(c) the final result after full grinding and mirror polish. A detail of the corner radius and of the unpolished area showing oxide layer, recast-layer and HAZ is shown in Figure 63.

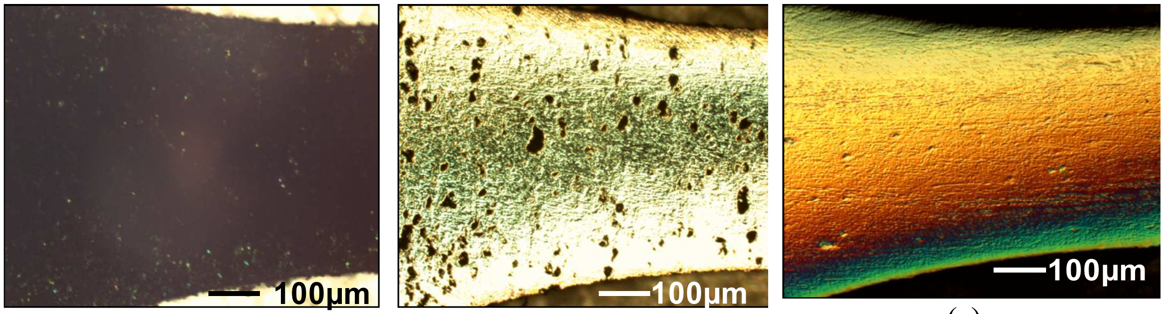

(a) (b) (c)

Figure 62. Optical micrographs showing the removal of the recast-layer/HAZ down to a polish of 0.3µm roughness with detail of (a) recast-layer, (b) partially removed recast-layer and (c) final polish [70].

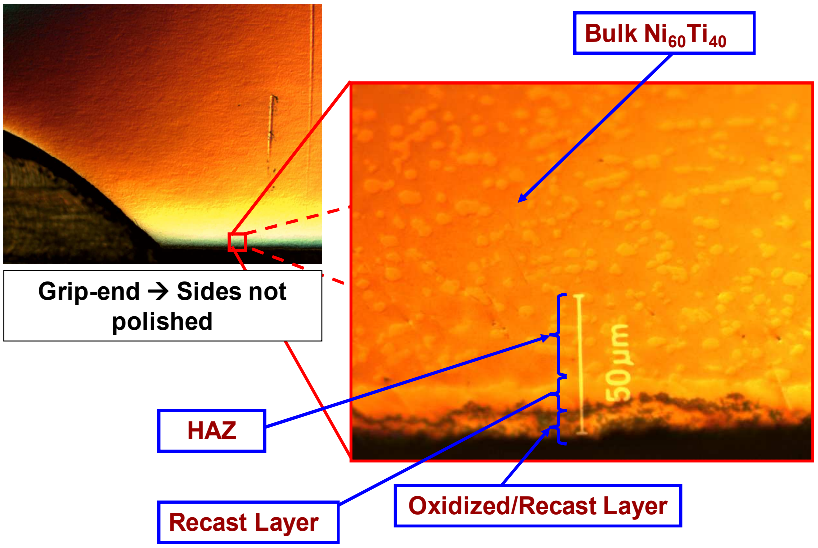

Figure 63. Optical micrographs showing the corner radius of a polished specimen; the grip-ends are not polished on the sides and the nature and morphology of the side recast-layer is visible and found in agreement with previous observations [70].

4.6.3. Influence of environment and surface quality on transformation induced fatigue

The results from the constant stress fatigue testing of the $Ni_{60}Ti_{40}$ specimens in corrosive and corrosion-free environments for as-received and polished surface quality are presented in Figure 64.

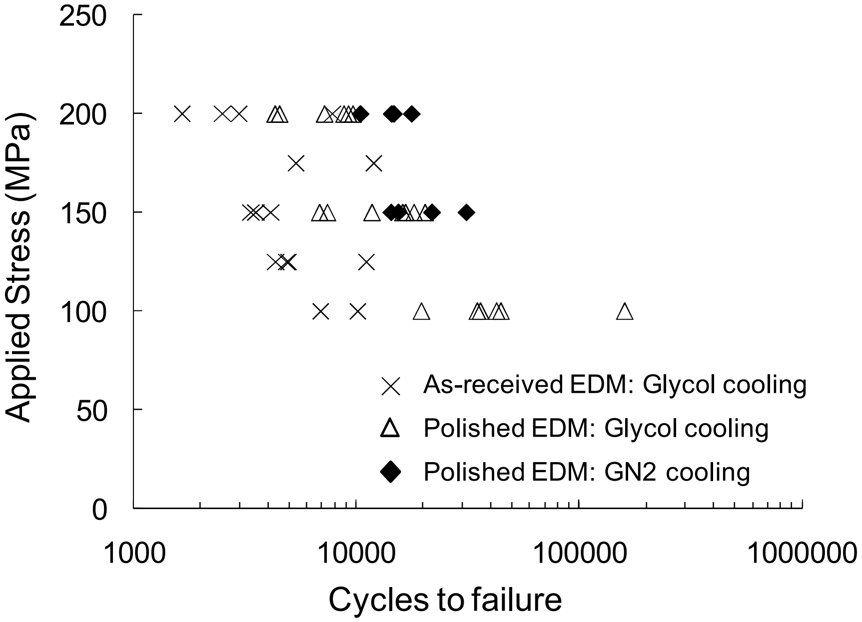

Figure 64. Constant stress fatigue results for $Ni_{60}Ti_{40}$ under as-received and polished conditions, tested with glycol coolant or with GN2 coolant.

The first important result is the consistent improvement of fatigue life from corrosive conditions on the as-received specimens, corrosive conditions on the polished specimens and finally to the corrosion-free testing on the polished specimens. The corrosive environment on as-received specimens gives fatigue limits ranging between 2,000 and 4,000 cycles under 200 MPa up to fatigue limits between 7,000 and 10,000 cycles under 100 MPa. The corrosive environment on polished specimens gives fatigue limits ranging between 5,000 and 15,000 cycles under 200 MPa up to fatigue limits comprised between 22,000 and 160,000 cycles under 100 MPa, which shows a significant improvement of the fatigue limits, and especially under low applied stress levels. It appears that the surface quality plays an even more important role under lower stress levels, where damage accumulates at a slower rate and therefore and results in failure initiation at much larger number of cycles to failure. Another explanation underlies with the presence of Ni-rich precipitates that play a major role in the damage initiation and formation in Ni-rich NiTi SMA actuators. The microstructural aspects of the damage initiation and propagation will be discussed in detail in Chapter V.

The second important result refers to the use of polished fatigue specimens in a corrosion-free cooling environment. Due to Nitrogen storage and feeding management, the fatigue testing in this last series of tests was performed for 200 MPa and 150 MPa stress levels only [70]. While data for the 100 MPa stress level would have been highly valuable for comparison purposes, the improvement of the fatigue life from the corrosive to corrosion-free environment for the polished fatigue specimens tested under 200 MPa goes from between 5,000 and 15,000 cycles to between 15,000 and 25,000 cycles. This result indicates that the surface of the fatigue specimens drives damage and failure initiation.

A common result to all fatigue testing conditions is the observation of a dispersion of the data, which was observed for both TiNiCu SMA wire actuators fatigue results in Chapter II as well as for the $Ni_{60}Ti_{40}$ dogbone specimens in the previous parametric study. The data dispersion is even more visible when comparing the accumulated plastic strain values reached at failure with respect to the number of cycles to failure, as shown in Figure 65. The important observation in this result is the absence of real possible criterion based on accumulated plastic strain. The data spread between 0.7% and 5% plastic strain for fatigue limits ranging between about 2,000 cycles up to more than 100,000 cycles. In opposition to non-precipitated SMA compositions, such as the equiatomic $Ni_{55}Ti_{45}$ (wt.%) or TiNiCu SMAs from Chapter II, the presence of precipitates seems to impede the plastic strain to saturate consistently, resulting in a wide range of plastic strain values measured at failure.

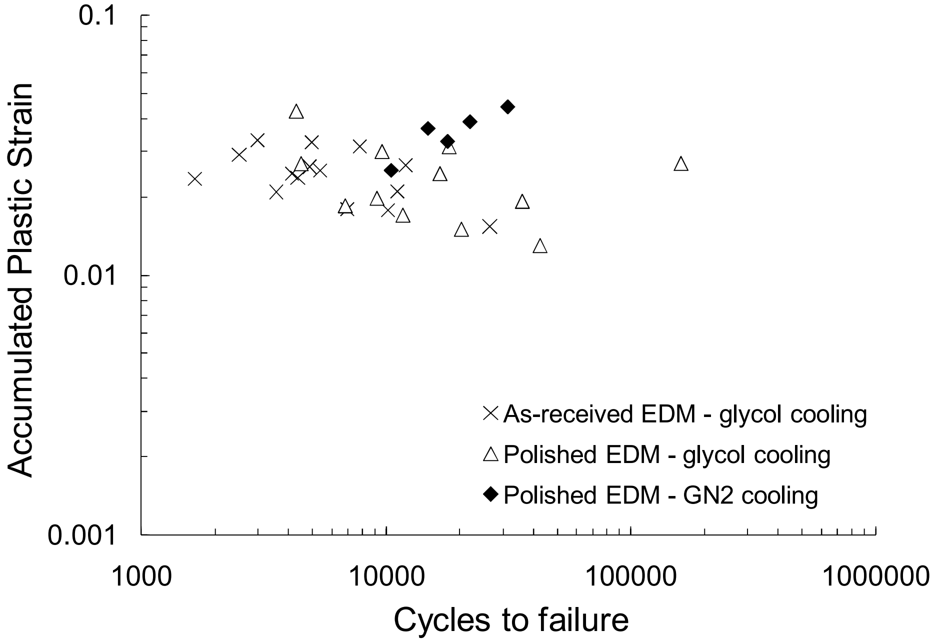

Figure 65. Accumulated plastic strain versus number of cycles to failure for unpolished specimens tested in glycol and polished specimens tested in glycol and gaseous Nitrogen.

CHAPTER V

CHARACTERIZATION AND FAILURE MECHANISMS OF THE TRANSFORMATION INDUCED FATIGUE OF Ni-RICH NiTi SMA ACTUATORS

Chapter V focuses on the characterization and the understanding of the failure mechanisms dictating transformation induced fatigue in Ni-rich NiTi SMA actuators. In Chapter IV, experimental investigations were carried out to study the impact of several parameters and their influence on the fatigue response of $\mathrm{Ni_{60}Ti_{40}}$ SMA actuators. the novel aspect of such Ni-rich NiTi SMA is that through precipitation [5, 45, 48], enhanced hardening and cyclic stability is achieved and therefore the evolution of the microstructure plays a significant role in the understanding of the material's cyclic response [5, 9, 15, 45, 47, 48, 49]. In this Chapter, the investigations are based on the understanding of the nature, the role and influence of the Ni-rich precipitates on damage formation upon cyclic loading. Pre-fatigue characterization is performed to assess the microstructure of the material prior to cyclic loading and conclusions are drawn from results obtained after measurement of the evolution of the transformation temperatures, of the mechanical properties and of the present phases using differential scanning calorimetric measurement, nanoindentation and X-ray diffraction techniques. The identification of a precipitation driven fatigue failure mechanism due to significant NiTi matrix/Ni-rich precipitates interactions concludes the chapter upon observation and discussion of a series of fractography performed on failed fatigue test specimens.

5.1. Precipitation characterization

5.1.1. Precipitation sequence

In order to understand the damage and failure mechanisms in $Ni_{60}Ti_{40}$ SMA actuators, it is necessary to investigate what influence the heat treatments have on the microstructure of the material and on the formation of Ni-rich precipitates in the NiTi matrix.

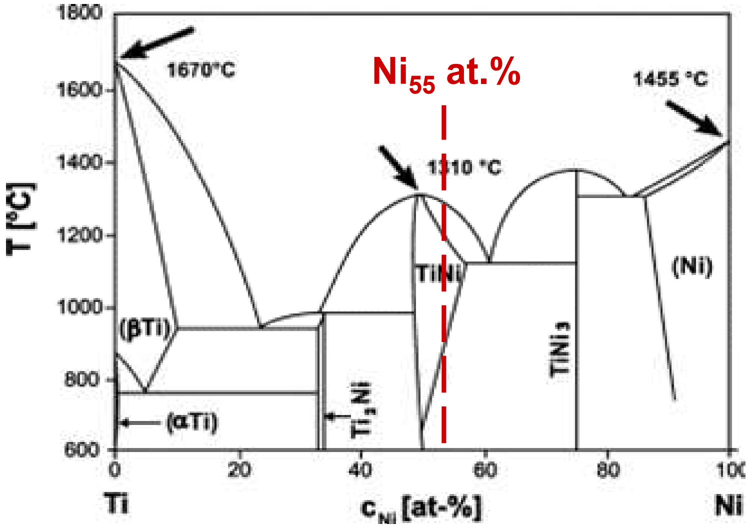

Figure 66. Binary phase diagram for NiTi [9, 53].

Figure 66 is the binary phase diagram for the NiTi system where 60 weight percents of Nickel corresponds to 55 atomic percent of Nickel. The location of the 55 atomic percent dash line indicates that upon cooling from the melt, the alloy presents two phases in equilibrium below a temperature approximately equal to 1000°C, namely NiTi and Ni_3Ti. As it was introduced earlier, the history of the alloy processing is not known until the 900°C hot rolling process, which indicates that deformation and texturing was induced at temperatures where NiTi and Ni_3Ti are in equilibrium, resulting in formation of a biphasic material. The homogenization treatment performed then at 850°C during 1 hour followed by a furnace controlled cooling in 12 hours allows relaxation of any texturing, residual stresses as well as diffusion equilibrium of Nickel between the NiTi matrix and Ni-rich precipitates [5, 50, 72]. For the material had been water quenched, the microstructure would have been made of solely NiTi and Ni_3Ti precipitates, but the slow cooling resulted in the formation of intermediate phases such as Ni_3Ti_2 and Ni_4Ti_3 precipitates [47, 51]. It has been reported that three temperature ranges correspond to three different equilibriums, which are also time dependent. The equilibriums corresponding to the three temperature ranges are given in Table 21, with α_0 corresponding to the highest Nickel concentration in the NiTi matrix and α_5 to the least Nickel concentration. These precipitation sequences allow identifying the different precipitates that may form upon the different heat treatments undergone by $Ni_{60}Ti_{40}$ SMA actuators.

Table 21. Equilibrium evolution from the supersaturated NiTi matrix α_0 to the growth of metastable Ni-rich precipitates, i.e. $\mathrm{Ni_4Ti_3}$ and $\mathrm{Ni_3Ti_2}$, and finally to the growth of stable Ni-rich precipitates, i.e. $\mathrm{Ni_3Ti}$ [47].

Precipitation sequence	Temperature range
$\alpha_0 \rightarrow \alpha_1 + \mathrm{Ni_3Ti}$	$780 \pm 10°\mathrm{C} \le \mathrm{T} \le 1010 \pm 10°\mathrm{C}$
$\alpha_0 \rightarrow \alpha'_1 + \mathrm{Ni_3Ti_2}$ $\alpha'_1 + \mathrm{Ni_3Ti_2} \rightarrow \alpha'_2 + \mathrm{Ni_3Ti_2} + \mathrm{Ni_3Ti}$ $\alpha'_2 + \mathrm{Ni_3Ti_2} + \mathrm{Ni_3Ti} \rightarrow \alpha'_3 + \mathrm{Ni_3Ti}$	$690 \pm 10°\mathrm{C} \le \mathrm{T} \le 780 \pm 10°\mathrm{C}$
$\alpha_0 \rightarrow \alpha''_1 + \mathrm{Ni_4Ti_3}$ $\alpha''_1 + \mathrm{Ni_4Ti_3} \rightarrow \alpha''_2 + \mathrm{Ni_4Ti_3} + \mathrm{Ni_3Ti_2}$ $\alpha''_2 + \mathrm{Ni_4Ti_3} + \mathrm{Ni_3Ti_2} \rightarrow \alpha''_3 + \mathrm{Ni_3Ti_2}$ $\alpha''_3 + \mathrm{Ni_3Ti_2} \rightarrow \alpha''_4 + \mathrm{Ni_3Ti_2} + \mathrm{Ni_3Ti}$ $\alpha''_4 + \mathrm{Ni_3Ti_2} + \mathrm{Ni_3Ti} \rightarrow \alpha''_5 + \mathrm{Ni_3Ti}$	$450 \pm 10°\mathrm{C} \le \mathrm{T} \le 690 \pm 10°\mathrm{C}$

5.1.2. Precipitation, cycling and transformation temperatures

From the previous observations, the microstructure of the $\mathrm{Ni_{60}Ti_{40}}$ SMA fatigue test specimens shows a consequential amount of precipitates. The precipitates seem therefore to have a multifunctional nature in these alloys such as generating local coherent/non-coherent stress fields responsible for elastic strain energy storage, as well as Nickel sinks allowing adjusting local composition and therefore transformation behavior (temperature, hardening and hysteresis).

Equiatomic NiTi SMAs have dislocation based stabilization and damage mechanisms. Therefore, evolution of the microstructure is dominated by the accumulation of plastic deformations through formation of dislocation under repeated martensitic transformation subject to stress. Transformation induced fatigue results exhibit a very large discrepancy in number of cycles to failure; from a few 1,000 cycles to almost 100,000 cycles under similar applied stress level, as shown in Figure 67. Therefore, additional investigations are needed to understand the physical reasons of such dispersion and to be able to reduce such discrepancy range for future application purpose. Based on the fatigue test results shown in Table 16, Table 19 and Figure 64, a selection of test specimens was done accordingly to increasing number of cycles to failure. The DSC coupons were cut to approximately 10 mg and were heated/cooled at a rate of 5°C/min. Figure 67 shows a selection of fatigued specimens summarized in Table 22

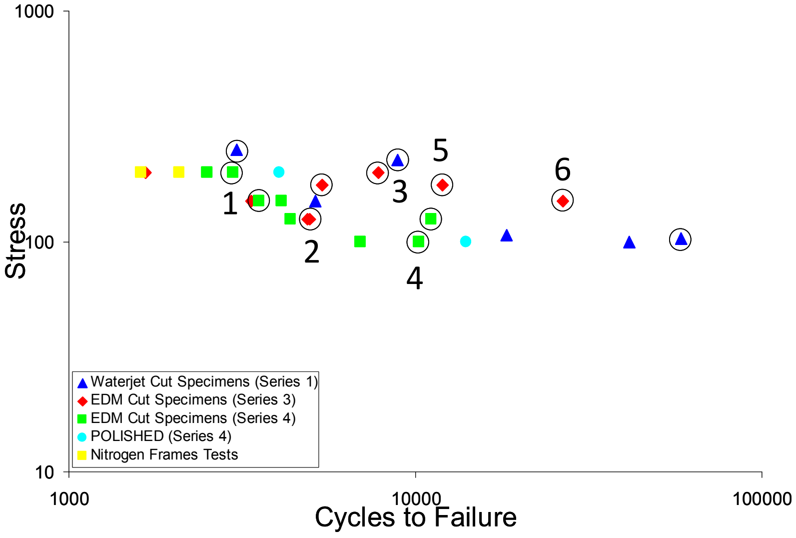

Fig

Figure 67. Stress – Cycles to failure for HT#2 and selected samples for DSC characterization.

Table 22. Identification of selected $Ni_{60}Ti_{40}$ fatigued specimens for DSC post failure characterization.

Load Level (MPa)	Number of Specimens
100	• 2 – AHT#2, EDM, 0.015 in. • 1 – VHT#2, Waterjet, 0.05 in. • 1 – VHT#2, EDM, 0.02 in.
125	• 1 – VHT#2, EDM, 0.015 in. • 1 – VHT#2, EDM, 0.02 in.
150	• 1 – VHT#2, EDM, 0.015 in. • 1 – VHT#2, EDM, 0.02 in.
175	• 2 – VHT#2, EDM, 0.015 in.
200	• 1 – VHT#2, EDM, 0.015 in. • 1 – VHT#2, EDM, 0.02 in.
250	• 2 – AHT#2, EDM, 0.015 in. • 1 – VHT#2, Waterjet, 0.01 in. (226 MPa) • 1 – VHT#2, Waterjet, 0.005 in.

The DSC results are shown for the 2nd heating/cooling cycle to assess any subsequent evolution of transformation temperatures due to internal stresses or retained martensite. The results are shown for the 2nd heating cycle and for the 2nd cooling cycle in Figure 68 and Figure 69, respectively.

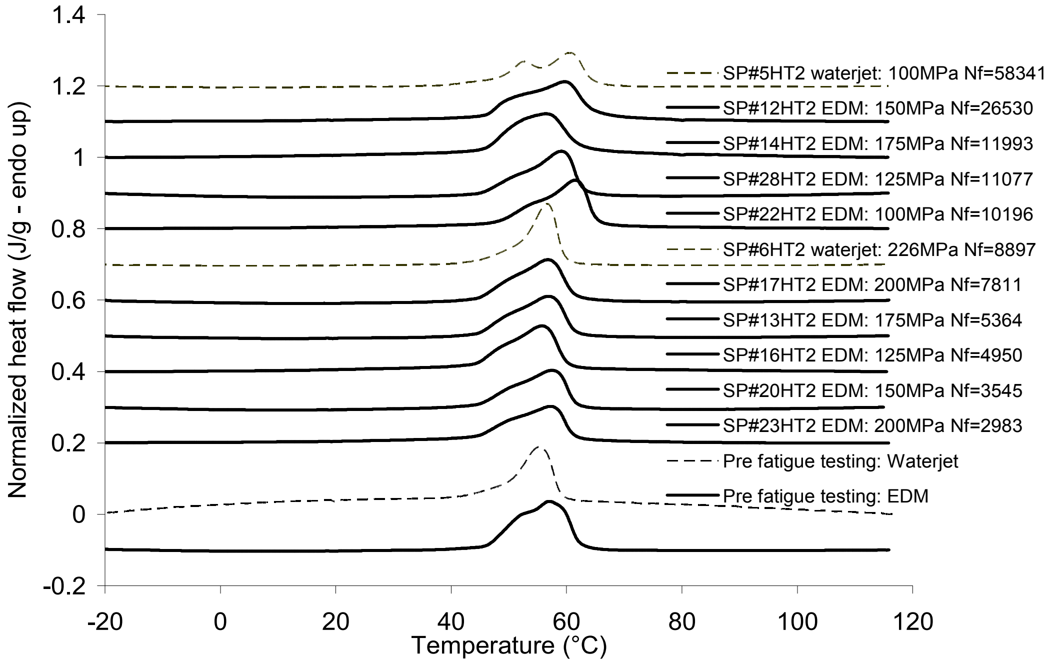

Figure 68. Pre/Post fatigue testing DSC results for martensite to austenite transformation.

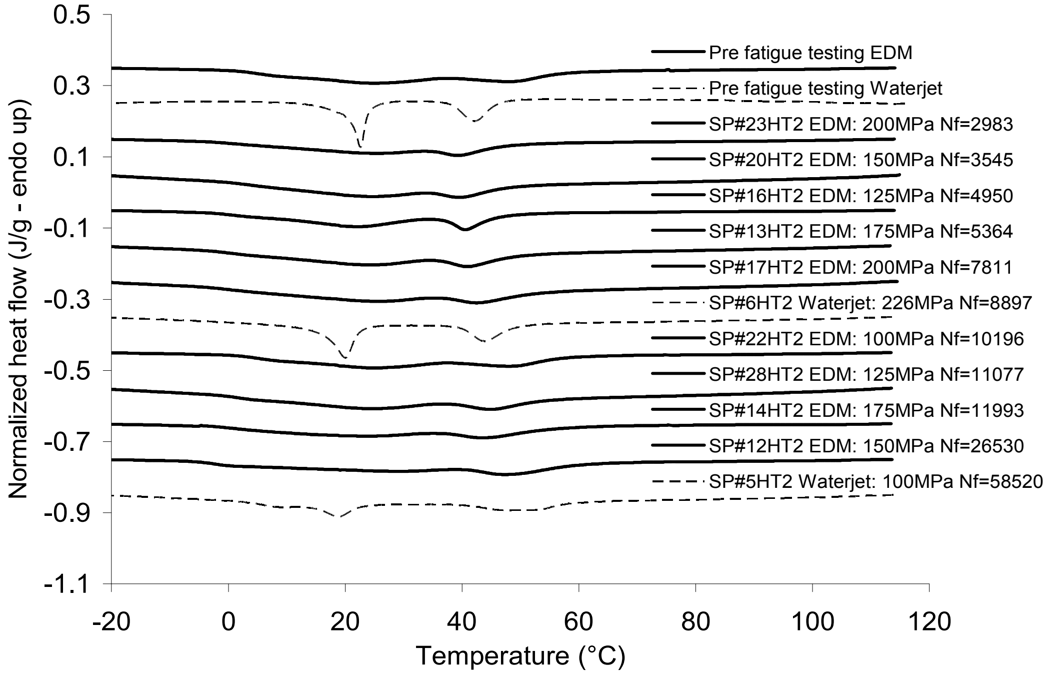

Figure 69. Pre/Post fatigue testing DSC results for austenite to martensite transformation.

The first result that can be concluded is that the stabilization/training results in the flattening of the DSC curves, indicating that dislocations have developed and stabilized the SME in the material [5, 46, 47]. The precipitates, first reason for the martensitic transformation in the Ni-rich NiTi SMAs, are driving the phase transformation and therefore are driving the transformation temperatures. The dislocations are contributing to the stabilization of the transformation and therefore to the shift in transformation temperatures [45, 47]. Due to the presence and dominant nature of the precipitates, the transformation temperatures are not shifting as much as they would be expected if the actuators were made of equiatomic NiTi SMA.

5.1.3. Characterization of the NiTi matrix and Ni-rich precipitates by X-ray diffraction

After investigating the chemical composition of the different phases observed in the $Ni_{60}Ti_{40}$ SMA, the nature of the phases (NiTi matrix and Ni-rich precipitates) requires confirmation. To do so, polished pre-fatigue test specimens are analyzed using X-ray diffraction techniques. The measurements are performed at room temperature as well as at high temperature, to investigate both martensite and austenite coexisting with Ni-rich precipitates.

Figure 70 is the result for the room temperature XRD scan. The two main results are the coexistence of martensite (also known as B19' phase [53]) with the Ni-rich precipitates, as expected, but also the confirmation of the precipitates compositions, i.e. Ni_3Ti and Ni_4Ti_3. The binary phase diagram was predicting approximately 20% Ni_3Ti

precipitates, which is qualitatively observed in the peaks relative intensity. The martensite is self accommodated with low symmetry, therefore many variants, resulting in normalized lower peak intensity. Figure 71 shows the results for 100°C XRD scan. The result presents the austenite (also known as B2 parent phase [53]) coexisting with Ni_3Ti and Ni_4Ti_3 precipitates. In this result, the normalized peak intensity are larger for the NiTi matrix, this can be explained by the high symmetry of the austenite diffracting with much more intensity than the self-accommodated martensite.

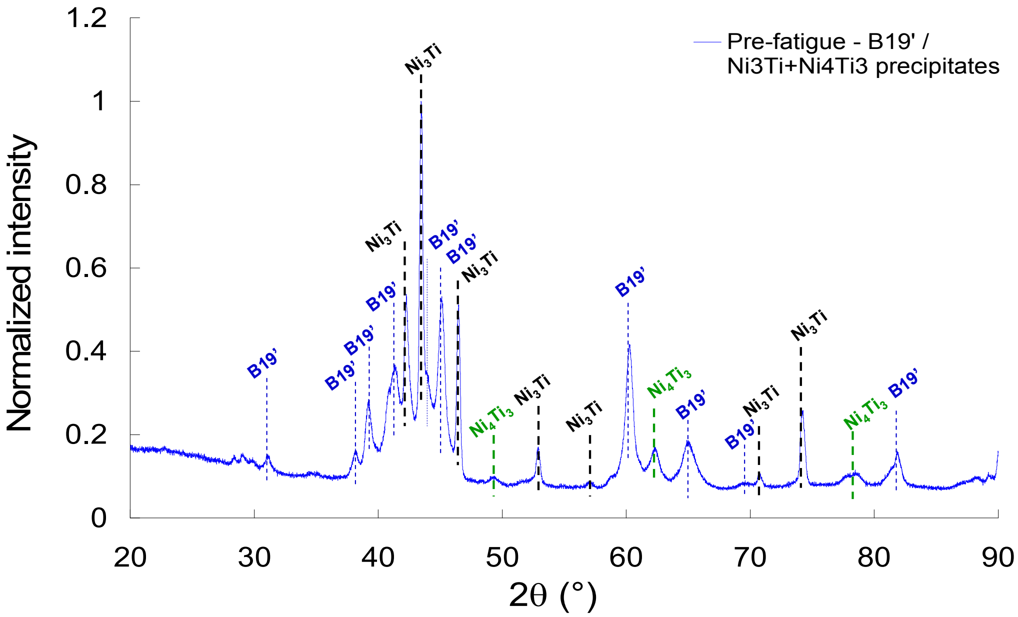

Figure 70. Room temperature XRD result of fatigue $Ni_{60}Ti_{40}$ specimens; identification of martensite B19', Ni_3Ti and Ni_4Ti_3 precipitates.

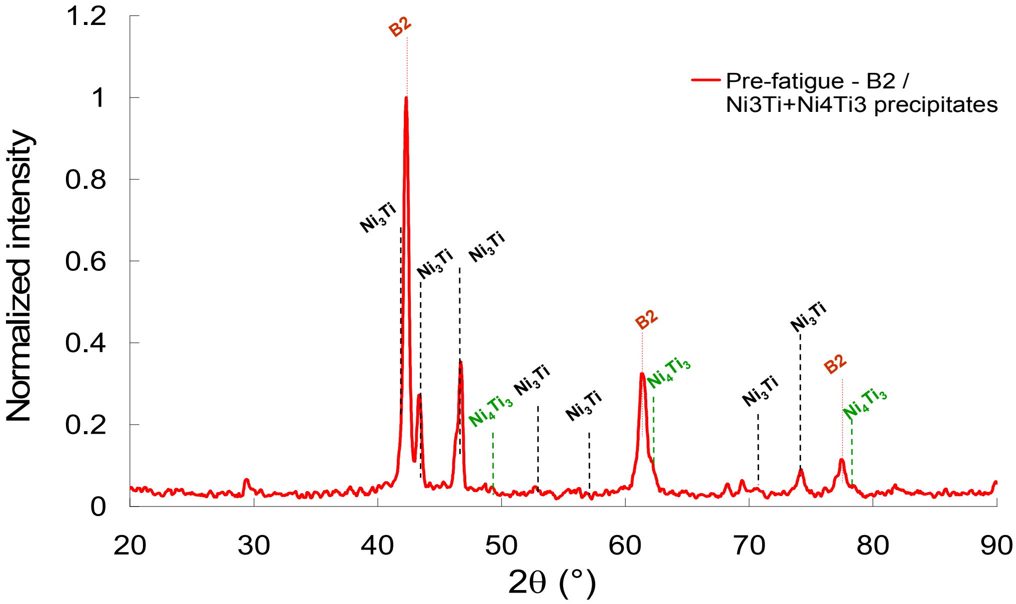

Figure 71. 100°C XRD result of fatigue $Ni_{60}Ti_{40}$ specimens; identification of austenite B2, Ni_3Ti and Ni_4Ti_3 precipitates.

5.1.4. Characterization of the NiTi matrix and Ni-rich precipitates by nanoindentation

After the analysis of the precipitates, the mechanical properties and interactions of the NiTi matrix with the Ni_3Ti precipitates became of interest, in the optic of understanding the influence of the presence of stable, non-phase changing precipitates, in a phase changing material. The Ni_3Ti precipitates, as large as 5 µm, present a morphology that makes nanoindentation ideal to study the mechanical properties and interactions between NiTi matrix and Ni_3Ti precipitates. To do so, two specimens are selected, one polished pre-fatigue testing and one post fatigue failure. The results are shown in Figure 72 and Figure 73.

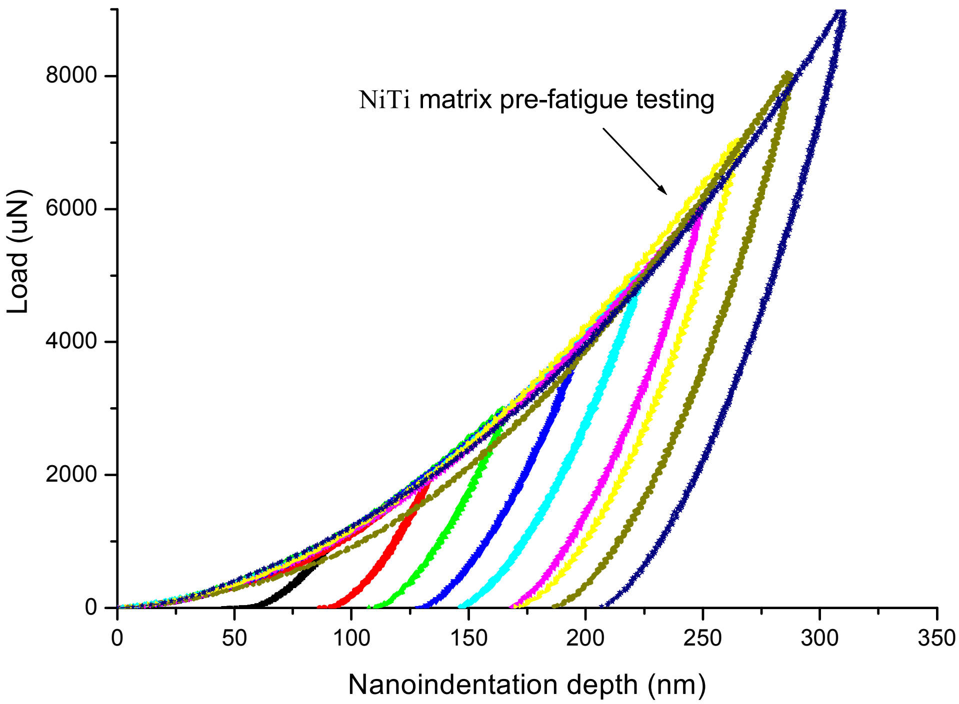

Figure 72. Load-depth nanoindentation profiles for increasing load in the NiTi matrix pre fatigue testing.

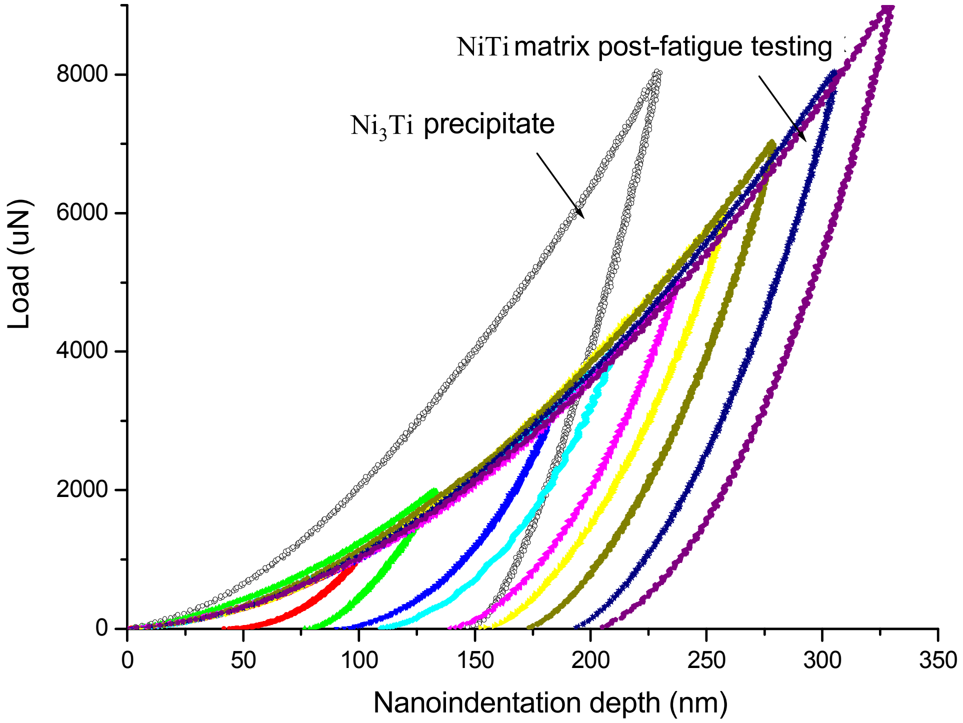

Figure 73. Load-depth nanoindentation profiles for increasing load in the NiTi matrix post fatigue failure compared to Ni_3Ti precipitate response.

A representative result of Figure 72 and Figure 73 is given in the next result. Figure 74 first shows how cyclic loading affects the load-depth response of the NiTi matrix but also how much stiffer the Ni_3Ti precipitates are compared to the NiTi matrix. The stiffness was measured to be approximately equal to 85 GPa in the pre fatigue matrix and approximately equal to 75 GPa in the case of the post fatigue matrix, as shown in Figure 75. A possible explanation for the slight reduction in elastic modulus as well as hardness seems to be the transformation temperatures and the phase in which nanoindentation was performed. It was done under room temperature conditions, i.e. in a region where R-phase finished transforming and where martensite (B19’) started. The results from Figure 68 and Figure 69 show how upon cooling the austenite (B2 parent phase) makes room temperature a region where the end of the R-phase and the beginning of the martensite (B19') transformation are concomitant. It was found that cyclic loading does affect transformation temperatures in the sense that they remain very stable; the one influence that seems significant in this analysis of mechanical properties using nanoindentation is the broadening of the transformation peaks, which means wider transformation regions and therefore different mechanical response at room temperature. The same analysis can be done with the evolution of the nanohardness between the pre and post fatigued specimen, as shown in Figure 76.

The other important result deals with the presence of Ni_3Ti precipitates. The measurement of the Ni_3Ti elastic modulus shows values twice as large as the one measured for the NiTi matrix, at low nanoindentation depths. However, deeper nanoindentation results in the reduction of the elastic modulus of the precipitates and leads to its convergence of towards NiTi matrix values, as seen in Figure 75. This indicates that the more the precipitate is indented, the more the response is a combined effect of the precipitate and of the NiTi matrix. Similar results and arguments can be made looking at the nanohardness of the precipitates at varying nanoindentation depths.

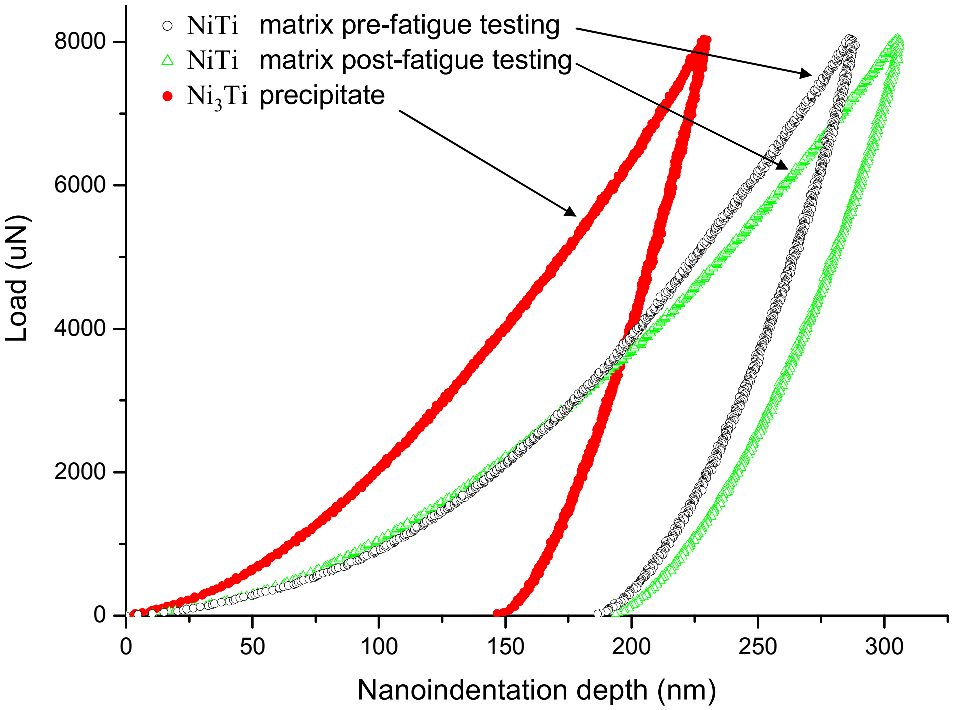

Figure 74. Nanoindentation profiles for polished specimen, before and after fatigue testing; with load-depth response for (a) Ni_3Ti precipitates, (b) NiTi matrix before fatigue and (c) NiTi matrix post fatigue failure.

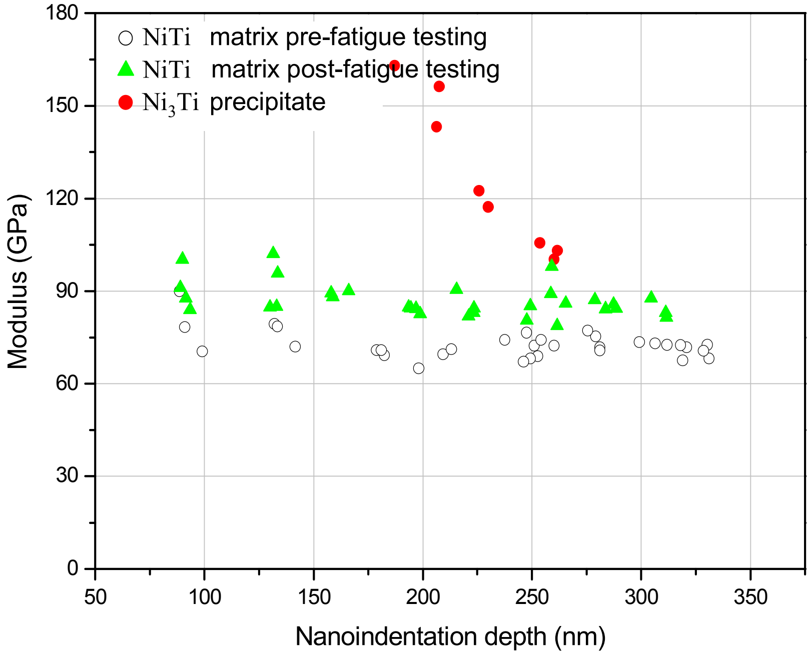

Figure 75. Elastic modulus for the pre fatigue and post fatigue specimens compared to the elastic modulus of the Ni_3Ti precipitates, measured for increasing nanoindentation depth.

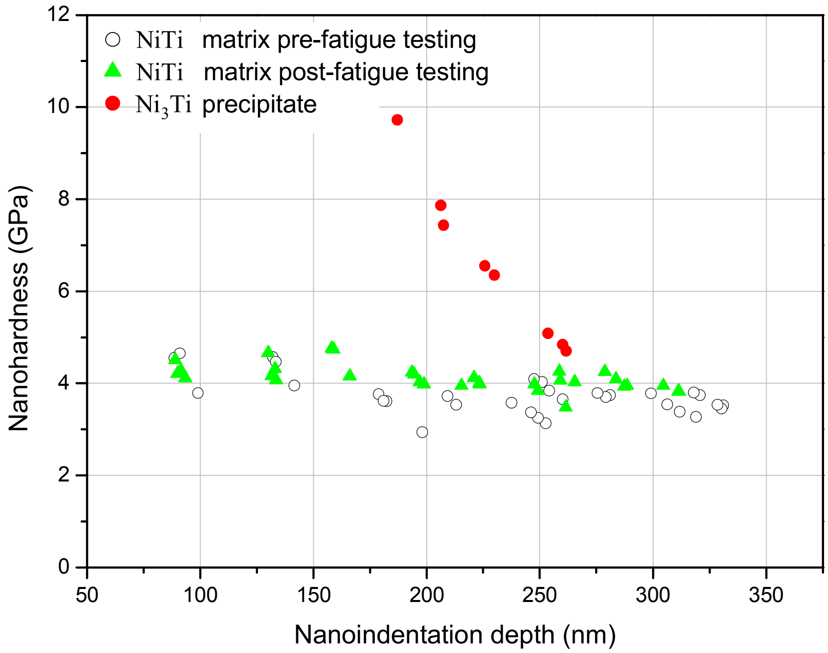

Figure 76. Nanohardness for the pre fatigue and post fatigue specimens compared to the elastic modulus of the Ni_3Ti precipitates, measured for increasing nanoindentation depth.

5.2. Pre-fatigue testing microstructure

5.2.1. Shape-set treatment

In this work, the starting heat treatment is a shape set treatment performed at 850°C during one hour and furnace cooled for 12 hours. Therefore, from the NiTi binary phase diagram in Figure 66, the Nickel from the high Nickel content NiTi matrix diffuses and contributes to the formation of Ni_3Ti precipitates. The use of electronic microscopy combined with EDS chemical element analysis allows the determination of the matrix and observed precipitate compositions.

Figure 77 is an SEM micrograph showing the polished surface of the post shape set treatment of a $Ni_{60}Ti_{40}$ SMA actuator. The first observation is the identification of white bulky phases which are measured to be Ni_3Ti precipitates, as shown in detail in the EDS measurement results from Figure 78 and Figure 79. The Nickel content of Ni_3Ti precipitates resulting from measurements is ranging between 75 at.% and 79 at.% which is very close to what was expected from simple lever rule performed on the binary phase diagram [9, 53]. The other important result is the observation of needle-like precipitates as seen in Figure 77. The measurement of the chemical composition leads to the identification of Ni_4Ti_3 and Ni_3Ti_2 precipitates from the results shown in Figure 78 and Figure 79.

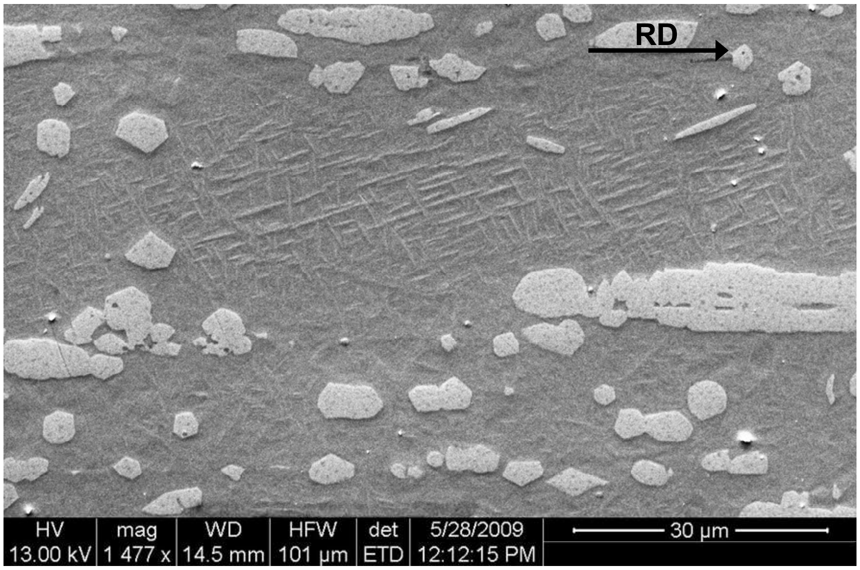

Figure 77. SEM micrograph of polished $Ni_{60}Ti_{40}$ SMA after shape set showing the rolling direction; overview of the different phases present after furnace controlled cooling.

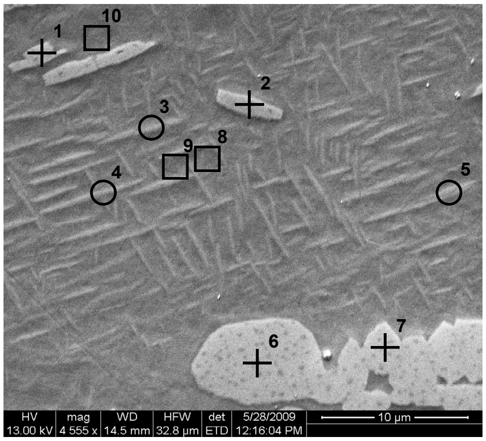

(a)

□ $Ni_{60}Ti_{40}$ matrix

+ Ni_3Ti precipitates

○ Ni_4Ti_3/ Ni_3Ti_2 Precipitates

(b)

Position	**Ni wt.% (at.%)**	**Ti wt.% (at.%)**
1	**81.75 (78.52)**	**18.25 (21.48)**
2	**81.71 (78.47)**	**18.29 (21.53)**
3	**61.42 (56.50)**	**38.58 (43.50)**
4	**62.80 (57.94)**	**37.20 (42.06)**
5	**62.83 (57.97)**	**37.17 (42.03)**
6	**82.25 (79.08)**	**17.75 (20.92)**
7	**82.38 (79.23)**	**17.62 (20.77)**
8	**64.63 (59.85)**	**35.37 (40.15)**
9	**61.90 (57.00)**	**38.10 (43.00)**
10	**62.46 (57.58)**	**37.54 (42.42)**

(c)

Figure 78. First site of observation and measurement: SEM EDS analysis of the surface of $Ni_{60}Ti_{40}$ SMA actuators after shape set treatment; (a) area of interest showing the different phases: NiTi matrix, Ni_3Ti bulky white precipitates and Ni_4Ti_3/Ni_3Ti_2 needle-like precipitates; (b) indexing legend for the EDS analysis and (c) chemical analysis of the observed phases.

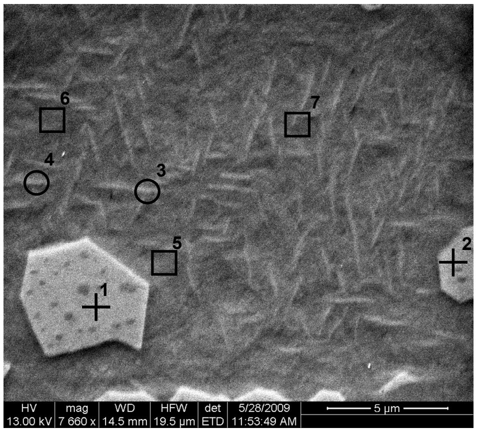

(a)

□ $Ni_{60}Ti_{40}$ matrix
\+ Ni_3Ti precipitates
○ Ni_4Ti_3/ Ni_3Ti_2 Precipitates

(b)

Position	Ni wt.% (at.%)	Ti wt.% (at.%)
1	81.89 (78.68)	18.11 (21.32)
2	78.98 (75.40)	21.02 (24.60)
3	61.06 (56.13)	38.94 (43.87)
4	62.07 (57.18)	37.93 (42.82)
5	61.08 (56.15)	38.92 (43.85)
6	62.09 (57.19)	37.91 (42.81)
7	62.70 (57.83)	37.30 (42.17)

(c)

Figure 79. Second site of observation and measurement: SEM EDS analysis of the surface of $Ni_{60}Ti_{40}$ SMA actuators after shape set treatment; (a) area of interest showing the different phases: NiTi matrix, Ni_3Ti bulky white precipitates and Ni_4Ti_3/Ni_3Ti_2 needle-like precipitates; (b) indexing legend for the EDS analysis and (c) chemical analysis of the observed phases.

5.2.2. Short aging treatment: HT#1

Subsequent to the shape set treatment is aging treatment followed by water quenching cooling to stabilize formed metastable precipitates. The aging treatment in this case is one hour at 450°C. It was found that the furnace cooling performed on the homogenized $Ni_{60}Ti_{40}$ resulted in the formation of not only Ni_3Ti stable precipitates but also in the existence of Ni_4Ti_3 and Ni_3Ti_2 metastable precipitates. The chemical process involved is redistribution of the Nickel from the Ni_3Ti precipitates into the matrix to form the metastable species mentioned above and in Table 21. According to previous studies [45, 46, 47] and Table 21, short aging at 450°C would only result in the formation of Ni_4Ti_3, however, in our study, the starting point for aging at 450°C is a post shape set treatment that already exhibits the three different phases previously discussed. Therefore, one can see the aging treatment post shape set as a tuning of the chemical balance between all precipitates and the matrix. Recent work from Eggeler discusses the influence of Nickel concentration gradients between precipitates resulting in different material response but not much change in the microstructure, as the precipitates are the same, just the local composition of the matrix differing between different aging times [50, 72]. The aging treatment discussed here is the one hour treatment at 450°C followed by water quenching.

An overview of the resulting microstructure is given in Figure 80. It appears that the Ni_3Ti stable bulky precipitates are still present but the Ni_4Ti_3 and Ni_3Ti_2 precipitates seem to be much less visible. Chemical analysis of the different phases confirms the existence of the Ni_3Ti bulky precipitates, a NiTi matrix with less Nickel than measured after the shape set treatment, indicative of further depletion of Nickel from the matrix towards the precipitates. However, it was expected to identify the presence of Ni_4Ti_3 and Ni_3Ti_2 precipitates and none could be clearly found. The composition analysis of the NiTi matrix from Figure 81 and Figure 82 indicate a slight variation in Nickel content from approximately 62 wt.% down to regions with 54 wt.%, and therefore it is thought that even if the precipitates are not visible, they are part of a very fine microstructure and simply could not be isolated from the matrix. What is even more interesting is the presence of low Nickel content regions. Those regions correspond mostly to the interfaces between NiTi matrix and Ni_3Ti precipitates. This indicates that during aging, the induced concentration gradient did not find equilibrium at the time water quench was performed. Those areas are mostly where clustering of Ni_3Ti precipitates or where larger Ni_3Ti precipitates were identified, as seen in Figure 81 and Figure 82.

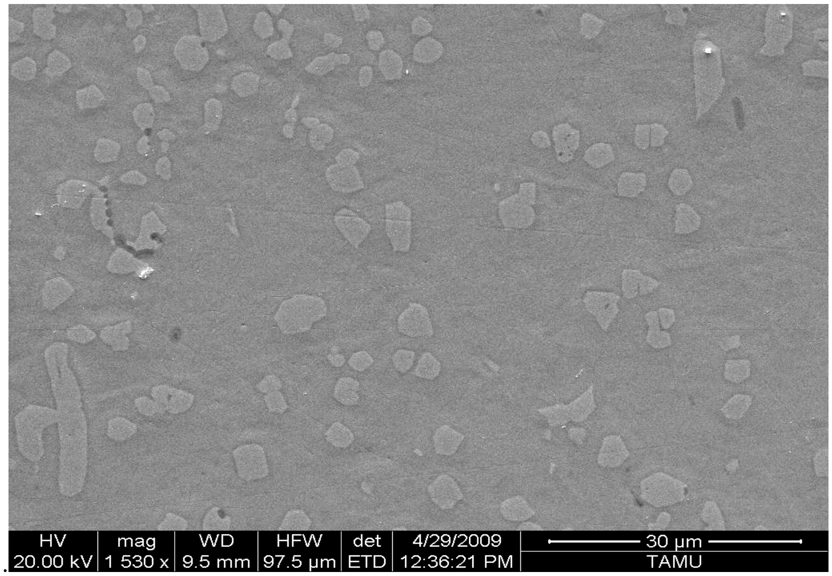

Figure 80. SEM micrograph of polished $Ni_{60}Ti_{40}$ SMA after shape set followed by short aging treatment of one hour at 450°C water quenched; overview of the different phases.

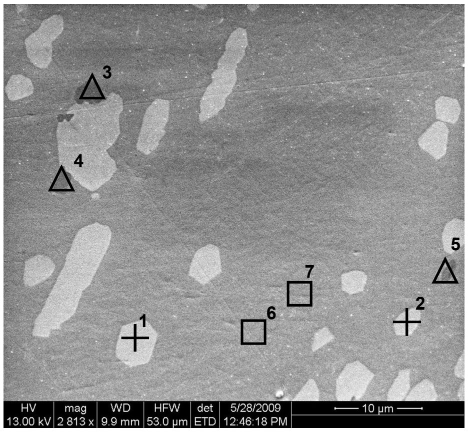

(a)

□ $Ni_{60}Ti_{40}$ matrix

+ Ni_3Ti precipitates

△ Ni-low regions

(b)

Index	Ni wt.% (at.%)	Ti wt.% (at.%)
1	81.07 (77.75)	18.93 (22.25)
2	79.84 (76.37)	20.16 (23.63)
3	45.03 (40.06)	54.97 (59.94)
4	46.39 (41.38)	53.61 (58.62)
5	47.36 (42.33)	52.64 (57.67)
6	60.51 (55.56)	39.49 (44.44)
7	62.00 (57.10)	38.00 (42.90)

(c)

Figure 81. First site of observation and measurement: SEM EDS analysis of the surface of $Ni_{60}Ti_{40}$ SMA actuators after short aging treatment; (a) area of interest showing the different phases: NiTi matrix, Ni_3Ti bulky white precipitates and globular areas with low nickel content; (b) indexing legend for the EDS analysis and (c) chemical analysis of the observed phases.

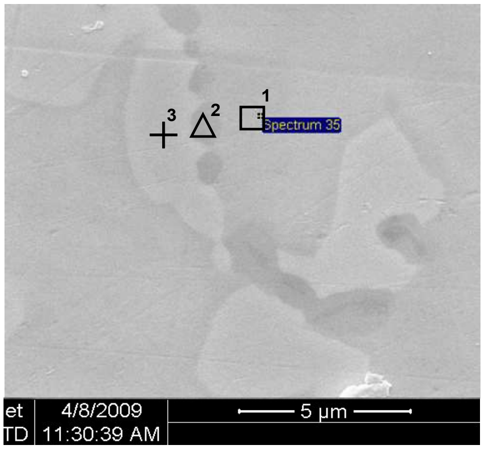

(a)

Index	Ni wt.% (at.%)	Ti wt.% (at.%)
1	54.19 (49.11)	45.81 (50.89)
2	46.98 (41.96)	53.02 (58.04)
3	76.61 (72.77)	23.39 (27.33)

(c)

□ $Ni_{60}Ti_{40}$ matrix

+ Ni_3Ti precipitates

△ Ni-low regions

(b)

Figure 82. Second site of observation and measurement: SEM EDS analysis of the surface of $Ni_{60}Ti_{40}$ SMA actuators after short aging treatment; (a) area of interest showing the different phases: NiTi matrix, Ni_3Ti bulky white precipitates and Ni-low region; (b) indexing legend for the EDS analysis and (c) chemical analysis of the observed phases.

5.2.3. Long aging treatment: HT#2

In the case of the longer aging treatment following the shape set treatment, the typical microstructure and present phases are shown in Figure 83.

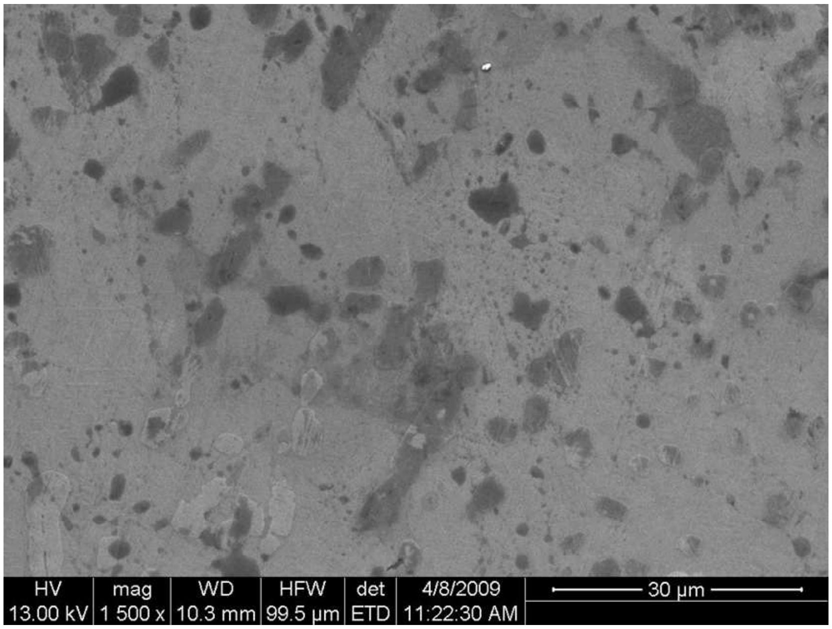

Figure 83. SEM micrograph of polished $Ni_{60}Ti_{40}$ SMA after shape set followed by long aging treatment of 20 hours at 450°C then water quenched; overview of the different phases.

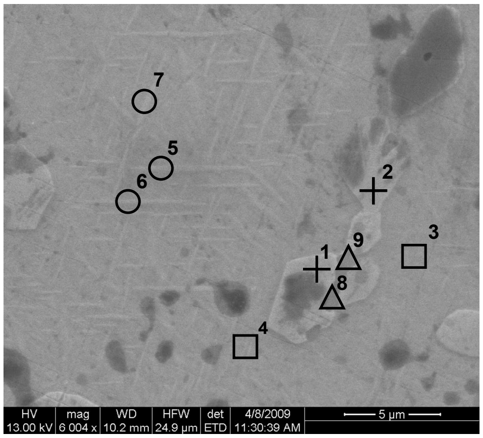

(a)

┼ Ni_3Ti Precipitates

☐ $Ni_{60}Ti_{40}$ Matrix

○ Ni_4Ti_3/Ni_3Ti_2 Precipitates

△ Ni-low regions in matrix

(b)

Index	Ni wt.% (at.%)	Ti wt.% (at.%)
1	81.90 (78.68)	18.10 (21.32)
2	81.62 (78.37)	18.38 (21.63)
3	62.82 (57.96)	37.18 (42.04)
4	61.74 (56.83)	38.26 (43.17)
5	65.10 (60.35)	34.90 (39.65)
6	65.62 (60.89)	34.38 (39.11)
7	64.86 (60.10)	35.14 (39.90)
8	49.35 (44.28)	50.65 (55.72)
9	49.34 (44.28)	50.66 (55.72)

(c)

Figure 84. Site of observation and measurement: SEM EDS analysis of the surface of $Ni_{60}Ti_{40}$ SMA actuators after long aging treatment; (a) area of interest showing the different phases: NiTi matrix, Ni_3Ti bulky white precipitates and Ni_4Ti_3 / Ni_3Ti_2 needle-like precipitates; (b) indexing legend for the EDS analysis and (c) chemical analysis of the observed phases.

5.3. Fractography of $Ni_{60}Ti_{40}$ SMA actuators

The analysis of the fracture surfaces and surface of the fatigue test specimens focuses on two specific areas of the failed specimens. Figure 85 presents two failed $Ni_{60}Ti_{40}$ fatigue specimens with a schematic magnification of the areas of interest. The first area of interest is the actual fracture surface with a second area of interest, i.e. the surface of the SMA fatigue specimen. The next section will focus on the failure mechanisms identifiable from the analysis of the damaged microstructure and from the crack initiation and propagation patterns.

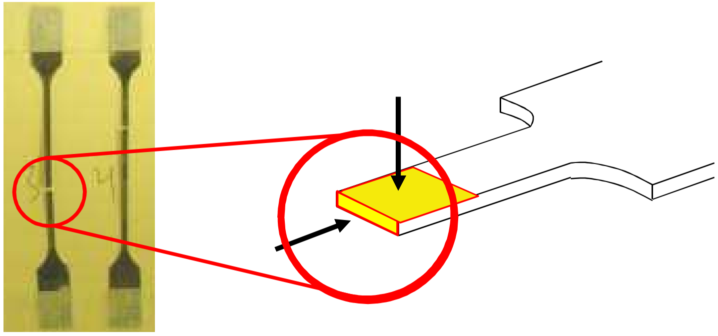

Figure 85. Picture of two different Ni-rich NiTi fatigue specimens showing random localization of the fatigue failure occurring within the designed test gauge; and a schematic showing the corresponding area of interest in terms of fractography.

5.3.1. Influence of material/process parameters on fatigue crack initiation and propagation

5.3.1.1. Influence of heat treatment time

As introduced earlier, the different heat treatment times results in Nickel concentration gradients between the Ni-rich precipitates and the NiTi matrix. A different composition means a different behavior in terms of transition temperatures, hardening and heat of transformation. Heat treatment HT#1 corresponds to the heat treatment that presents smooth transitions in terms of constant stress hysteresis, as shown in Figure 49, as well as in phase transformation temperatures, as shown in Figure 45.

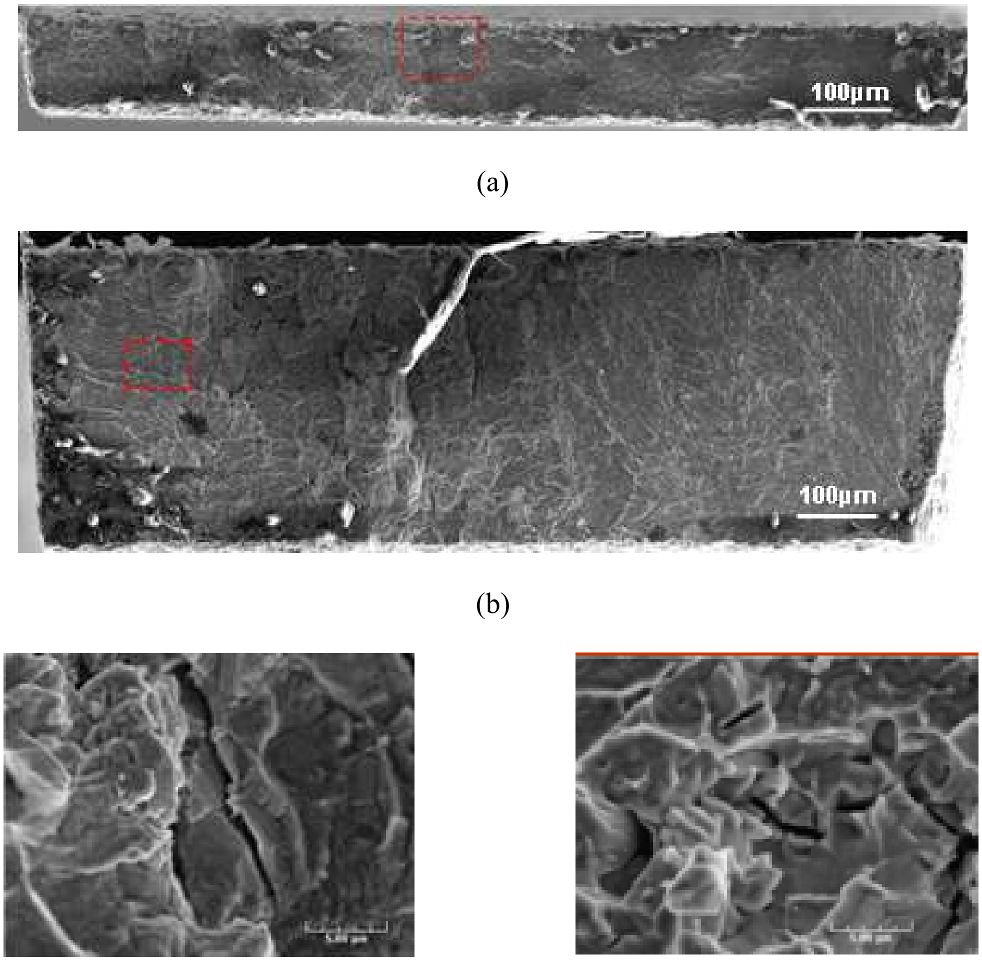

(a)

(b)

(c)

(d)

Figure 86. SEM fractographies for fatigue specimens tested after HT#1 under 100 MPa: full fractography of (a) 5 mils thick specimen and (b) 15 mils thick specimen; (c) high magnification area of 5 mils thick specimen and (d) 15 mils thick specimen.

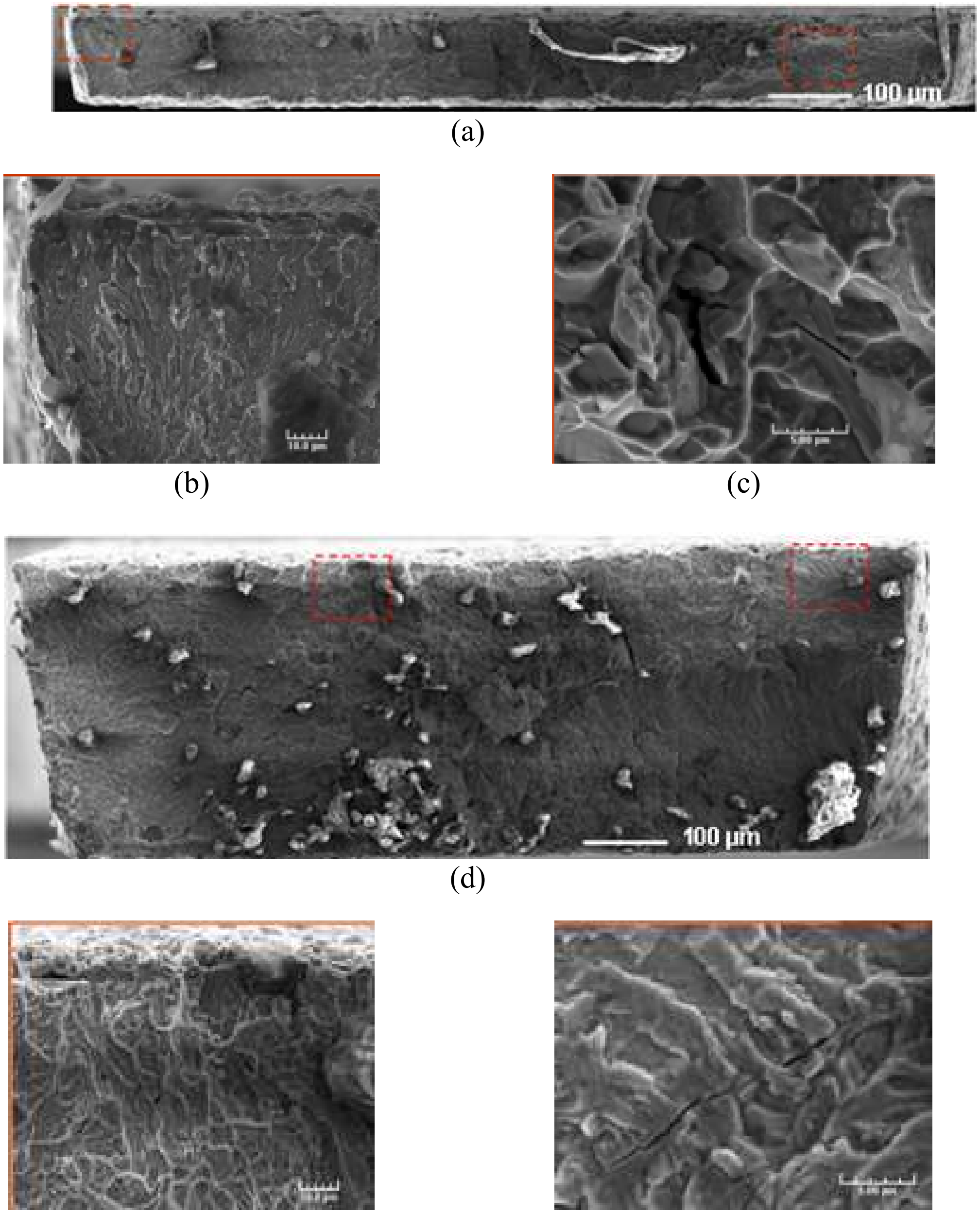

(a)

(b) (c)

(d)

(e) (f)

Figure 87. SEM fractographies for fatigue specimens after HT#1 under 250 MPa: (a) 5 mils thick and (d) 15 mils thick full fractography; (b)-(c) high magnification of 5 mils thick specimen and (e)-(f) high magnification of 15 mils thick specimen.

The thin specimen shows initiation at one edge with propagation across the width until the cracks became unstable and the specimen failed. The cracks that formed during propagation and before final failure seem to all be oriented transversely to the thickness as shown in Figure 86(a), Figure 86(c), Figure 87(a), Figure 87(b) and Figure 87(c). In opposition, the thick specimens present a bulk response that does not exhibit anymore the observed fracture behavior seen in the thin specimens.

In the case of HT#2, the fractographies show different features. It appears that fatigue striations and fatigue lines, corresponding to crack tip propagation upon cyclic loading are much more contrasted, as shown in Figure 88 and Figure 89. As the transition temperature were raised from HT#1 to HT#2, longer aging times seems to impact the actuators response in terms of ductility (discussed in Chapter IV) but also in terms of crack evolution. HT#2 makes the SMA more ductile, therefore more sensitive to accumulation of plastic deformation, but also more resistant to crack instability as plasticity acts as crack blunting mechanism. Another aspect of crack propagation is the high precipitation density that can be observed at higher magnification. The clear appearance of precipitates of the order of 2 μm to 5 μm along the fatigue lines that can be seen in Figure 89(f), while the influence of thickness is still visible, just as seen in fractographies from HT#1 specimens.

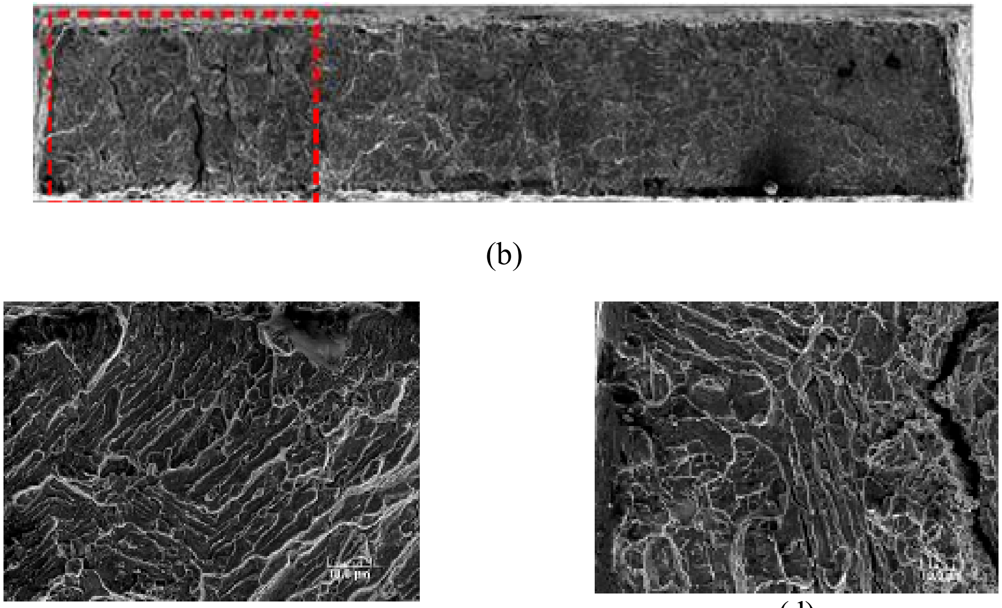

(b)

(c)

(d)

Figure 88. SEM fractographies for fatigue specimens tested after HT#2 under 100 MPa: full fractography of (a) 5 mils thick specimen and (b) 10 mils thick specimen; (c) high magnification area of 5 mils thick specimen and (d) 10 mils thick specimen.

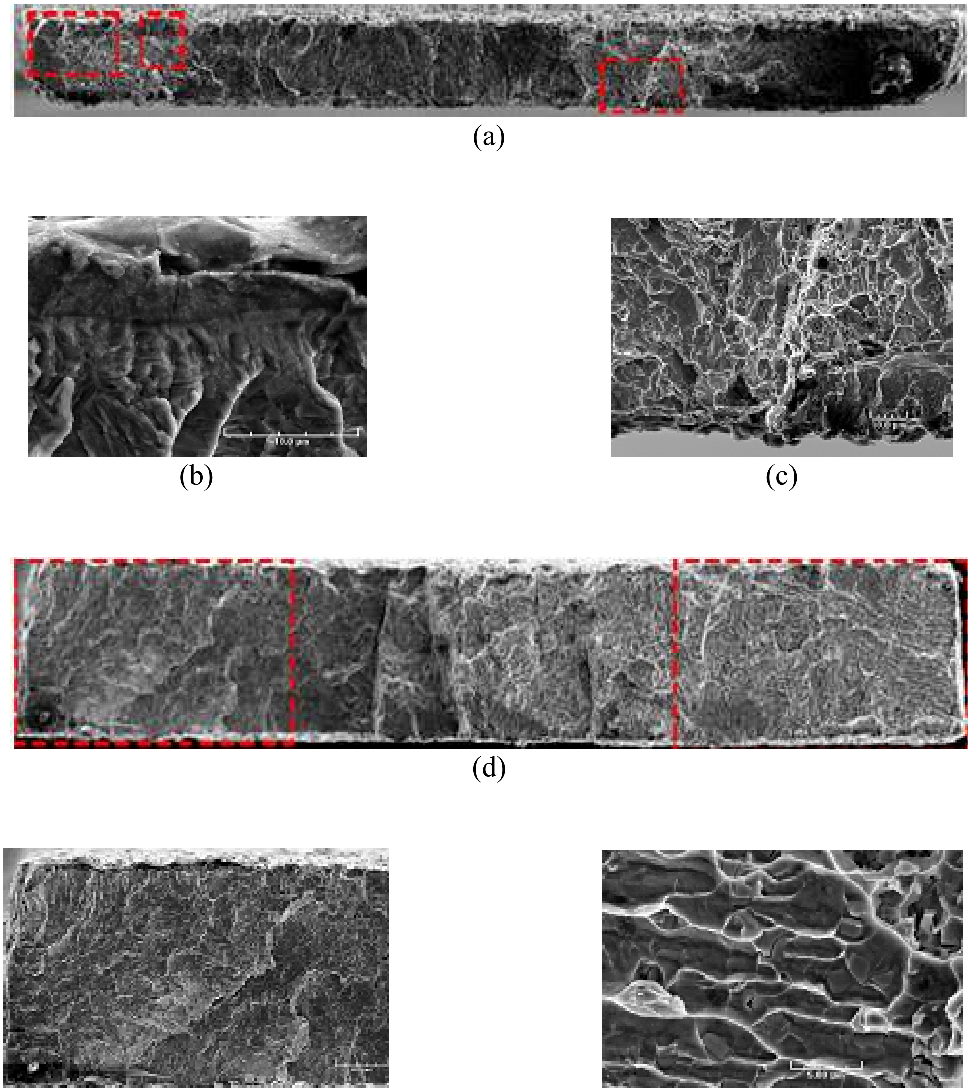

(a)

(b) (c)

(d)

(e) (f)

Figure 89. SEM fractographies for fatigue specimens after HT#2 under 250 MPa: (a) 5 mils thick and (d) 10 mils thick full fractography; (b)-(c) high magnification of 5 mils thick specimen and (e)-(f) high magnification of 10 mils thick specimen.

5.3.1.2. Influence of heat treatment atmosphere

Two series of fatigue specimens were prepared in two different ways, as described in Chapter IV. While the first series of fatigue specimens were heat treated in high vacuum atmosphere, the second series of specimens were heat treated in air. The macroscopic analysis from Chapter IV showed how air heat treatment was affecting the fatigue life of thin specimens. The second series of specimens failed below approximately 2,000 cycles under 100MPa and 150MPa applied stress as a result of being heat treated in air, as shown in Figure 90, while vacuum heat treatments performed on the first series of specimens resulted in number of cycles approximating 50,000 cycles (Figure 91).

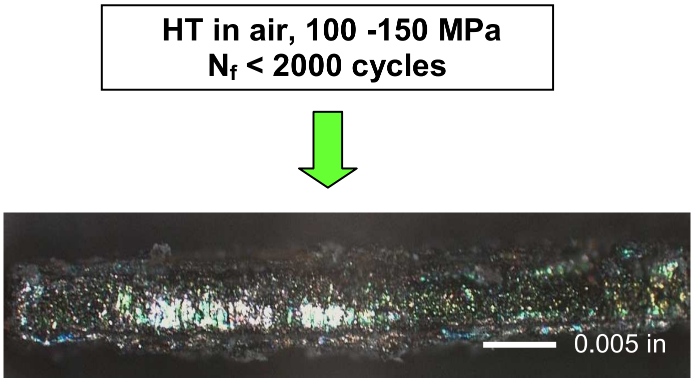

Fracture surface, thickness = 5 mils

Figure 90. Identification of very low number of cycles to failure for air heat treated specimens.

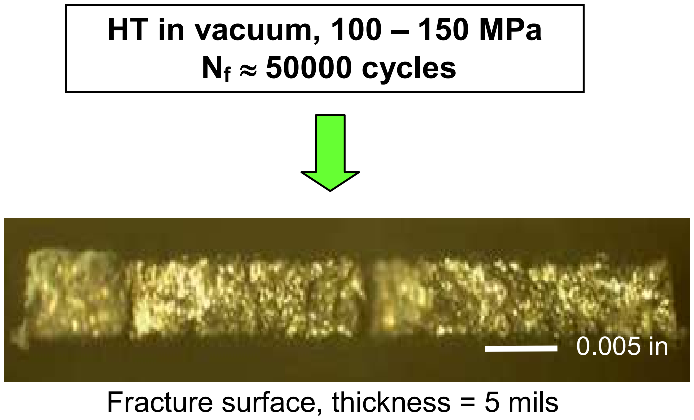

Figure 91. Identification of very low number of cycles to failure for high vacuum heat treated specimens.

Transverse fatigue lines across the thickness of the thin specimens can be observed in both types of heat treatment. However, a significant oxide layer can be identified surrounding the entire specimens hest treated in air. The interface is well defined and cracks initiating from the oxide layer and from the interface oxide/SMA indicate can be identified and concluded to lead to further crack formation and propagation in the entire SMA actuators, as shown for both thick and thin specimens in Figure 92 and Figure 93, respectively. The oxide layer that was created has the same thickness of approximately 25µm, which represent 2/5 of the entire specimen thickness for the thin specimens and 2/15 of the entire specimen thickness for the thick specimens. Figure 94 is an SEM-EDS analysis of the oxide layer formed upon air heat treatment and presents the identification of the different phase compositions after short aging (HT#1). The oxide layer is mostly composed of Titanium and Oxygen, depleting the core of the SMA actuator from Ti and making it even more Nickel rich.

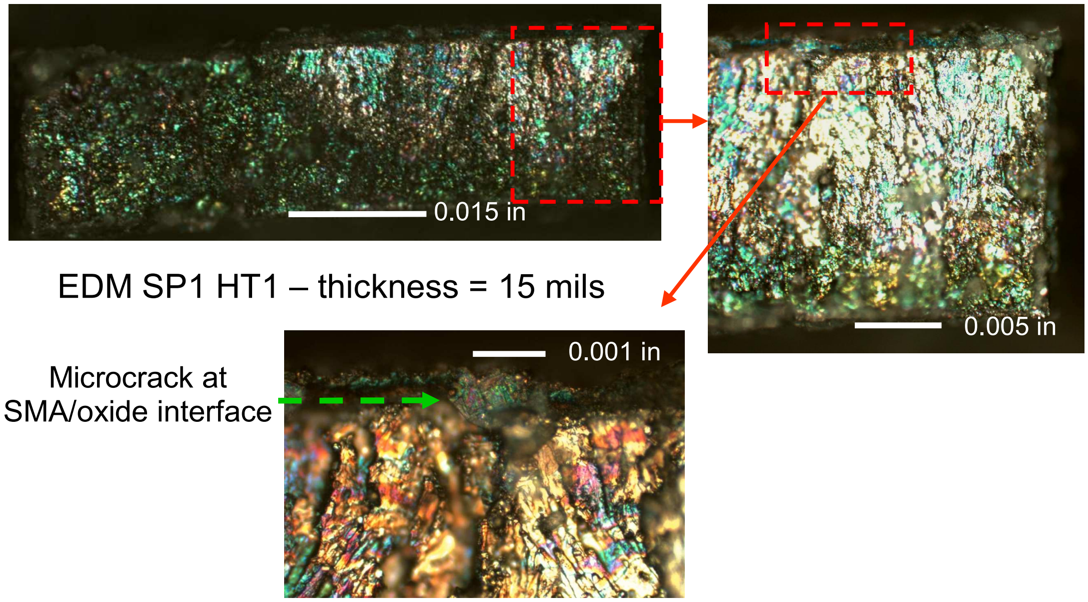

Figure 92. Optical fractography for fatigue test specimen EDM SP1 HT#1.

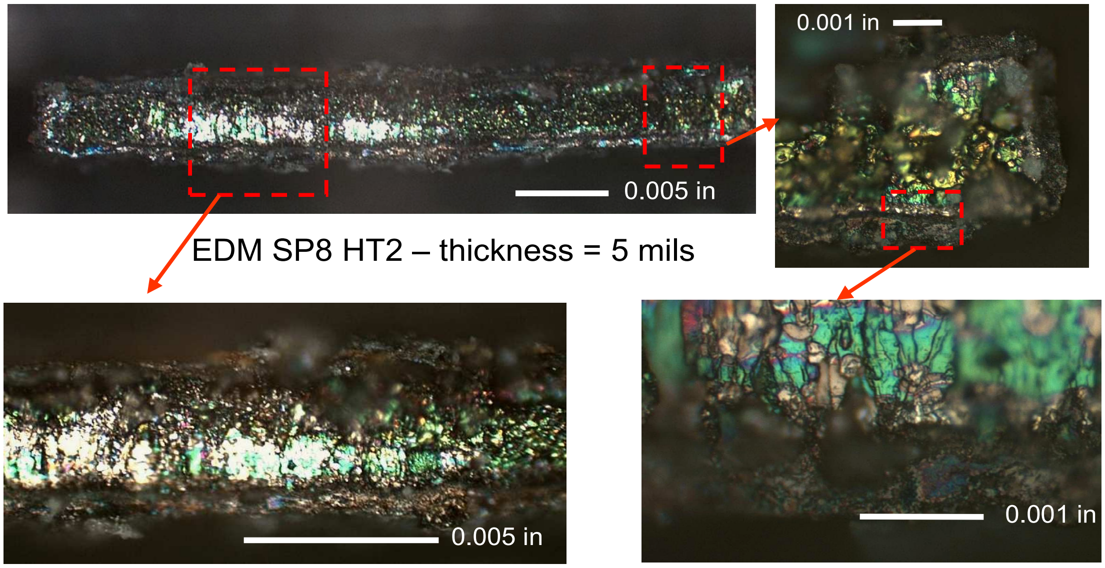

Figure 93. Optical fractography for fatigue test specimen EDM SP8 HT#2.

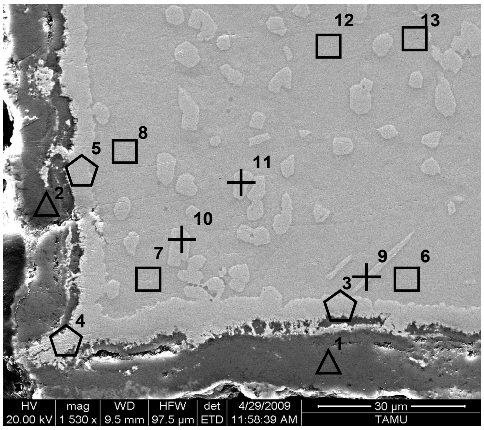

(a)

☐ $Ni_{60}Ti_{40}$ matrix

+ Ni_3Ti precipitates

△ Ti oxide layer (Ni-low due to air HT)

⬠ Recast layer from EDM cutting

(b)

Position	Ni wt.% (at.%)	Ti wt.% (at.%)	O wt.% (at.%)
1	**/**	**57.64 (31.24)**	**42.36 (68.76)**
2	**0.80 (0.37)**	**59.91 (33.63)**	**39.28 (66.01)**
3	**77.31 (73.55)**	**22.69 (26.45)**	**/**
4	***95.66 (94.73)***	***4.34 (5.27)***	***/***
5	**77.27 (73.50)**	**22.73 (26.50)**	**/**
6	**54.69 (49.62)**	**45.31 (50.38)**	**/**
7	**56.36 (51.31)**	**43.64 (48.69)**	**/**
8	**54.97 (49.90)**	**45.03 (50.10)**	**/**
9	**76.34 (72.48)**	**23.66 (27.52)**	**/**
10	**77.05 (73.26)**	**22.95 (26.74)**	**/**
11	**76.82 (73.00)**	**23.18 (27.00)**	**/**
12	**55.35 (50.28)**	**44.65 (49.72)**	**/**
13	**55.07 (50.00)**	**44.93 (50.00)**	**/**

(c)

Figure 94. Site of observation and measurement: SEM EDS analysis of the surface of $Ni_{60}Ti_{40}$ SMA actuators after short aging treatment in this example; (a) area of interest showing the dark oxide layer (EDS spots number 1 and 2), the recast-layer (3and 5): NiTi matrix (6 – 8, 12 and 13), Ni_3Ti bulky white precipitates (9 – 11); (b) indexing legend for the EDS analysis and (c) chemical analysis of the observed phases.

5.3.2. Influence of test parameters on fatigue crack initiation and propagation

5.3.2.1. Influence of specimen thickness

The influence of the specimen thickness can be seen as cracks are generated across the thickness of SP3 HT#1 where as SP7 HT#1 displays more of a bulk behavior with different failure behavior from thickness 5 mils to 15 mils, as shown in Figure 95 and Figure 96. It was discussed in the previous section how thin specimens develop transverse cracks while thick specimens were showing more of a bulk material response (Figure 86 through Figure 89), as well as the influence of the thickness of the specimens when heat treatments were performed in air versus in high vacuum (Figure 90 through Figure 93).

From those collective observations and analysis of damage formation and propagation, it can be concluded that below 10 mils thick, specimens were starting to exhibit a strong thickness to width ratio dependency and therefore were removed from further fatigue testing due to their sensitivity to external influence as well as not being representative enough of the actual SMA beam actuators fatigue response.

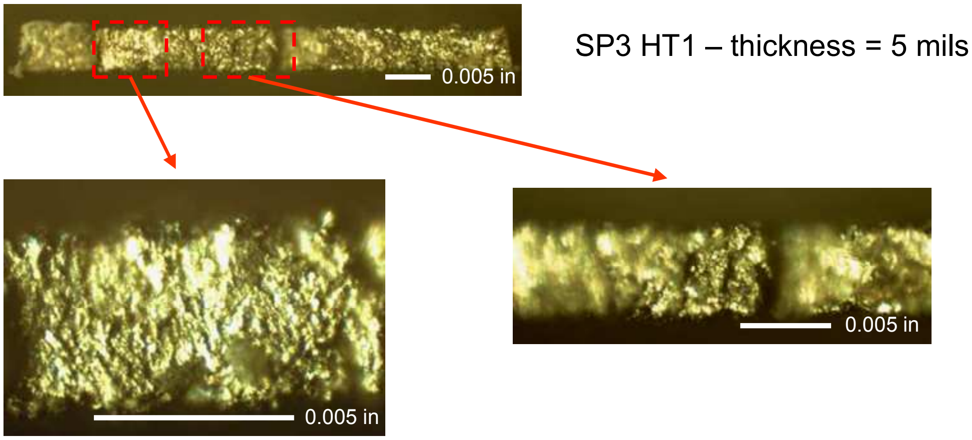

Figure 95. Optical fractography for fatigue test specimen SP3 HT#1.

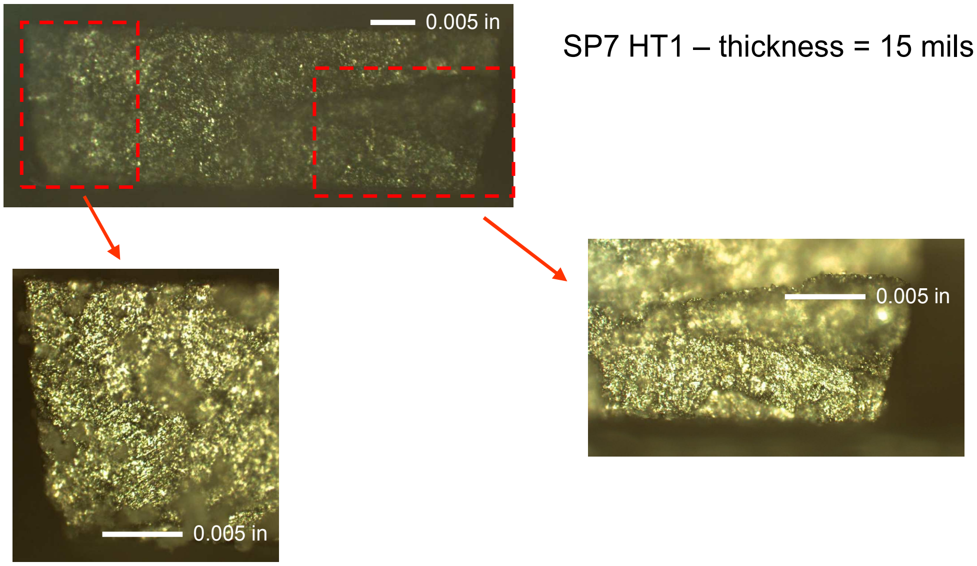

Figure 96. Optical fractography for fatigue test specimen SP7 HT#1.

5.3.2.2. Influence of recast-layer/HAZ removal

In addition to improving the fatigue results (see fatigue testing results of polished vs. as-received specimens in previous sections), the microstructure and especially the morphology of the crack formation at the surface of the fatigued specimens is improved. Figure 97 shows a specimen in which the recast-layer caused major transverse surface cracks that ultimately led to early failure of the component.

After removal of the recast-layer/HAZ, the failure of the actuator can be identified to initiate at the surface, as it can be expected, but the failure can be attributed to the biphasic nature of the SMA where clusters of Ni_4Ti_3 precipitates seem to weaken the matrix and induce debonding and crack formation, as shown in Figure 98 and Figure 99.

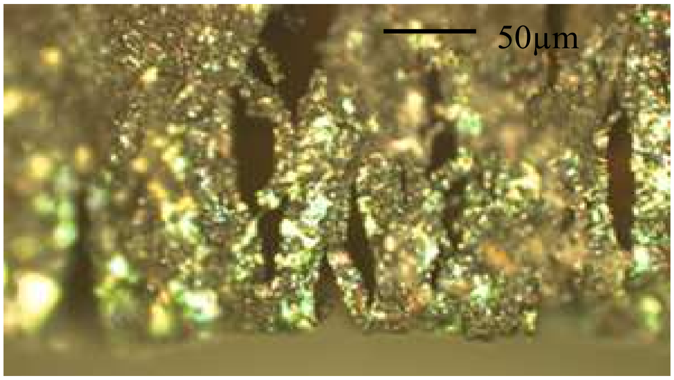

Figure 97. Optical micrographs showing the surface of an SMA actuator with recast-layer. Cracks formed upon cyclic loading in the recast-layer that caused early failure.

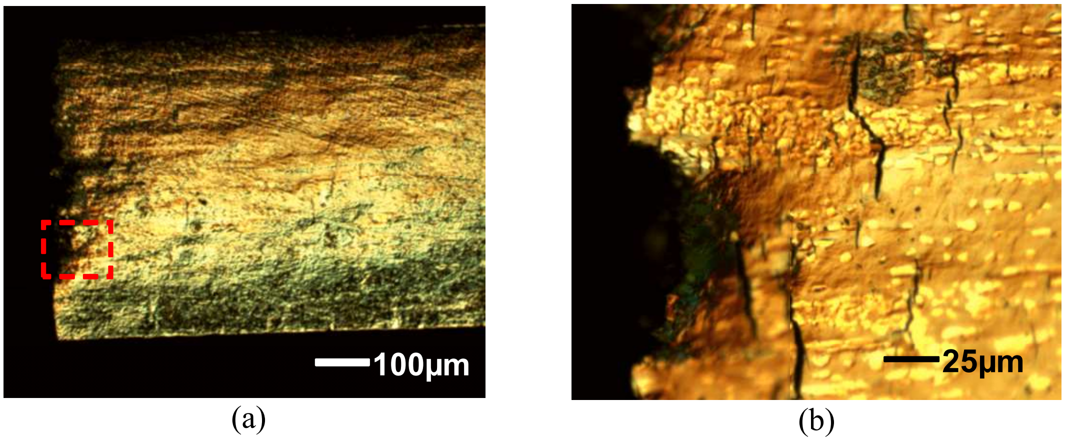

(a) (b)

Figure 98. (a) Optical surface analysis of a failed polished specimen; (b) traces of clustered precipitates are visible and present higher crack density than in the NiTi matrix with fewer precipitates.

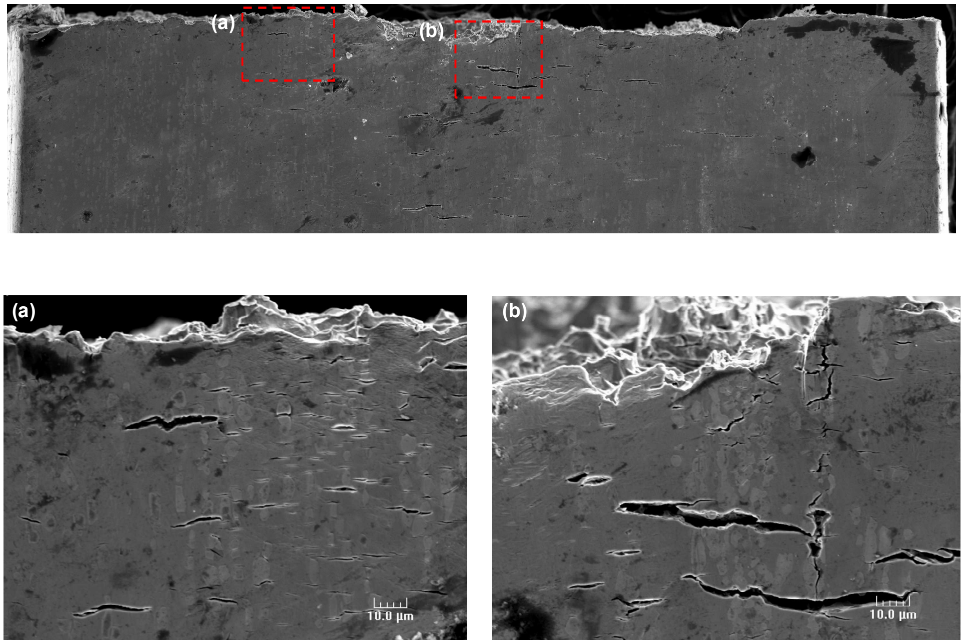

Figure 99. SEM surface analysis of the specimen presented in Figure 98. The transverse cracks formed upon cyclic loading are present near or in contact with the precipitates (a); (b) shows a magnification on larger propagated cracks and longitudinal crack formation on a line of clustered precipitates.

From these results and observations, it appears that the failure of the Ni-rich NiTi SMA actuators aged 20hrs. at 450°C is driven by crack formation/interaction precipitates/NiTi matrix.

It has been understood that the formation of a recast-layer upon EDM wire cutting was detrimental to the fatigue life of SMA actuators due to partial loss of SM, brittleness, and to an area of the material that was affected by the heat, i.e. heat affected zone (HAZ). Fracture surface of failed specimens with and without recast-layer/heat affected zone show different features. Figure 100 and Figure 101 show fractographies for an as-received specimen and a specimen with removed top and bottom recast-layer/heat affected zone, respectively, both failed after fatigue testing under 200MPa. The sides, however, were voluntarily left intact to observe the influence of different surface properties on one specimen.

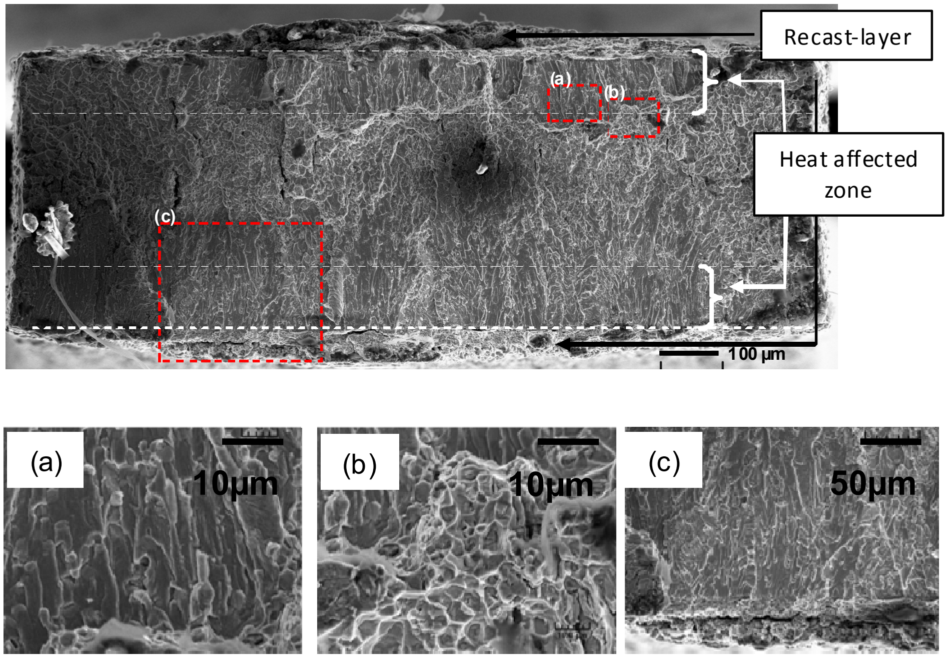

Figure 100. SEM fractography of as received fatigued specimen, tested under 200MPa; (a) detail of the heat affected zone, (b) interface HAZ/ unaffected SMA and (c) detail on the brittle aspect of the recast layer and the interface recast-layer/HAZ.

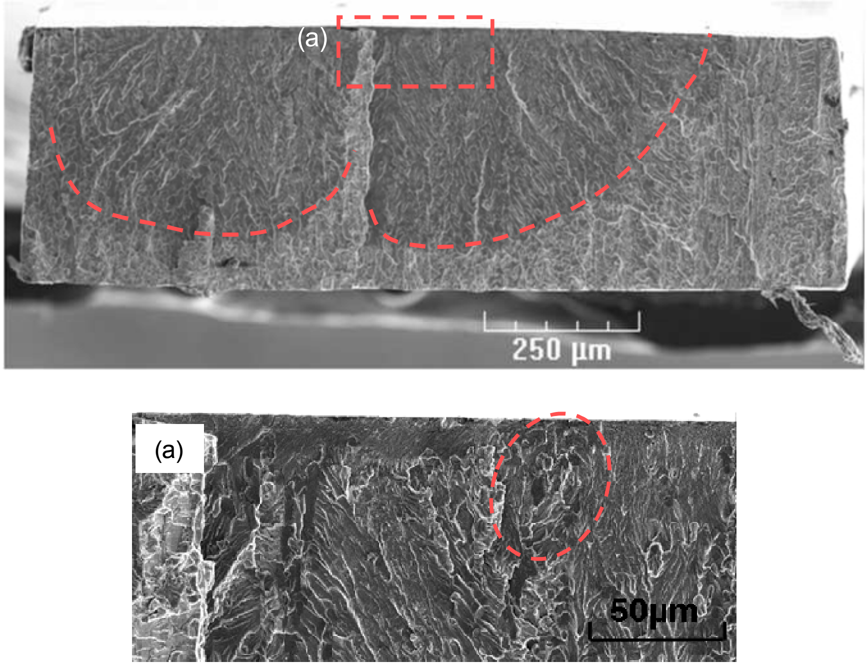

Figure 101. SEM fractography of a polished fatigued specimen, tested under 200MPa showing initiation site and two fatigue propagation areas; (a) detail of the initiation site with sub-surface defect found to be a Ni_3Ti precipitate.

5.3.2.3. Influence of cooling environment

The influence of the environment on the fatigue life of the $Ni_{60}Ti_{40}$ SMA actuators was assessed for polished specimens only. The damage caused by the presence of the recast layer was too important to compare corrosive and non-corrosive conditions on the as-received specimens. Therefore, the effect of corrosion induced by the combined effects of resistive joule heating and a fluid convective cooling versus corrosion-free conditions obtained in a dry non-conducting medium (i.e. gaseous Nitrogen) is assessed by monitoring the damage formed at the surface of the fatigued specimens. The interpretation of damage comprises surface roughness, crack formation and distribution.

Figure 102 and Figure 103 are representative assessment of surface damage indentified for corrosion-free and corrosive conditions, respectively. The comparison of damage accumulated during cyclic loading in corrosive and non-corrosive conditions is performed at the fatigue failure location and away from it. The purpose is to verify any possible localization process during cyclic loading. The first result that we can discuss can be seen in Figure 102(a), Figure 102(b) and in Figure 103(a) and Figure 103(b). The surface micrographs correspond to surface observation of the fatigued specimens at or near the fracture surface (fracture surface edge visible in the top part of the micrographs), with schematic representation of the position where fracture occurred and what observation site is being investigated, as shown in Figure 102(e) and Figure 103(e). The observations from the micrographs near the fracture surface show formation of cracks at the interface NiTi matrix/ Ni_3Ti precipitates and for some within the Ni_3Ti precipitates, for both corrosive and non-corrosive testing conditions. However, when comparing the influence of corrosion on the crack formation away from the fracture surface, corrosion-free conditions show no crack initiation, just an evolution of the surface roughness, indicative of deformation processes that led to evolution of the surface quality, as shown in Figure 102(c) and Figure 102(d). However, the surface analysis of the specimens tested in a corrosive environment show formation of cracks over the entire surface of the SMA actuators, as seen in Figure 103(c) and Figure 103(d).

The first conclusion from these observations is that damage will accumulate, no matter what environment the specimens are testing in, however, as previously shown, a corrosive environment will contaminate and damage the entire surface of the actuators, which combined to corrosion-free accumulation of damage and localization of fracture, results in an accelerated fatigue failure. This result is confirmed by the fatigue life results shown in Chapter IV in Figure 64.

The formation of cracks and damage due to corrosive cooling conditions can be seen in Figure 103. However, it is when comparing corrosive fatigue failure under high stress level resulting in a relatively low number of cycles to failure, i.e. failure at $N_f \sim$ 10,000 cycles in Figure 104(a) and Figure 104(b), to fatigue failure under low stress resulting in a high number of cycles to failure, i.e. failure at $N_f \sim$ 150,000 cycles shown in Figure 104(c) and Figure 104(d), that the specimen exhibit a well distributed, high density network of cracks. The identified network of cracks was not found to be related to any NiTi matrix and $\mathrm{Ni_3Ti}$ precipitate interactions. This type of damage seems to be related to a secondary type of damage, such as the interactions $\mathrm{Ni_4Ti_3}$ precipitates with the NiTi matrix. This secondary damage formation will be discussed in the next subsection. Some of those results will be the subject of future projects that will be initiated after the completion of this dissertation work.

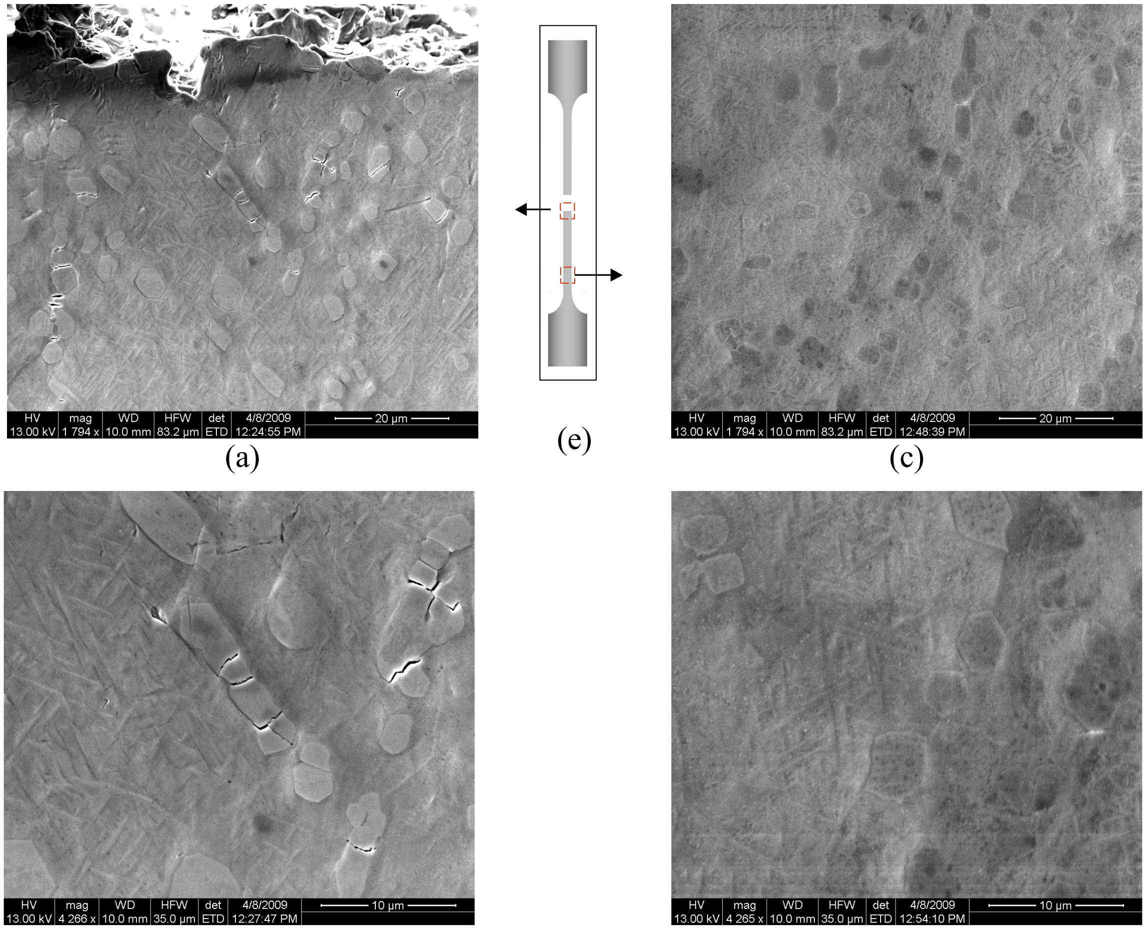

(a) (e) (c)

(b) (d)

Figure 102. Surface aspect of a $Ni_{60}Ti_{40}$ SMA actuator tested in corrosion-free cooling environment under 200 MPa stress level; (a) and (b) are observations near the fracture surface at different magnification showing surface cracks and damage, (c) and (d) are observations away from the fracture surface at different magnification showing surface cracks and damage; (e) is a schematic representing the location of the fracture surface and of the observation sites.

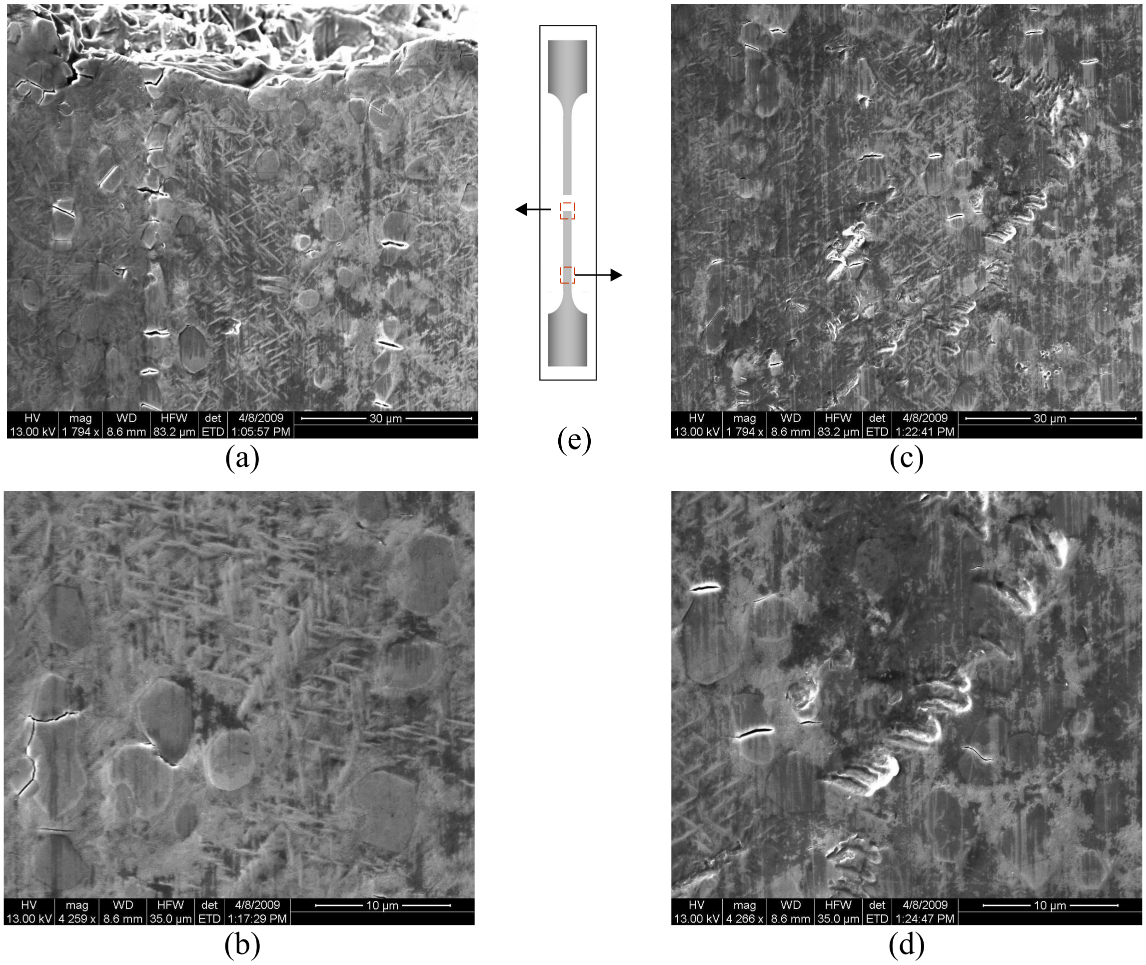

Figure 103. Surface aspect of a $Ni_{60}Ti_{40}$ SMA actuator tested in corrosive cooling environment under 200 MPa stress level; (a) and (b) are observations near the fracture surface at different magnification showing surface cracks and damage, (c) and (d) are observations away from the fracture surface at different magnification showing surface cracks and damage; (e) is a schematic representing the location of the fracture surface and of the observation sites.

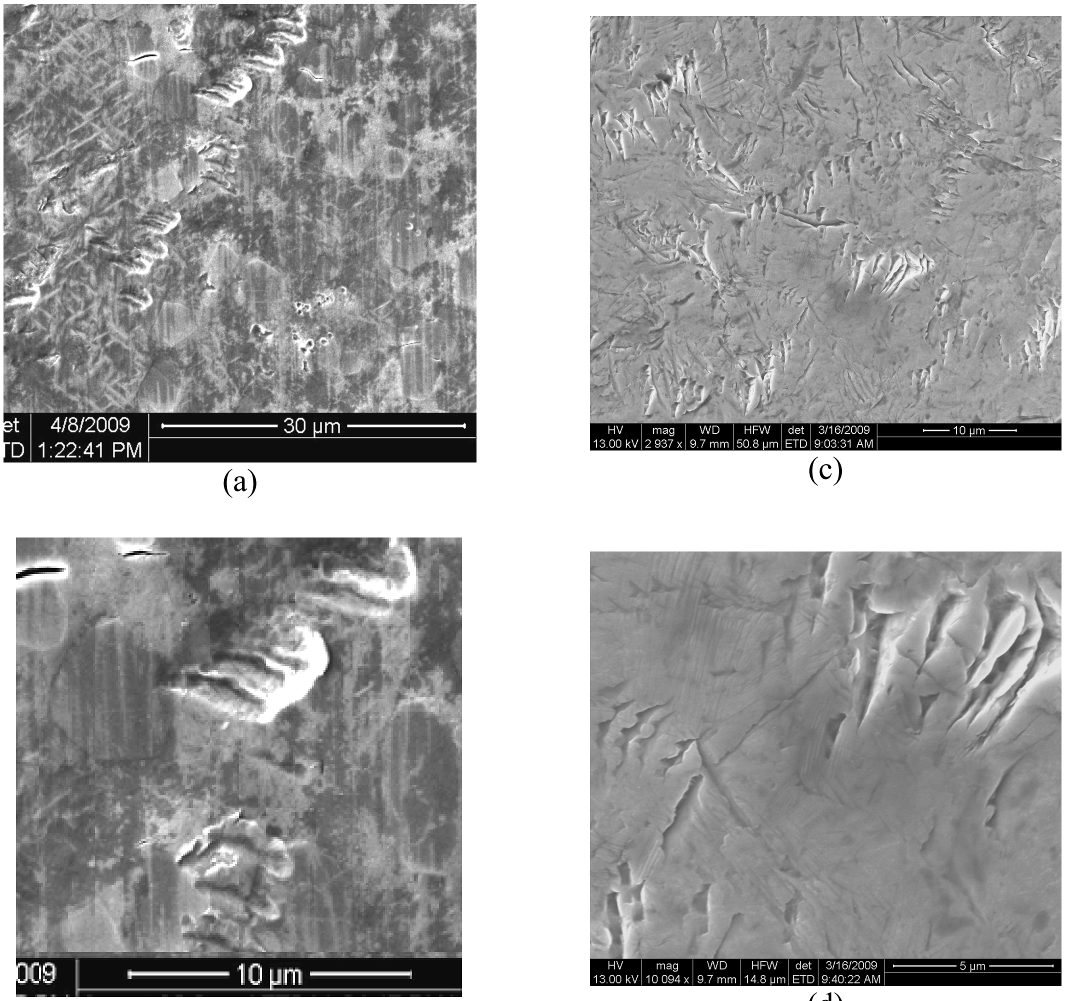

(a) (c)

(b) (d)

Figure 104. Surface aspect of $Ni_{60}Ti_{40}$ SMA actuators tested under corrosive conditions for test conditions of (a, b) 200MPa resulting in Nf ~ 10,000 cycles; and (c, d) 100MPa resulting in Nf ~ 160,000 cycles.

5.4. Precipitate driven fatigue failure mechanisms

In opposition to SMAs that develop large accumulated plastic strain in a quasi-consistent manner for which a Manson-Coffin failure criterion can be developed based on accumulation of plastic strain, as shown in Chapter II, as well as on additional mechanisms such as the effect of simultaneous cyclic loading and corrosion, Ni-rich NiTi SMAs fatigue failure appears to be precipitate dependent. The purpose of this section is to address the effect of two types of Ni-rich precipitates, i.e. Ni_3Ti and Ni_4Ti_3 / Ni_3Ti_2, on the damage and failure mechanisms.

5.4.1. Influence of Ni_3Ti precipitates on failure mechanisms

5.4.1.1. Surface damage characterization

It is found that upon cyclic loading that the surface of the SMA actuators exhibit surface cracks in and around the Ni_3Ti precipitates. Figure 105 shows the details of the damage formed around and in the Ni-rich precipitates. The presence on the NiTi matrix of large Ni_3Ti precipitates create a non-coherent stress field that is accommodated by inelastic strains rather than elastic strains. Those regions are coexisting with phase transforming NiTi matrix and result in large strain incompatibilities cycled through repeated phase transformation. From previous nanoindentation results, the mechanical properties showed Ni_3Ti precipitates twice as hard as the NiTi matrix, which would indicate lower accommodation of elastic strains and higher brittleness of the bulky Ni-rich precipitates, as shown in Figure 75 and Figure 76. Under cyclic loading, damage is observed to form and induce cracks along the loading direction of the SMA actuators at the two extremities of the Ni_3Ti precipitates. This mechanism of repeated cyclic transformation is therefore responsible for high stresses resolved into the precipitates and around the precipitates. The cracks mostly form in a mode 1, at the interface between Ni_3Ti and NiTi matrix and inside the Ni_3Ti precipitates, as shown in Figure 105.

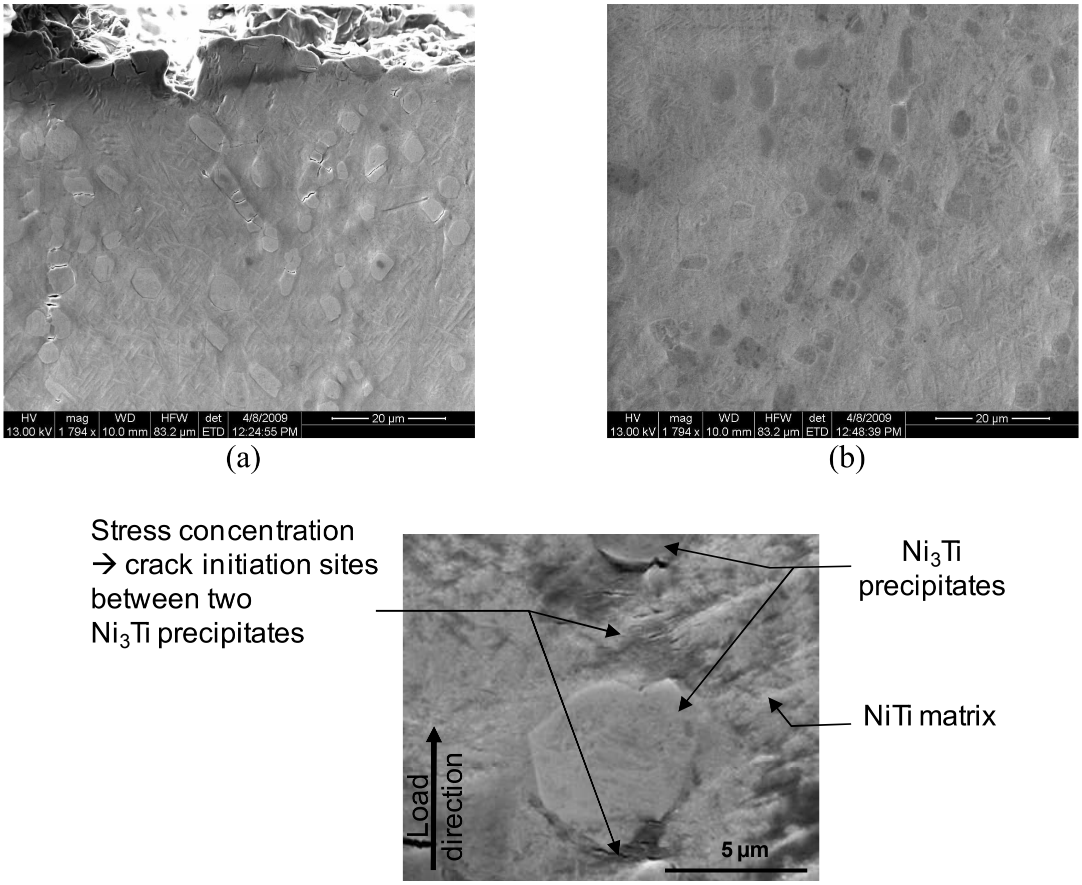

(a) (b)

(c)

Figure 105. Site of observation and measurement post fatigue failure (top horizontal crack being edge of fracture surface) tested in Nitrogen: SEM EDS analysis of the surface of $Ni_{60}Ti_{40}$ SMA actuators after long aging treatment; (a) high crack density near fracture surface, (b) low crack density away from fracture, (c) interaction sites between NiTi matrix and Ni_3Ti with crack formation.

5.4.1.2. Bulk damage characterization

The assessment of the surface damage is now compared to fracture surfaces and bulk damage. As cycles progress during fatigue testing, damage forms around the precipitates and the overall SMA actuator failure can be identified as ductile, as shown in Figure 106. Figure 106(a) shows the fracture surface of a $Ni_{60}Ti_{40}$ fatigued specimen with Figure 106(b) showing the details of three cracks that propagated through the thickness. Features like ductile dimples and Ni_3Ti precipitates at the center of nearly each dimple can be observed and related to failure of the Ni-rich precipitates. The NiTi matrix demonstrates ability to accommodate the large deformation due to phase transformation under constant stress resulting in 1-1.2% actuation. However, it was previously shown how the Ni_3Ti precipitates are stiffer, harder and are acting as inhomogeneities. The consequence is brittle failure by cleavage or near cleavage as shown in Figure 107 and Figure 108. A process related issue was clearly identified during post mortem analysis with consequences resulting in the propagation of cracks through the thickness of the SMA actuators. It appears that during solidification and hot rolling, the material developed preferred locations to grow Ni_3Ti precipitates. The clustering of Ni_3Ti precipitates is found to permit coalescence of cracks developed inside and around the Ni_3Ti precipitates. SMAs have the properties to delay crack growth due to the effect of martensitic transformation and plastic strain accumulation, acting a shield for further crack progression. An example of precipitate clustering and crack propagation can be seen in Figure 109. Figure 110 is a schematic and three-dimensional representation of the clustering of precipitates generating surface cracks and crack growth through the thickness, resulting in ultimate failure of the SMA actuators. Such damage mechanism is found to dominate the fatigue failure of the $Ni_{60}Ti_{40}$ SMA actuators, thus dictating their fatigue life.

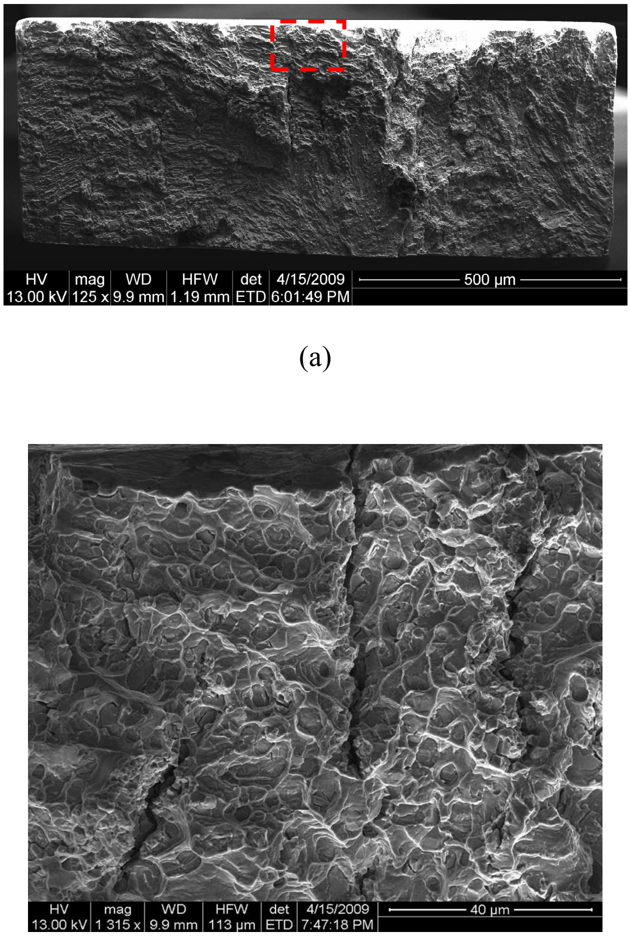

(a)

(b)

Figure 106. Fracture surface and detail on clustering of precipitates from surface through thickness, cracks showing path through clustered precipitates.

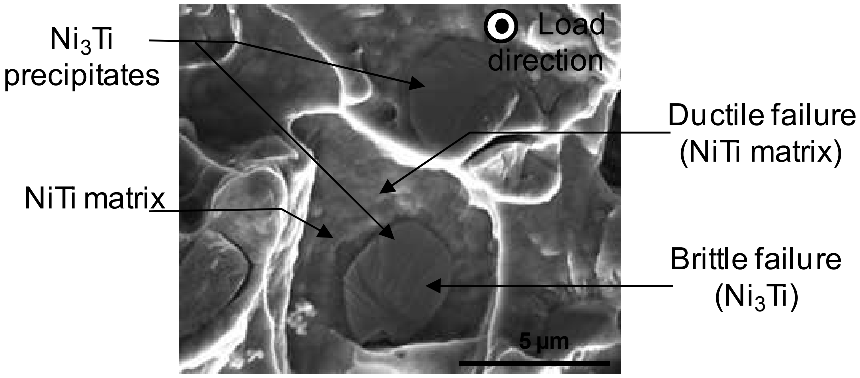

Figure 107. SEM micrograph showing brittle fracture of Ni_3Ti precipitates with damage in the surrounding NiTi matrix.

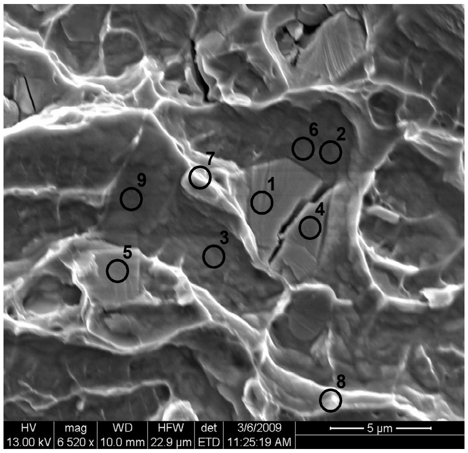

(a)

Position	**Ni wt.% (at.%)**	**Ti wt.% (at.%)**
1	**84.88 (82.08)**	**15.12 (17.92)**
2	**37.23 (32.61)**	**62.77 (67.39)**
3	**65.12 (60.37)**	**34.88 (39.63)**
4	**85.05 (82.28)**	**14.95 (17.72)**
5	**85.44 (82.72)**	**14.56 (17.28)**
6	**63.41 (58.57)**	**36.59 (41.43)**
7	**62.02 (57.12)**	**37.98 (42.88)**
8	**73.16 (68.98)**	**26.84 (31.02)**
9	**56.96 (51.92)**	**43.04 (48.08)**

(b)

Figure 108. Site of observation and measurement post fatigue testing: SEM EDS analysis of the fracture surface of $Ni_{60}Ti_{40}$ SMA actuators; (a) area of interest showing the different phases: a cracked ductile NiTi matrix and brittle failure of Ni_3Ti bulky and (b) chemical analysis of the observed phases.

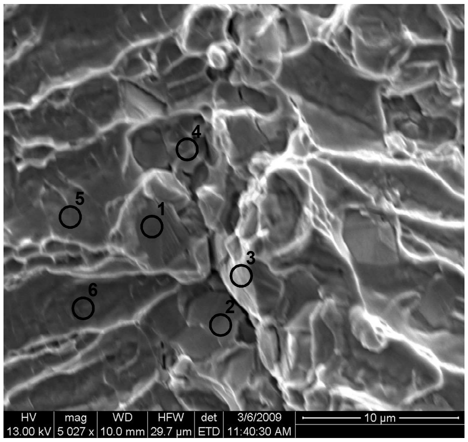

(a)

Position	Ni wt.% (at.%)	Ti wt.% (at.%)
1	80.25 (76.83)	19.75 (23.17)
2	17.26 (14.54)	82.74 (85.46)
3	50.24 (45.17)	49.76 (54.83)
4	9.22 (7.65)	90.78 (92.35)
5	65.00 (60.24)	35.00 (39.76)
6	60.88 (55.94)	39.12 (44.06)

(b)

Figure 109. Site of observation and measurement post fatigue testing: SEM EDS analysis of the fracture surface of $Ni_{60}Ti_{40}$ SMA actuators; (a) area of interest showing the effect of clustering on crack propagation and (b) chemical analysis of the observed phases.

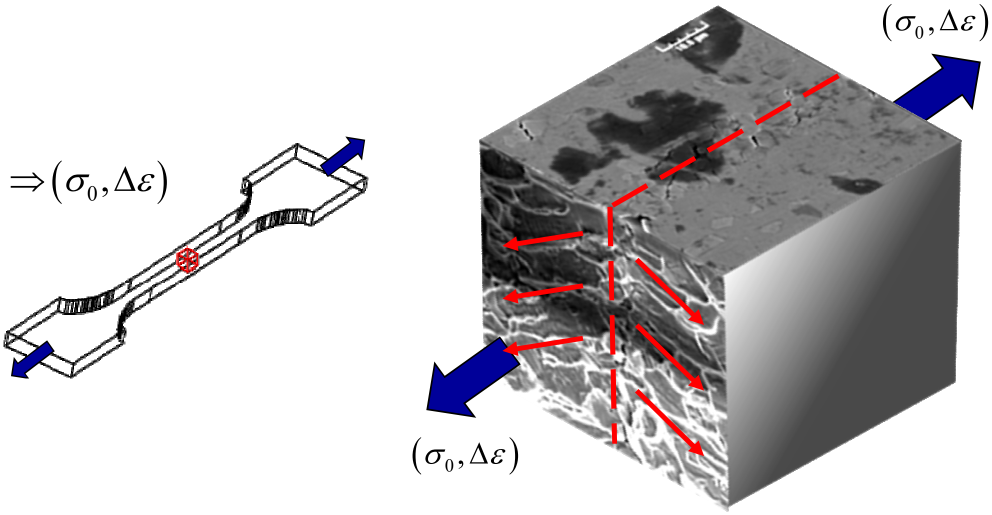

Figure 110. Clustered precipitates and localization of failure in $Ni_{60}Ti_{40}$ SMA actuators.

5.4.2. Influence of Ni_4Ti_3 / Ni_3Ti_2 precipitates on fatigue failure mechanisms

The Ni_4Ti_3 / Ni_3Ti_2 precipitates have a very different morphology and can be found as big as a few micrometers (Figure 83 and Figure 84). They have a needle-like shape or a slant penny-like shape. They form a complex network when they grow to the micrometer size and therefore constitute a “backbone” structure for the NiTi matrix to transforms in between. This complex network, formed during the various heat treatments (shape set followed by aging), would act similarly to Ni_3Ti if Ni_4Ti_3 / Ni_3Ti_2 precipitates were having the same impact on the failure mechanism. However, from fractography and analysis, the Ni_4Ti_3 / Ni_3Ti_2 precipitates, besides assisting to the transformation mechanism, they do not appear to be a direct cause for the $Ni_{60}Ti_{40}$ SMA actuators to fail prematurely.

5.4.2.1. Surface damage characterization

The presence of the needle-like Ni_4Ti_3 / Ni_3Ti_2 precipitates is the result of a high Nickel content from a Nickel rich NiTi matrix that diffuses into metastable secondary phases. While the presence of stable Ni_3Ti precipitates do not serve a purpose to the martensitic phase transformation mechanism, but to a strengthening and hardening of the material, the Ni_4Ti_3 / Ni_3Ti_2 are grown and adjusted during a lower temperature aging treatment (450°C in this work) and stabilized in the material at room temperature by mean of water quenching. They work along with the phase transformation to act as barriers limiting the evolution and propagation of dislocations. Therefore, repeated actuation under load results in the accumulation of defects at the interface Ni_4Ti_3/Ni_3Ti_2 with the NiTi matrix. From comparison between non-precipitated and precipitated SMAs, the amount of accumulation plastic varies from a higher to a lower level, respectively. Therefore, less damage is expected from this mechanism but can be observed from microstructural analysis such as shown in Figure 111. the damage and cracks generated in the Ni_3Ti precipitates that were discussed in the previous subsection, it appears clearly that the pristine surface quality that was obtained after fine polish is now altered in areas where Ni_4Ti_3/Ni_3Ti_2 interact with the NiTi matrix , as seen in Figure 111(a). This mechanism is confirmed on the entire surface of the SMA actuators and not only near the fracture surface where localization may have been responsible, as shown in Figure 111(b). One can identify the unique distribution of the metastable Ni-rich precipitates in triangular patterns with strong orientation along the rolling direction, represented vertically in the corresponding micrographs. The mechanism of damage accumulation at the interface NiTi matrix and Ni_4Ti_3/Ni_3Ti_2 is globally observed. However, at locations where Ni_3Ti precipitates initiate failures, it appears that the Ni_4Ti_3/Ni_3Ti_2 precipitates undergo higher levels of deformation and stresses resulting in very fine cracks along the metastable precipitate network, as detailed in Figure 111(c). This observation indicates a saturation of the local martensite with defects that results in development of cracks aligned with certain Ni_4Ti_3/Ni_3Ti_2 precipitates.

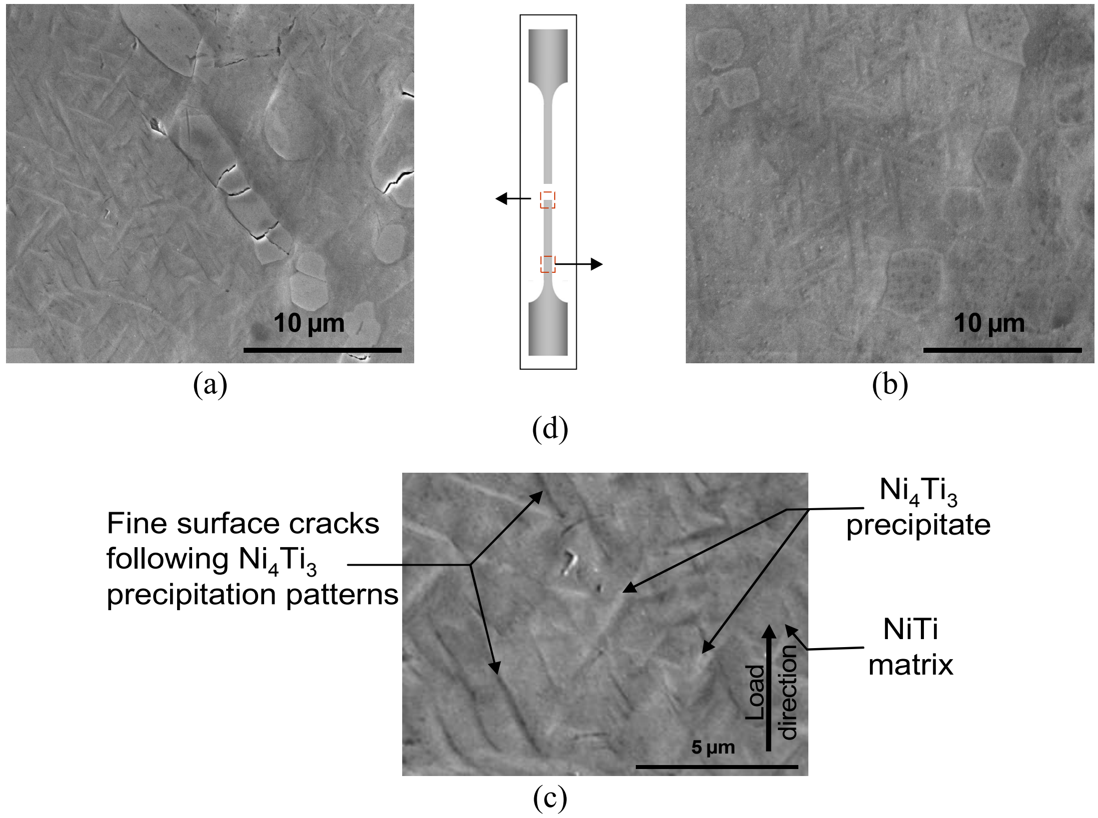

(a) (b)

(d)

(c)

Figure 111. Site of observation and measurement post fatigue failure tested in Nitrogen: SEM EDS analysis of the surface of $Ni_{60}Ti_{40}$ SMA actuators after long aging treatment; (a) low crack density within Ni_4Ti_3/Ni_3Ti_2 network near fracture surface, (b) low crack density within Ni_4Ti_3/Ni_3Ti_2 network away from fracture, (c) interaction sites between NiTi matrix and Ni_4Ti_3/Ni_3Ti_2 with crack formation.

5.4.2.2. Bulk damage characterization

The mechanism of damage in the bulk of the material related to the existence of the metastable precipitates is accentuated when looking at fracture surfaces. It was found that most of the fracture surface was made of damage and cracks due to the brittle nature of the $\mathrm{Ni_3Ti}$ precipitates working against the relatively more ductile NiTi matrix. However, in some areas, damage caused by the interaction between $\mathrm{Ni_4Ti_3/Ni_3Ti_2}$ and NiTi matrix can be found and related to the previous surface observations. Figure 112 shows the overall fracture surface with a magnification of an area where secondary damage was observed. It is clearly seen how the $\mathrm{Ni_4Ti_3/Ni_3Ti_2}$ precipitates developed cracks and created a pattern that is identical to the one previously observed in the secondary surface damage shown in Figure 111(c). Figure 113 represents the detail of the damage caused by the interactions between NiTi matrix and $\mathrm{Ni_4Ti_3/Ni_3Ti_2}$. From these observations, it is understood that the damage resulting from this mechanism is secondary and provides path for crack propagation rather that for crack initiation, therefore it is concluded that while the fatigue life and failure is dictated by the $\mathrm{Ni_3Ti}$ precipitates, $\mathrm{Ni_4Ti_3/Ni_3Ti_2}$ precipitates contribute to a propagation mechanism.

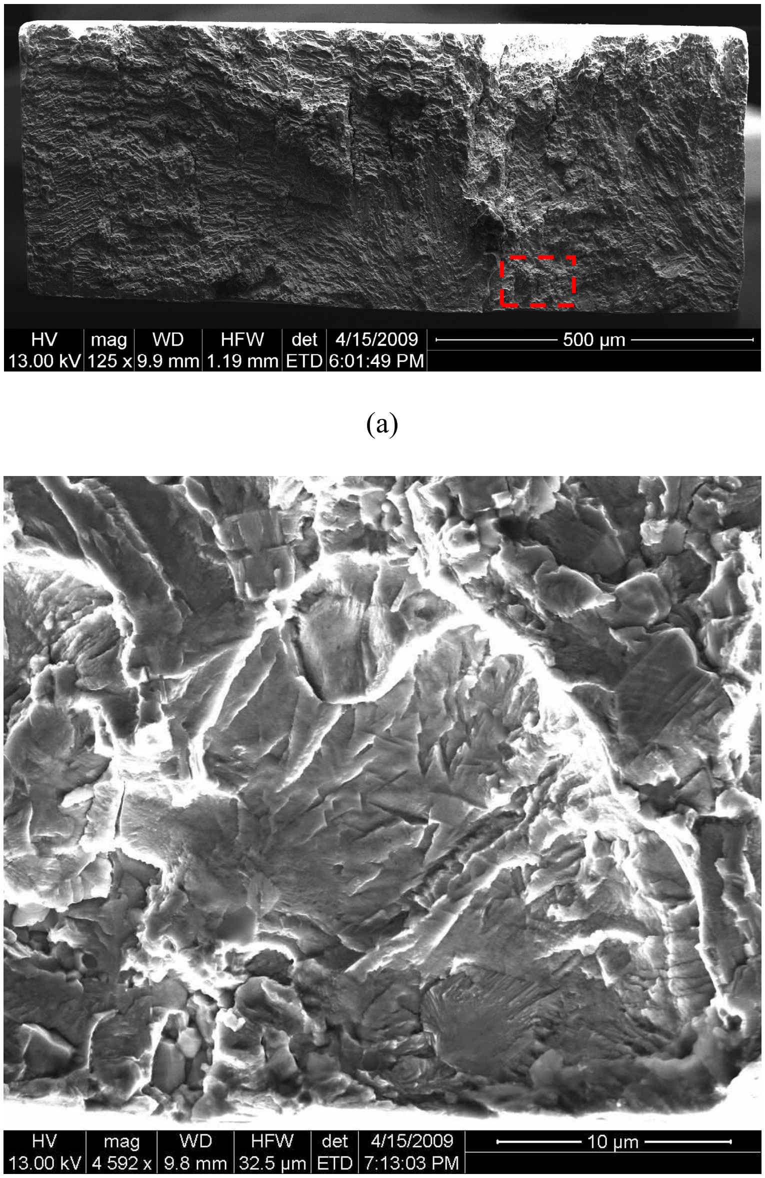

(a)

(b)

Figure 112. (a) Fracture surface and (b) detail on clustering of precipitates from surface through thickness, cracks showing path through clustered precipitates.

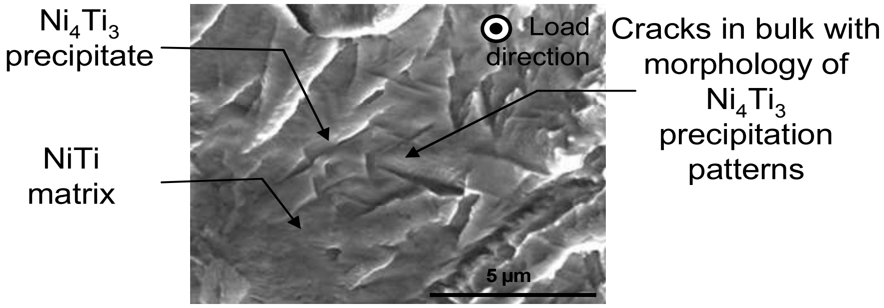

Figure 113. SEM micrograph showing fracture/tear patterns of Ni_4Ti_3 / Ni_3Ti_2 precipitates in the NiTi matrix.

CHAPTER VI

CONCLUSIONS AND FUTURE WORK

In a scientific community where new theories, new techniques and new application-oriented projects are driving the need for constant improvement and research, the characterization and modeling of the transformation induced fatigue behavior of SMA actuators is critical. The understanding of failure mechanisms involved in the failure of future application-based components will allow the correction of weaknesses causing early fatigue failure, therefore leading to a design optimization.

6.1. Summary and conclusions

In Chapter II, the focus was the study of the constant stress, thermomechanical, transformation induced fatigue of TiNiCu SMA wire actuators and the assessment of the influence of corrosion on the fatigue life. Two series of tests were conducted, one for complete transformation cycles and another for partial transformation cycles.

The fatigue life of TiNiCu SMA wire actuators was improved by an order of magnitude when actuation strain was reduced by approximately 50%. The accumulated plastic strain was found to be a function of the number of cycles to failure using a Manson-Coffin power-law and dictates the fatigue life of the SMA actuators. The transformation induced fatigue of SMA wire actuators in a corrosive cooling environment resulted in a significant reduction of the number of cycles to failure and corrosion was found to act more severely in the case of partial transformation cycles. The study of the fatigue life of $Ti_{50}Ni_{40}Cu_{10}$ was found to be consistent with fatigue life results obtained by others [16, 43]. Investigations on composition variations, such as $Ti_{50}Ni_{45}Cu_5$, showed slightly higher fatigue limits [24] and the highest were found for equiatomic NiTi [3]. The reduction of the fatigue life with increasing Cu content from 0 to up to 10 at.% was consistent with what was found in the literature.

One of the interests of this study was to perform high actuation frequency fatigue testing using convective cooling. The consequence was an actuation frequency increased by nearly an order of magnitude, i.e. 0.01 Hz under natural cooling conditions versus 0.1 Hz under convective cooling conditions, which in return led to the creation of a corrosive environment. The consequence was a reduced fatigue life in comparison to fatigue results generated in a corrosion free environment, and this reduction was due to the coupling between corrosion and repeated martensitic phase transformation. The presence of a corrosive cooling environment led to the formation of a detrimental surface layer that contributed to the initiation and growth of circular microcracks.

The focus of Chapter III was a post failure microstructure analysis, the definition of a cyclic damage mechanism and the formulation of a damage accumulation rule for fatigue life modeling accounting for corrosion. From microstructural analysis, a proposed cyclic damage mechanism presenting the coupling between corrosion and cyclic phase transformation contributing to the formation of a brittle surface layer was introduced. This mechanism was validated by the application of a shear-lag model accounting for inelastic strains due to both reversible martensitic phase transformation and irrecoverable accumulated plastic strain. The micromechanical analysis demonstrated the influence of the amount of transformation strain on different critical crack spacing to failure.

Finally, a fatigue life analysis was carried out to assess the influence of cyclic corrosion on the reduction of the fatigue life of SMA wire actuators. The Miner's rule was applied using stress renormalization functions modeling a continuous cyclic crack growth. While more complex and more accurate models were available, such as non-linear damage accumulation models or fracture mechanics based models, Miner's rule presented the advantage to be simple and in our specific case, quite accurate too. Two approaches were developed based on the Miner's rule. The first method, called direct Miner's rule, permitted a validation of the proposed assumptions and formulation. The inverse Miner's, however, made the model fully predictive and enabled its user to predict the fatigue life of SMA actuators in corrosion-free conditions from only corrosive fatigue data. The results also indicated that the model was conservative, constituting a safety margin for future design applications.

Chapters IV and V corresponded to and are still referring to an ongoing research effort pursued between the Boeing Company and Texas A&M University. The need for certification by the Federal Aviation Administration before an application such as the Variable Geometry Chevrons actuated by Nickel rich NiTi SMA beam actuators is implemented in the future Boeing 787 commercial airplane is unavoidable. A systematic approach with parametric study, both on the macroscopic and microscopic level led to the identification of critical parameters. The identification of parameters such as such processing, specimen thickness, applied stress level, surface finish and testing environment contributed to the isolation of external mechanisms to focus on the critical role of the microstructure on the fatigue life of Nickel rich SMA actuators. The never tested before new alloy composition presenting a higher Nickel content than in the well studied and applied equiatomic NiTi SMA, presented and still embodies challenges. It was shown how precipitation can affect not only the actuation characteristics but also the performances under cyclic loading. It was also concluded that while the fatigue mechanism, fatigue life and fatigue failure in non-precipitated SMAs were dictated by the evolution of dislocations and accumulation of plastic strains through large strain incompatibilities, highly precipitated SMAs exhibit a behavior dependent on two different mechanisms: the material response and stabilization due to global effects such as the accumulation of plastic strains and the application of external stress, but also a fatigue life and failure mechanism dictated by a complex and very sensitive microstructure.

A general conclusion that can be drawn out of this work is the fact that whether the SMA is non-precipitated, exhibiting high actuation performances (3-4% actuation strain between 50 -250 MPa), accumulating significant amount of irrecoverable strains and therefore dimensionally unstable (i.e. TiNiCu and equiatomic NiTi, with 3-6% plastic strain) or highly precipitated SMA, exhibiting lower actuation performances (1-1,2% actuation strain between 100 – 250 MPa) with better dimensional stability (i.e. Ni-rich NiTi, with 1-2% plastic strain), the fatigue life is relatively similar within the low-cycle range of nearly 1,000 cycles to a transition to 100,000 cycles.

6.2. Future work

Continuation of this work has become highly relevant with the new interest in more stable and more reliable actuators such as the new class of Ni-rich NiTi SMAs. The development of methods that can be utilized to certify and validate fatigue life for particular applications such as the Boeing VGCs are absolutely necessary before one can see such advancement take place in everyday commercial airplanes. Validation of the preliminary results obtained from small size specimens will require a comparison to real size actuators to assess the reliability of small scale testing.

However, on a more scientific level, the material system utilized for such applications is still unknown and its potential improvement through process and microstructure optimization is highly promising. On a systematic level, one can see how the combination of testing, performance and microstructure evaluation, and damage assessment can establish an iterative optimizing cycle that may eventually lead to the formulation of a predictive model. The latest analysis and understanding from the failure mechanisms could lead to possible cohesive law type models that could account for precipitation density, distribution, size, and probability of failure.

REFERENCES

[1] Lagoudas D C, editor. Shape memory alloys: modeling and engineering applications. New York: Springer-Verlag, 2008.

[2] Tobushi H, Hachisuka T, Hashimoto T, Yamada S. Cyclic deformation and fatigue of a TiNi shape-memory alloy wire subjected to rotating bending. Journal of Engineering Materials and Technology 1998; 120(1): 64-70.

[3] Miyazaki S, Mizukoshi K, Ueki T, Sakuma T, Liu Y. Fatigue life of Ti–50 at.% Ni and Ti–40Ni–10Cu (at.%) shape memory alloy wires. Mat Sci Eng 1999; A273-275: 658-63.

[4] Furuichi Y, Tobushi H, Ikawa T, Matsui R. Fatigue properties of a TiNi shape-memory alloy wire subjected to bending with various strain ratios. Proc. Instn Mech. Engrs, Part L: J. Materials: Design and Applications 2003; 217(L2): 93-9.

[5] Gall K, Maier H J. Cyclic deformation mechanisms in precipitated NiTi shape memory alloys. Acta Mater 2002; 50: 4643–57.

[6] Young J M, Van Vliet K J. Predicting In vivo failure of pseudoelastic NiTi devices under low cycle, high amplitude fatigue. J Biomed. Mater Res, Part B: Appl Biomater 2005; 72(B): 17-26.

[7] De Azevedo Bahia M G, Fonseca Dias R, Buono Vincente T L. The influence of high amplitude cyclic straining on the behaviour of superelastic NiTi. Int J Fatigue, 2006; 28(9): 1087-1091

[8] Birman V. Review of mechanics of shape memory alloy structures. Applied Mechanics Reviews 1997; 50(11): 629-45.

[9] Otsuka K, Wayman C M. Shape Memory Materials. Cambridge, UK: Cambridge University Press, 1998.

[10] Miller D A, Lagoudas D C. Thermomechanical characterization of NiTiCu and NiTi SMA actuators: influence of plastic strains. Smart Mater Struct 2000; 9(5): 640-52.

[11] Hebda D, White S R. Effect of training conditions and extended thermal cycling on Nitinol two-way shape memory behavior. Smart Mater Struct 1995; 4: 298-304.

[12] Lim T J, McDowell D L. Degradation of a Ni-Ti alloy during cyclic loading. In: Varadan V K, editor. Proceedings of SPIE, Orlando, FL, May 1994, Smart structures and materials: Smart materials, vol 2189; 1994, [326-41].

[13] Bo Z, Lagoudas D C. Thermomechanical modeling of polycrystalline smas under cyclic loading, part III: evolution of plastic strains and two-way memory effect. Int J Eng Sci 1999; 37: 1175-1203.

[14] Calkins F T, Butler G W. Subsonic jet noise reduction variable geometry chevron. 42nd AIAA Aerospace Sciences Meeting and Exhibit, 2004, AIAA-2004-0190, Reno NV.

[15] Calkins F T, Mabe J, Butler G. Boeing's variable geometry chevron: Morphing aerospace structures for jet noise reduction. In: White E V, editor. Proceedings of SPIE, San Diego, CA, March 2006, smart structures and materials: industrial and commercial applications of smart structures technologies, vol 6171; 2006, [6171-22].

[16] Bigeon M, Morin M. Thermomechanical study of the stress assisted two way memory effect fatigue in TiNi and CuZnAl wires. Scripta Materialia 1996; 35(12): 1373-78.

[17] De Araujo C J, Morin M, Guénin G. Electro-thermomechanical behaviour of a Ti-45.0Ni-5.0Cu (at.%) alloy during shape memory cycling. Mat Sci Eng 1999; A273-275: 305-9.

[18] Lagoudas D C, Li C, Miller D A, Rong L. Thermomechanical transformation fatigue of SMA actuators. In: Lynch C S, editor. Proceedings of SPIE, San Diego, CA, June 2000, smart structures and materials: active materials: behavior and mechanics, vol 3992; 2000, [420-9].

[19] López Cuéllar E, Guénin G, Morin M. Study of the stress-assisted two-way memory effect of a Ti–Ni–Cu alloy using resistivity and thermoelectric power techniques. Mater Sci Eng 2003; A358(1-2): 350-5.

[20] Figueiredo A M, Modenesi P, Buono V. Low-cycle fatigue life of superelastic NiTi wires. Int J Fatigue 2009; 31(4): 751-8.

[21] Tamura H, Mitose K, Suzuki Y. Fatigue properties of Ti-Ni shape memory alloy springs. Jnl Physics 1995; IV5(C8): 617.

[22] Lagoudas D C, Miller D A, Rong L, Kumar P K. Thermomechanical transformation fatigue of shape memory alloys, Smart Mater Struct 2009; 18: 085021 (12 pp).

[23] Bertacchini O W, Lagoudas D C and Patoor E. Thermomechanical transformation fatigue of TiNiCu SMA actuators under a corrosive environment – Part I: experimental results. Int J Fatigue 2009; 31: 1571–8.

[24] Bhaumik S K, Saikrishna C N, Ramaiah K V, Venkataswamy M A. Understanding the fatigue behaviour of NiTiCu shape memory alloy wire thermal actuators. Key Eng Mater 2008; 378-379: 301-16.

[25] Proft J L, Melton K N, Duerig T W. Transformational cycling of NiTi and NiTiCu shape memory alloys. MRS conference 1989; 9: 159-64.

[26] Bertacchini O, Lagoudas D, Patoor E. Fatigue life characterization of shape memory alloys undergoing thermomechanical cyclic loading. In: Lagoudas D C, editor. Proceedings of SPIE, San Diego, CA, August 2003, smart structures and materials: active materials: behavior and mechanics, vol 5053; 2003, [612-24].

[27] Morgan N B, Friend C M. A review of shape memory stability in NiTi alloys. Jnl Physics 2001; IV11(PR8): 325-32.

[28] Tae-hyun N, Jae-hwa L, Gyu-bong C, Yeon-wook K. Stability of the B19 martensite in rapidly solidified Ti–Ni–Cu alloys. Mat Sci Eng 2006; A(438–440): 687–90.

[29] Kustov S, Pons J, Cesari E, Van Humbeeck J. Chemical and mechanical stabilization of martensite. Acta Mater 2004; 52: 4547–59.

[30] Liu1 Y, Favier D. Stabilisation of martensite due to shear deformation via variant reorientation in polycrystalline NiTi. Acta Mater 2000; 48(13): 3489-99.

[31] Hornbogen E. Review thermo-mechanical fatigue of shape memory alloys. Jnl Mater Sci 2004; 39: 385-99.

[32] Eggeler G, Hornbogen E, Yawny A, Heckmann A, Wagner M. Structural and functional fatigue of NiTi shape memory alloys Materials. Sci Eng 2004; A378: 24–33.

[33] Hornbogen E, Eggeler G. Surface aspects in fatigue of shape memory alloys (SMA). Materialwissenschaft und Werkstofftechnik 2004; 35(5): 255-9.

[34] Cheung G S P, Darvell B W. Fatigue testing of a NiTi rotary instrument. Part 2: Fractographic analysis. Int Endodontic J 2007; 40(8): 619-25.

[35] Bannantine J A, Comer J J, Handrock J L, editors. Fundamentals of metal fatigue analysis. Upper Saddle River, NJ: Prentice Hall Pub, 1990.

[36] Meetham, G W. High-temperature materials - a general review. J Mater Sci 1991; 26: 853-60.

[37] Tong J, Dalby S, Byrne J, Henderson M B, Hardy M C. Creep, fatigue and oxidation in crack growth in advanced nickel base superalloys. Int J Fatigue 2001; 23(10): 897-902.

[38] Noebe R, Draper S, Gaydosh D, Garg A, Lerch B, Bigelow G, Padula II S. Effect of thermomechanical processing on the microstructure, properties, and work behavior of a Ti50:5Ni49:5Pt20 high-temperature shape memory alloy. In Proceedings of the International Conference on Shape Memory and Superelastic Technologies, ASM International, Metals Park, OH; 2006, [1-10].

[39] Lagoudas D C, Chatzigeorgiou G, Kumar P K. Modeling and experimental study of simultaneous creep and transformation in polycrystalline high temperature shape memory alloys. Journal of Intelligent Material Systems and Structures, accepted for publication, 2009.

[40] Miller D A. Thermomechanical characterization of plastic deformation and transformation fatigue in shape memory alloys. PhD thesis, Texas A&M University College Station TX, USA, 2000.

[41] Shabalovskaya S A. Surface, corrosion and biocompatibility aspects of Nitinol as an implant material. Bio-Medical Mater and Eng 2002; 12: 69–109.

[42] Firstov G S, Vitchev R G, Kumar H, Blanpain B, Van Humbeeck J. Surface oxidation of NiTi shape memory alloy. Biomater 2002; 23: 4863-71.

[43] De Araújo C J, Morin M, Guénin G. Fatigue behavior of Ti-Ni-Cu thin wires SME. J Physique 1997; IV-7(11): 501-6.

[44] Clingman D, Calkins F, Smith J. Thermomechanical properties of 60-nitinol. In: Lagoudas D C, editor. Proceedings of the SPIE, San Diego, CA, August 2003, smart structures and materials: active materials: behavior and mechanics, vol 5053, 2003, [219–29].

[45] Nishida M, Wayman C M, Honma T. Precipitation process in near-equiatomic TiNi shape memory alloys. Metall trans. 1986; A(17): 1505-15.

[46] Kainuma R, Matsumoto M, Honma T. Metallographic study of precipitation processes in Ni-rich TiNi alloys. Tohoku Daigaku Senko Serein Kenkyujo Iho 1987; 43(2): 149-58.

[47] Adharapurapu R R, Vecchio K S. Superelasticity in a new bioimplant material: Ni-rich 55NiTi alloy. Exp Mech 2007; 47(3): 365-71.

[48] Mabe J, Ruggeri R, Calkins F. Characterization of nickel-rich nitinol alloys for actuator development. In Proceedings of the International Conference on Shape Memory and Superelastic Technologies, ASM International, Metals Park, OH; 2006, [1-10].

[49] Mabe J H, Cabell R H, Butler G. Design and control of a morphing chevron for takeoff and cruise noise reduction. In 11th AIAA/CEAS Aeroacoustics Conference (26th AIAA Aeroacoustics Conference), 23 - 25 May, Monterey, CA; 2005, [1-15].

[50] Khalil Allafi J, Ren X, Eggeler G. The mechanism of multistage martensitic transformations in aged Ni-rich NiTi shape memory alloys. Acta Mater 2002; 50: 793-803.

[51] Wojcik C C. Aging effects in nickel rich Ni-Ti alloys. In Proceedings of the International Conference on Shape Memory and Superelastic Technologies, Baden-Baden, GE; 2004, [229–36].

[52] Hartl D, Volk B, Lagoudas D C, Calkins F T, Mabe J. Thermomechanical characterization and modeling of $Ni_{60}Ti_{40}$ SMA for actuated chevrons. In Proceedings of ASME, International Mechanical Engineering Congress and Exposition (IMECE), 5–10 November, Chicago, IL; 2006, [1–10].

[53] Funakubo H, editor. Shape Memory Alloys. London, UK: Gordon and Breach Publishers, 1987.

[54] Bertacchini O W, Lagoudas D C, Patoor E. Surface crack development in transformation induced fatigue of SMA actuators. In: Gdoutos E E, editor. Proceedings of the 16th European Conference of Fracture, Alexandropoulos, Greece, 3-7 July, 2006, fracture of nano and engineering structures, vol C; 2006, [1309-10].

[55] McCartney L N. New theoretical model of stress transfer between fibre and matrix in a uniaxially fibre-reinforced composite. Proc R Soc, London, UK, 1989; A425: 215-44.

[56] McCartney L N. Analytical models of stress transfer in unidirectional composites and cross-ply laminates, and their application to the prediction of matrix/transverse cracking. In Proceedings of IUTAM Symposium, Local mechanics concepts for composite material systems, Blacksburg, VA; 1991, [251-8].

[57] Nairn J A. On the use of shear-lag methods for analysis of stress transfer in unidirectional composites. Mech Mater 1997; 26: 63-80.

[58] Miller D A, Lagoudas D C. Thermomechanical characterization of NiTiCu and NiTi SMA actuators: influence of plastic strains. Smart Mater Struct 2000; 9: 640–52.

[59] Armitage D A, Grant D M. Characterization of surface-modified nickel titanium alloys. Mat Sci Eng 2003; A(349): 89-97.

[60] Glassford K M, Chelikowsky J R. Structural and electronic properties of titanium dioxide. Phys. Rev. B 1992; 46(3): 1284-98.

[61] Mayo M J, Siegel R W, Narayanasamy A. Mechanical properties of nanophase TiO2 as determined by nanoindentation. J Mater Res 1990; 5: 1073.

[62] Han Y, Hong S H, Xu K W. Porous nanocrystalline titania films by plasma electrolytic oxidation. Surface and Coatings Technology 2002; 154: 314–8.

[63] Manghnani M H, Fisher E S, Browser W S Jr. Temperature dependence of the elastic constants of single-crystal rutile between 4 and 583 K. J Phys Chem Solids 1972; 33: 2149.

[64] Barisona S, Cattarina S, Daolioa S, Musiania M, Tuissi A. Characterization of surface oxidation of nickel–titanium alloy by ion-beam and electrochemical techniques. Electrochimica Acta 2004; 50: 11-8.

[65] Lagoudas D C, Entchev P, Triharjanto R. Modeling of oxidation and its effect on crack growth in titanium alloys. Comput Methods Appl Mech Eng 2000; 183(1-2): 35-50.

[66] Gdoutos E E, editor. In Solid mechanics and its applications; vol. 14, Fracture mechanics: an introduction. Dordrecht: Kluwer Academic Publishers, 1993.

[67] Palmgren A. Die Lebensdauer von Kugellagern Verfahrenstechinik 1924;68:339-341.

[68] Miner M A. Cumulative damage in fatigue. J Appl Mech 1945; 12(A): 159-64.

[69] Fatemi A, Yang L. Cumulative fatigue damage and life prediction theories: a survey of the state of the art for homogeneous materials. Int J Fatigue 1998; 20(I): 9-34.

[70] Schick J R. Transformation induced fatigue of Ni-rich NiTi SMA actuators. M.S. thesis, Texas A&M University College Station TX, USA, 2009.

[71] Theisen W, Schuermann A. Electro discharge machining of nickel–titanium shape memory alloys. Materials Science and Engineering 2004: A(378): 200–4.

[72] Chiang L J, Li C H, Hsu Y F, Wang W H. Ages-induced four-stage transformation in Ni-rich NiTi shape memory alloys. J Alloys and Compounds 2008; 458: 231-7.

VITA

Olivier Walter Bertacchini, son of Serge Walter Raymond Bertacchini and Jacqueline Henriette Yvonne Gallice, was born in March of 1977 in Saint-Raphaël, France. He graduated from high school in June of 1995 and was immediately accepted at the “Lycée Technique Régional des Eucalyptus”, in Nice, France. During the next three years, he prepared for the national competitive examination for the “Grandes Ecoles”, which he successfully passed in August of 1998. He then gained access to the Ecole Nationale Supérieure d’Arts et Métiers in Metz (Arts et Métiers Paris-Tech), France, where he obtained his Engineering Diploma and M.S. degree in July of 2002. He spent a year working as a research assistant at Texas A&M University before he was accepted to pursue his Ph.D. degree in Aerospace Engineering in September of 2003. He completed his degree in December of 2009.

Olivier can be reached at the following address:

c/o Dr. Dimitris C. Lagoudas
Department of Aerospace Engineering
Texas A&M University
College Station, TX 77843-3141